Investigating the biophysical, biochemical, and biological activity of anti-cancer zinc oxide nanoparticle and its physiometacomposite (PMC) nanoparticles

by

Elza Neelima Mathew

B.V.Sc. & AH., Kerala Agricultural University, 2010

M.V.Sc., Guru Angad Dev Veterinary & Animal Sciences University, 2013

M.S., University of Connecticut, 2017

AN ABSTRACT OF A DISSERTATION

submitted in partial fulfillment of the requirements for the degree

DOCTOR OF PHILOSOPHY

Department of Anatomy & Physiology

College of Veterinary Medicine

KANSAS STATE UNIVERSITY

Manhattan, Kansas

2020

Abstract

Combating melanoma, the most lethal form of skin cancer, our research group works towards assessing the anticancer potential of zinc oxide (ZnO) nanoparticle and its different physiological metal oxide nanoparticles or physiometacomposite (PMC) nanoparticles. Among these, the antimelanoma cytotoxic activity of zinc oxide nanoparticle (ZnO NP; 100 nm) has been extensively demonstrated. The objective of the proposed study is to elucidate the biophysical, biochemical, and biological mechanisms of the anti-cancer activity of ZnO NP and its PMCs. For biophysical and biochemical characterization, dynamic light scattering (DLS), two-dimensional fluorescence difference spectroscopy (2-D FDS), transmission electron microscopy (TEM) and inductively coupled plasma mass spectrometry (ICP-MS) have been used. The biological activity of the different nanoparticles was investigated in NIH3T3 mouse fibroblast cells and B16F10 mouse melanoma cells followed by *in vivo* investigation in a mouse model. The behavior of the nanoparticles in different mouse tissues was also monitored *ex vivo*. This dissertation presents the significant findings of this study. Chapter 1 gives a general introduction to the dissertation and an overview of ZnO NP, its anti-cancer activity, *in vivo* behavior, and a brief outline on melanoma particularly drug resistant and rarer forms. Chapter 2 is a detailed review of the anticancer activity of zinc oxide nanoparticles and combining ZnO NPs with nucleic acid therapeutic and protein delivery against metastatic melanoma. Chapter 3 investigates the immunological activity of zinc oxide nanoparticle and its anticancer peptide and RNA complexes. Chapter 4 characterizes the biochemical activities of ZnO NP and its PMCs in terms of inhibition of enzyme activities and associations of enzymes involved in the RAS pathway of metastatic progression. In Chapter 5, the interaction of ZnO NP with proteins using Ras binding Domain (RBD) as the model protein is investigated. In chapter 6, the combinatory anti-melanoma potential of ZnO NP and LL-37, an

antimicrobial peptide, which is currently in clinical trials against melanoma is investigated. Chapter 7 summarizes the main findings from the previous chapters. An in-depth investigation of the cellular mechanisms and *in vivo* physiological/pathological effects is expected to help in molding new therapeutic targets and approaches. Demonstration of precise mechanisms of action is expected to help with the development of further therapeutic approaches utilizing ZnO NP.

Investigating the biophysical, biochemical, and biological activity of anti-cancer zinc oxide nanoparticle and its physiometacomposite (PMC) nanoparticles

by

Elza Neelima Mathew

B.V.Sc. & AH., Kerala Agricultural University, 2010

M.V.Sc., Guru Angad Dev Veterinary & Animal Sciences University, 2013

M.S., University of Connecticut, 2017

A DISSERTATION

submitted in partial fulfillment of the requirements for the degree

DOCTOR OF PHILOSOPHY

Department of Anatomy & Physiology

College of Veterinary Medicine

KANSAS STATE UNIVERSITY

Manhattan, Kansas

2020

Approved by:

Major Professor

Dr. Robert K. DeLong

Copyright

Abstract

Combating melanoma, the most lethal form of skin cancer, our research group works towards assessing the anticancer potential of zinc oxide (ZnO) nanoparticle and its different physiological metal oxide nanoparticles or physiometacomposite (PMC) nanoparticles. Among these, the antimelanoma cytotoxic activity of zinc oxide nanoparticle (ZnO NP; 100 nm) has been extensively demonstrated. The objective of the proposed study is to elucidate the biophysical, biochemical, and biological mechanisms of the anti-cancer activity of ZnO NP and its PMCs. For biophysical and biochemical characterization, dynamic light scattering (DLS), two-dimensional fluorescence difference spectroscopy (2-D FDS), transmission electron microscopy (TEM) and inductively coupled plasma mass spectrometry (ICP-MS) have been used. The biological activity of the different nanoparticles was investigated in NIH3T3 mouse fibroblast cells and B16F10 mouse melanoma cells followed by *in vivo* investigation in a mouse model. The behavior of the nanoparticles in different mouse tissues was also monitored *ex vivo*. This dissertation presents the significant findings of this study. Chapter 1 gives a general introduction to the dissertation and an overview of ZnO NP, its anti-cancer activity, *in vivo* behavior, and a brief outline on melanoma particularly drug resistant and rarer forms. Chapter 2 is a detailed review of the anticancer activity of zinc oxide nanoparticles and combining ZnO NPs with nucleic acid therapeutic and protein delivery against metastatic melanoma. Chapter 3 investigates the immunological activity of zinc oxide nanoparticle and its anticancer peptide and RNA complexes. Chapter 4 characterizes the biochemical activities of ZnO NP and its PMCs in terms of inhibition of enzyme activities and associations of enzymes involved in the RAS pathway of metastatic progression. In Chapter 5, the interaction of ZnO NP with proteins using Ras binding Domain (RBD) as the model protein is investigated. In chapter 6, the combinatory anti-melanoma potential of ZnO NP and LL-37, an

antimicrobial peptide, which is currently in clinical trials against melanoma is investigated. Chapter 7 summarizes the main findings from the previous chapters. An in-depth investigation of the cellular mechanisms and *in vivo* physiological/pathological effects is expected to help in molding new therapeutic targets and approaches. Demonstration of precise mechanisms of action is expected to help with the development of further therapeutic approaches utilizing ZnO NP.

Table of Contents

List of Figures xiii
List of Tables xvii
Acknowledgements xviii
Dedication xx
Chapter 1 - Introduction 1
Nanomedicine for cancer therapy 1
Zinc Oxide Nanoparticles (ZnO NPs) 1
Anticancer Activity of Zinc Oxide Nanoparticles 2
Zinc-based Physiometacomposites 3
Investigating the interaction of zinc oxide nanoparticles with proteins 3
In vivo Distribution and Tolerance of Zinc Oxide Nanoparticle 6
Melanoma – Overview 7
Oncogenic pathways for melanomagenesis 8
Treatment for Melanoma 9
Use of B16F10 mouse melanoma model for melanoma 9
Objective of the Dissertation 10
Chapter 2 - Translating Nanomedicine to Comparative Oncology—the Case for Combining Zinc Oxide Nanomaterials with Nucleic Acid Therapeutic and Protein Delivery for Treating Metastatic Cancer 13
Abstract 13
Introduction 14
Cancer and Nanomedicine. 14
Advantages of ZnO NPs. 15
Anticancer Properties of Zinc Oxide 16
ZnO Surface Chemistry 16
Reactive Oxygen Species Generation 17
Intracellular Gradients of Free Zn Ions 17

Biochemical Effects on Enzyme Activity 18
Biologic Activity of ZnO NPs in Animal Models 19
The Case for Zinc Oxide Nanoparticles 21
Effect of ZnO or ZnO-RNA on Experimental Melanoma in Mice 27
Pharmacokinetics of ZnO NPs 29
Pharmacokinetics and Biodistribution of ZnO NPs in Healthy Animals. 29
Pharmacokinetics and Biodistribution of ZnO NPs in Tumor-Bearing Animals 30
Physiologically Based Pharmacokinetic Model for ZnO NPs 32
Comparative Oncology 33
Conclusions and Outlook 35
On the Horizon 37
Targeting Metastases 40
Acknowledgements 40
Authorship Contributions 40
Chapter 3 - Comparative Molecular Immunological Activity of Physiological Metal Oxide Nanoparticle and its Anticancer Peptide and RNA Complexes 42
Abstract 42
Introduction 44
Materials and Methods 45
Materials 45
Cytokine Panel 46
Ex vivo Splenocyte Assay 46
High Throughput Tumor Proteomics Analysis 47
Effect size calculation: 47
Molecular Dynamics 48
IL-6 Assay 49
MTT Assay 49
Results and Discussion 49
In Vitro Immunogenicity 49
Ex vivo Splenocyte Assay 51
In vivo Direct Intratumoral Injection Model 52

Immunological Activity of ZnO NP Antimicrobial Peptide Complexes 54
Combination Therapy Experiment 56
Conclusions 56
Author Contributions 57
Funding 58
Acknowledgments 58
Conflicts of Interest 58
Chapter 4 - Challenging the tumor-microbe biomolecular interface: characterizing antimicrobial physiometacomposite, RNA and protein nanoparticle interactions, enzyme inhibition, signaling and splicing changes in metastatic melanoma cells and tumor 59
Abstract 59
Introduction 60
Materials and methods 60
Materials 60
Methods 61
β-Gal and Luc assays. 61
MTT assay and proteomic microarray analysis: 62
Circos high throughput tumor proteomics analysis: 62
Results and Discussion 63
Physiometacomposites (PMC) 63
Characterization 64
Biochemical inhibition 66
In vivo metastatic tumor analysis 67
Author Contributions 68
Chapter 5 - Interaction of Ras Binding Domain (RBD) with Chemotherapeutic Zinc Oxide Nanoparticles: Progress towards RAS Pathway Protein Interference 70
Abstract 70
Introduction 71
Materials & Methods 72
Materials and Equipment 72
NP stock preparation 73

Zeta potential measurement 73
Fluorescence spectroscopy 73
SDS – PAGE 73
Determination of hydrodynamic size of ZnO NP in cell culture medium over time 74
Determination of dissolution of ZnO NPs in cell culture medium 74
Spheroid Assay 75
MTT assay 75
Apoptosis assay 75
Results and Discussion 76
Confirming interaction of RBD to ZnO NPs 76
Protein gel electrophoresis analysis 78
ZnO NP does not dissociate in cell culture medium 79
Zinc oxide nanoparticles inhibit 3-D spheroids 80
Zinc oxide combined with RBD exhibited anticancer activity in mouse melanoma cells ... 81
Zinc oxide-RBD complexes induce apoptosis morphology in mouse melanoma cells 82
Author Contributions 84
Chapter 6 - Interaction of the antimicrobial peptide LL-37 in with zinc oxide nanoparticle and its physiometacomposites 85
Introduction 85
Materials & Methods 87
Physicochemical Characterization 87
High Resolution-Mass Spectrometry 88
Peptide preparation 88
High-resolution mass spectrometry (HR-MS) 88
Optimizing the loading technique/conditions and payload by BCA Assay 89
Dynamic light scattering 89
SDS-PAGE 89
Biological Characterization *in vitro* 90
MTT assay 90
Investigating the changes in gene expression 90
Reaction Mix Composition: 91

Results and Discussion 91
Physicochemical Characterization 91
Relative abundance of LL-37 peptide: 91
Zeta potential measurements 92
Payload estimation 93
SDS-PAGE analysis 95
Cytotoxicity in mouse melanoma cells 95
Gene expression of ERK and AKT suppressed by ZnO NP and 0.1%Ni/ZnO PMC 97
Conclusion 99
Author Contributions 99
Chapter 7 - Summary 100
Future Perspectives: 100
References 102
Appendix A - Supplemental Information 123
Appendix B - List of Abbreviations 131
Appendix C - List of Publications 135
Appendix D - Copyright Permission 136

List of Figures

Figure 1.1. Periodic element chart showing Zinc and physiological metals with potential anti-cancer activity 3

Figure 1.2. In vivo biodistribution and tolerance of ZnO NP in mice. A. Bioimaging of tissues from BALB/C mice administered with 100 µl phosphate buffered saline (PBS) control or 2 mg/kg single intravenous dose of ZnO-NP or Cy5.5-ZnO NP-PEG. Tissues were collected post-euthanasia within 30 minutes after administration of PBS, 5 days after ZnO NP and 6h after Cy5.5-ZnO NP-PEG. B. Histopathology C. Biodistribution of zinc (estimated by ICP-MS) compared to fluorescence in tissues D. Hematology 6

Figure 2.1. Anticancer activity of ZnO NPs. Anticancer mechanisms include ROS, membrane interference, pH-dependent zinc ion flux or gradients, and enzyme inhibition. 19

Figure 2.2. Altered NF1-RAS-BRAF axis and interactions in RBD lead to downstream ERK and AKT activation in melanoma tumor at-the-time-of-metastasis [adapted from Ramani et al. (2017a,b) and DeLong et al. (2017)]..... 28

Figure 2.3. (Left) RNAfold predicted structure for full-length RBD-specific aptamer with interaction site in the hashed box and bases known to interact with RBD retained as RNA indicated by arrows. (Right) Specificity of its interaction to RBD is shown by the gel shift with micromolar affinity vs. nonspecific RNA control (torula yeast RNA). RBD was tested at 0, 1:10,000, 1:1000, 1:100, or 1:10 dilution of stock at constant RNA concentration (100 µg/ml). 38

Figure 3.1. (A) Comparing in vitro immunological activity for two physiological metal oxide nanoparticles (NP). (B) Dose-response of NP on IL-8 (inset plots HSI results for Co_3O_4 NP) 50

Figure 3.2. Comparing activity of the physiological metal oxide NP by ex vivo splenocyte assay. 52

Figure 3.3. Loss of poly I:C from water supernatant as it associates to ZnO NP after brief spin down in micro-centrifuge. 53

Figure 3.4. Interaction of LL37 to ZnO NP as shown by molecular dynamic simulation (A), electrophoretic gel mobility shift (B) suppresses IL-6 cytokine secretion by BEAS-2B transformed lung cells (C)..... 55

Figure 3.5. Cytotoxic activity of ZnO, ZnO-LL37 or ZnO-LL37/carboplatin combination. 56
Figure 4.1. A) Hierarchy degree of order (binary, ternary, quaternary and hi-order), B) Representative electron microscope image of hi-order PMC, C) Nanoparticle tracking analysis of the hi-order PMC. 64
Figure 4.2. A) Zeta potential surface charge shift of PMC nanomaterials in the presence of protein, signifying protein-NP conjugation. B) Gel shift assay with Poly I:C + ZnO, 5%Co/ZnO, 5%Ni/ZnO and RBD complexes. 65
Figure 4.3. Biochemical inhibition of Luc enzyme with bioluminescent readings at 578 nm (A) and β-Gal enzyme with fluorescence readings ex/em 570/590 (B) and the dose-response of NP or PMC against Luc (C) or β-Gal (D). [Data generated in collaboration with Ryan Swanson and Julie Majka] 66
Figure 4.4. A) Circos plot proteomics analysis of metastatic B16F10-BALB/c tumor [Data generated in collaboration with Dr. Majid Jaberi], B) RAS/ERK/AKT pathway and enzyme associations, C) B16F10 cellular viability in the presence of Co/ZnO + RBD and CoFe/ZnO + RBD with increasing concentration of NP eliciting stable cell death throughout biological dosages (50-200 µg/ml), D) Splicing correction induced by SSO targeting exon 3/intron 4 junction associated with melanoma drug resistance, E) Anticancer activity of the anti-RBD SSO compared to BCL-xL ASO or doxorubicin chemotherapy drug [Data generated in collaboration with Miranda Hurst]..... 67
Figure 5.1. Size measurements of ZnO NP-100 nm and 14 nm 77
Figure 5.2. A. Fluorescence quenching of ZnO NP in the presence and absence of RBD measured at 350 nm further confirming interaction. B. Dissociation constant of RBD complexed to Zinc oxide nanoparticle C. SDS-PAGE analysis of RBD and ZnO nanoparticle combination Lane 1 – Protein Ladder; 2 – RBD alone; 3 – RBD and ZnO NP combination..... 78
Figure 5.3. A. Hydrodynamic size of ZnO NPs (14 nm and 100 nm) monitored over 72h time course. B. Zinc concentration in supernatant monitored over 72h time course..... 80
Figure 5.4. Anticancer activity of ZnO NP in HeLa cell spheroids at 0 h, 24 h and day 5 B. i. Untreated spheroids ii. Spheroids treated with ZnO NP..... 81
Figure 5.5. A. Comparative dose-dependent cytotoxicity in B16F10 cells in response to increasing doses of ZnO NP 100 nm and ZnO NP – 14 nm B. Comparative cytotoxicity in

B16F10 cells in response to RBD-bound ZnO NP 100 nm @ 20 µg/ml C. Bright-field microscopic images (panel A) and fluorescence microscopic images (panel B) of B16F10 cells after 24 h exposure to ZnO + RBD 83
Figure 6.1. Graphical representation of the activity of ZnO in combination with LL-37 87
Figure 6.2. Relative abundance of LL-37 peptide in the fraction received from Indiana University demonstrated by High-Resolution Mass Spectrometry [Data generated in collaboration with Dr. Geraldine Magnin] 92
Figure 6.3. Zeta potential measurements showing the interaction of physiometacomposite nanoparticles with LL-37 peptide 93
Figure 6.4. Absorbance measurements suggesting binding of LL-37 on the surface of ZnO NP and Ni/ZnO PMC NP 94
Figure 6.5. SDS-PAGE suggesting interaction of LL-37 with ZnO NP. Lane 1-Protein ladder; 2-LL-37 alone; 3-ZnO NP + LL-37 95
Figure 6.6. Comparative expression of AKT and ERK in mouse melanoma cells and fibroblast cells 97
Figure 6.7. Relative fold expression of ERK gene in B16F10 cells in response to ZnO and Ni/ZnO NPs 98
Figure 6.8. Relative fold expression of ERK gene in B16F10 cells in response to Ni/ZnO PMC NP 98
Figure A.1. Zinc accumulation in mouse tissues demonstrated by ICP-MS 124
Figure A.2. Biodistribution of ZnO NP demonstrated by fluorescence measurements 125
Figure A.3. Cell density dependent melanoma cell viability in the presence of ZnO NP. BLUE-1000 cells per well; GREY-500 cells per well; GREEN-11000 cells per well 125
Figure A.4. Cytotoxic Activity of nanoparticles in B16F10 mouse melanoma cells at 24h of exposure. A. Untreated Cells B. Cells treated with ZnO C. Cells treated with 0.1% Ni/ZnO 126
Figure A.5. Anti-melanoma activity of ZnO and its PMCs in B16F10 cells at 20µg/ml in the presence and absence of LL-37 126
Figure A.6. Anti-melanoma activity of ZnO and its PMCs in B16F10 cells at 20µg/ml in the presence and absence of LL-37 127

Figure A.7. Dose dependent cell viability of NIH3T3 fibroblast cells in the presence of ZnO NP and its PMCs at 24h 127
Figure A.8. Dose dependent cell viability of NIH3T3 fibroblast cells in the presence of ZnO NP and its PMCs at 48h 128
Figure A.9. Dose dependent cell viability of NIH3T3 fibroblast cells in the presence of ZnO NP and its PMCs at 72h 128
Figure A.10. Dose dependent cell viability of NIH3T3 fibroblast cells in the presence of ZnO NP and its PMCs at 96h 129
Figure A.11. Relative Cytotoxicity in M4 canine melanoma cells following ZnO NP exposure for 24h demonstrated by trypan blue exclusion assay 129
Figure A.12. Relative Cytotoxicity in M5 canine melanoma cells following 0.1% NiZnO NP exposure for 24h demonstrated by trypan blue exclusion assay 130

List of Tables

Table 1.1. Techniques used for the characterization of proteins with nanoparticles 4
Table 2.1. Effects of ZnO-based NPs in rodents 21
Table 3.1. Intratumoral administration of ZnO-poly I:C nanocomplex induces tumor-regulating cytokine response relative to PBS sham injected controls..... 54
Table 5.1. Zeta potential measurements of ZnO NP in response to RBD binding 76
Table 6.1. HESI source parameters used for High resolution mass spectrometry of LL-37 peptide 88
Table 6.2. Primers used for RT-qPCR 91
Table 6.3. Estimation of payload of LL-37 peptide on ZnO NP and 0.1% Ni/ZnO PMC NP 94
Table 6.4. Time (h) at which various nanoparticles demonstrate the highest anti-melanoma activity..... 96
Table 6.5. Nanoparticles showing the highest anti-melanoma activity at 24, 48, 72 and 96h..... 96
Table A.1. RT-qPCR cycling conditions 125

Acknowledgements

Life at Kansas State University has been eventful, I should say, altogether changing me personally as well as professionally. As I finish my Ph.D., I would like to express my gratitude to each and every person who has been a part of this journey.

Foremost, I would like to thank my major advisor, Dr. Robert K. DeLong for being an exceptional mentor. He has been a constant source of support and motivation. Thank you so much for guiding me through these years!

I would like to thank Dr. Mary Lynn Higginbotham, Dr, Santosh Aryal and Dr. Zhoumeng Lin for serving as my supervisory committee members. All your suggestions and support have been extremely helpful.

I would like to acknowledge all our collaborators —at K-state & external—, current and earlier members of DeLong lab— Amanda Hoffman, Jayden McCall, Nina Marchell, Grant Huslig, Miranda Hurst, Vaibhav Murthy, Baolin Wang, Sarah Wilson, Sarah Devader, Mary Post, Juliet Nava, Sunyoung Yoon and Ryan Swanson—, and Aryal lab members—Dr. Tuyen Nguyen, Dr. Ramesh Marasini and Sagar Rayamajhi—for all the support.

I am grateful for the sincere and invaluable support from the faculty and staff of the Nanotechnology innovation Center of Kansas State (NICKS) and the Department of Anatomy & Physiology especially, Marla Pyle, Dr. Tej Shreshtha, Dr. Don Harbidge, Joel Sanneman, Gail Eyestone and Dan Galbraith.

I am very much indebted to all my friends at K-State, and the members of *K-State Cancer Fighters* and the Society for the Promotion of Indian Classical Music and Culture Amongst Youth (*SPICMACAY-KSU*) for making Manhattan, a home away from home. I am thankful to all my friends, near and far, who cheered me on in this venture.

Words fall short to express my immense gratitude to my family. I do not know how to thank my parents—Mrs. Annamma Mathew and Mr. T.A. Mathew—for dreaming big for me, believing in me and supporting me to pursue my passions. Thank you so much for raising me as a kid to stand up for myself. I would like to thank my sister, Mrs. Janita Poornima Mathew and her family for all the love, care and support. How can I not thank Mr. Pius Sebastian, our family-friend, who is more or less like a member of our family, for the very first mentions of the United States of America as a land of possibilities?

It is a never-ending list, I know; but I am grateful to everyone, knowingly or unknowingly, has made this feat possible.

Dedication

To the ever-loving memory of my parents, Mrs. Annamma Mathew

and, Mr. T. A. Mathew

To my mentor, Dr. Robert K. DeLong

Chapter 1 - Introduction

Nanomedicine for cancer therapy

According to the World Health Organization (WHO), cancer continues to be the second leading cause of death worldwide. It is estimated that 1 in 6 deaths are caused by cancer [1]. Nanomedicine is an emerging candidate for cancer therapy that uses different types of nanocarriers such as, lipid-based, polymer-based, inorganic, viral, and drug-conjugated nanoparticles [2]. Size, high surface-to-volume ratio and other physico-chemical parameters make nanocarriers unique [3]. Accentuated drug delivery along with potential applications in diagnosis and imaging makes nanomedicine an appealing candidate in cancer therapeutics [4]. Surface functionalization of nanoparticles with different types of ligands can be used for targeting biomolecules and cells thereby enabling drug delivery and disease diagnosis [5]. By the phenomenon of enhanced permeability and retention (EPR), dependent on the leaky vasculature, nanoparticles can modulate the biodistribution of loaded molecules and increase their accumulation in cancer tissues with leaky vasculature [6,7].

Zinc Oxide Nanoparticles (ZnO NPs)

Zinc is the second most abundant transition metal ion in the body. Approximately 2800 human proteins are zinc-binding. This is one-tenth of the human proteome [8]. In addition to its catalytic role in enzyme activity, zinc ions are involved in the stabilization and folding of proteins, and regulation of cell signaling [9,10]. Zinc oxide (ZnO) is a "Generally Recognized as Safe" (GRAS) chemical according to the United States Food and Drug Administration [11]. ZnO NPs have been associated with a variety of biomedical applications owing to their anticancer, antibacterial, antidiabetic, anti-inflammatory, drug delivery and bioimaging properties [12].

Anticancer Activity of Zinc Oxide Nanoparticles

With its unique intrinsic anticancer activity, physiologically based zinc oxide (ZnO) has been shown to be selectively toxic to a variety of cancer cell types including cancerous T cells, human hepatocellular carcinoma (HepG2), human bronchial epithelial cells (BEAS-2B), human lung adenocarcinoma (A549) cells, human malignant melanoma cells (A375) and mouse skin melanoma cells (B16F10) and human head and neck squamous cell carcinoma (HNSCC) [13–16]. ZnO NP showed a melanoma-cell-selectivity ratio of 39:1 over normal cells [17]. Recent work from our research group have shown ZnO NPs can complex polyinosinic acid: cytidilic acid (poly I:C) RNA which improves ZnO NP inhibition of experimental melanoma [17,18].

The unique surface chemistry of the nanoparticle allows $ZnOH^+$ formation which likely underlies its interaction with the anionic membrane of cancer cells and its drug delivery activity [19,20]. ZnO NP has been associated with an increase in superoxide dismutase activity and generation of reactive oxygen species (ROS) which can also trigger cancer cells to undergo apoptosis [21,22]. Oxidative stress due to the generation of ROS has been associated with the induction of apoptosis in colon cancer cells (Caco-2), hepatocarcinoma cells (HepG2), ovarian cancer cells (SKOV3), cervical cancer cells (HeLa) and human epidermal cancer cells (A431) [12,23–27]. Lysosomal destabilization and an increase in intracellular Zn^{2+} ion concentration were induced in colon cancer cells [12,28,29]. Green-synthesized ZnO NPs induced inhibition of angiogenesis in chick chorioallantoic membranes [30]. Anticancer activity of ZnO NP could be an outcome of its role in humoral and cell-mediated immunity [31]. At sub-cytotoxic concentration (20 µg/ml), ZnO NP has been shown to induce pro-inflammatory cytokine IL-8 in human lung epithelial cells [32].

Zinc-based Physiometacomposites

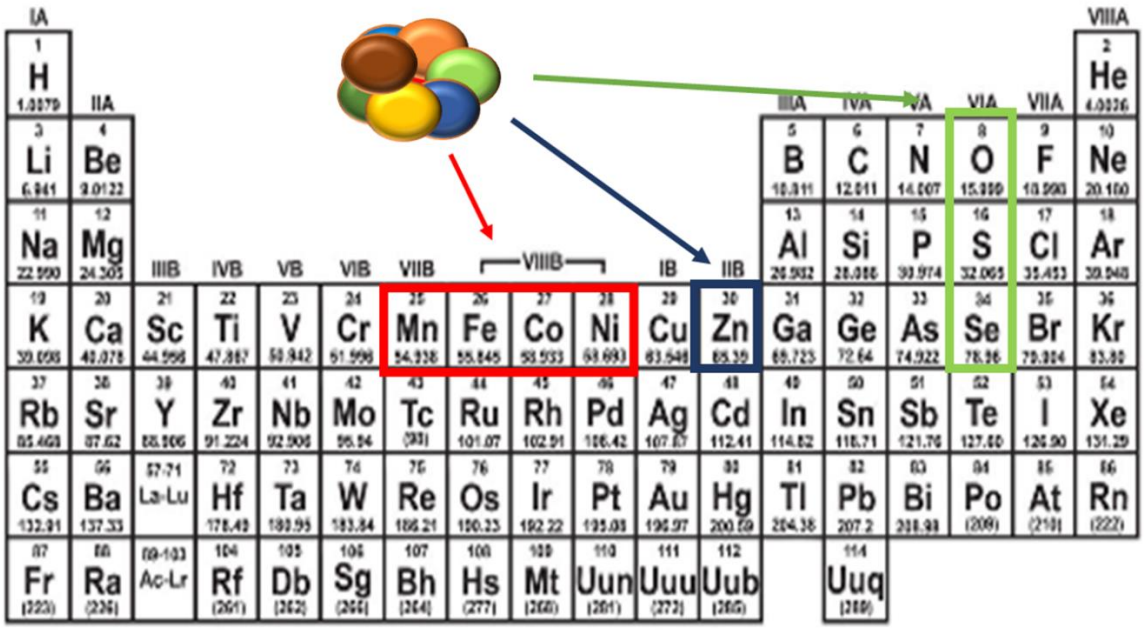

Figure 1.1. Periodic element chart showing Zinc and physiological metals with potential anti-cancer activity

To enhance the anticancer activity of ZnO NP, our research group proposes to explore the outcomes of doping other physiological metals with ZnO/zinc sulfide/zinc selenide as the core nanoparticle. These novel compositions are called physiometacomposites (PMCs). Currently, different percentages of the physiological metals, manganese (Mn), iron (Fe), cobalt (Co) and nickel (Ni) are used to generate zinc-based PMCs.

Investigating the interaction of zinc oxide nanoparticles with proteins

Interaction of proteins with nanoparticle surface leads to protein adsorption on nanoparticle surface mediated by hydrogen bonds, solvation forces, Van der Waals interactions, etc [33]. This formation of complexes is usually referred to as the protein corona on the nanoparticle surface. Hard corona is the irreversible binding whereas soft corona is the reversible binding [34]. ZnO NP interactions with proteins present in simulated biological fluids were measured using the protein fluorescence quenching ratio. One-dimensional gel electrophoresis was used to determine the

adsorption of plasma proteins on the ZnO NP surface, which was further analyzed using two-dimensional gel electrophoresis. Using mass spectrometry, protein corona formation around the NPs was identified. In total, 23 proteins were found to be adsorbed on the ZnO NP surface with serum albumin and fibrinogen being the most abundant [35].

Bovine serum albumin (BSA) was used as a model protein to analyze the protein corona formation around ZnO NPs using spectrophotometry, circular dichroism (CD), Fourier Transform Infrared (FTIR) and High-Resolution Transmission Electron Microscopy (HRTEM). Interaction between ZnO NP and BSA and formation of bio-conjugate was indicated by a shift in the absorption peak of the protein. CD spectrum suggested that BSA changes its conformation when bound to ZnO NP [36].

Interaction of ZnO NPs with biologically relevant proteins such as lactate dehydrogenase (LDH), and two interleukins (IL-6 and IL-8) had been investigated as part of *in vitro* toxicological investigations. Dynamic light scattering was used to analyze hydrodynamic size distribution and zeta potential of ZnO NPs LDH absorbance was found to decrease with increasing ZnO NP concentrations in cell culture medium suggestive of their interaction [37]. Different techniques used for the characterization of proteins with nanoparticles are summarized in Table 1.1.

Table 1.1. Techniques used for the characterization of proteins with nanoparticles

Protein	Nanoparticle	Technique
Bovine Serum Albumin (BSA)	ZnO	UV-visible spectrum, Fluorescence quenching, Circular Dichroism (CD) [38]
BSA	ZnO	UV-visible spectrum,

		X-ray diffraction (XRD), Fluorescence quenching, Fourier-transform infrared spectroscopy (FTIR) [39]
Bovine Plasma Fibrinogen (BPF) and BSA	Titanium dioxide (TiO_2)	XRD, Transmission Electron Microscopy (TEM), Zeta potential, Bicinchoninic acid (BCA) Assay, Raman Spectroscopy [40]
Green fluorescent protein (GFP) with a glutamate-6 tag	Iron oxide (BION)	XRD, TEM, Raman spectroscopy, Zeta potential, SDS-PAGE, CD, ATR-IR spectroscopy [41]
Cell culture proteins	Gold	UV-visible spectrum, DLS and Zeta potential, TEM [42]
Ubiquitin	Gold	NMR [43]

Two-dimensional fluorescence difference spectroscopy (2D-FDS) measures the fluorescence spectrum of nanoparticles and the interaction with proteins can be assessed in terms of fluorescence quenching [18]. Dynamic light scattering is used to measure the size and zeta potential of nanoparticles. Zeta potential is the measurement of the electrostatic potential of the electrical double layer around a nanoparticle in solution. A zeta potential of -10 mV to +10 mV is considered neutral, > +30 mV strongly cationic and < -30 mV strongly anionic [44]. Transmission electron microscopy (TEM) provides information about the particle size, grain size, size distribution, size homogeneity, lattice type, morphological information, crystallographic details and chemical composition of phases distribution [45]. Bicinchoninic acid (BCA) Assay determines

protein concentration in terms of the reduction of cupric ions (Cu^{2+}) to cuprous ions (Cu^{+}) by proteins [46]. Sodium dodecyl sulphate – polyacrylamide gel electrophoresis (SDS-PAGE) is one of the most common methods used to separate proteins present in a sample according to their molecular weight [47].

This dissertation will discuss the interaction of Ras binding domain (RBD) and the dual antimicrobial-anticancer peptide, LL-37 with ZnO NP and its PMCs in chapters 3 and 4.

In vivo Distribution and Tolerance of Zinc Oxide Nanoparticle

Very little is known about the effects of ZnO NP in animal models. Available studies provide variable data on physiological or pathological responses and toxicity. A brief account of the rodent studies done with ZnO NPs is provided in chapter 2 (Table 2.1.) [48]. Labeled with the fluorophore Cy5.5, the biodistribution of ZnO NP at 2 mg/kg dose was assessed in a mouse model. The detailed procedure is provided in the supplemental information.

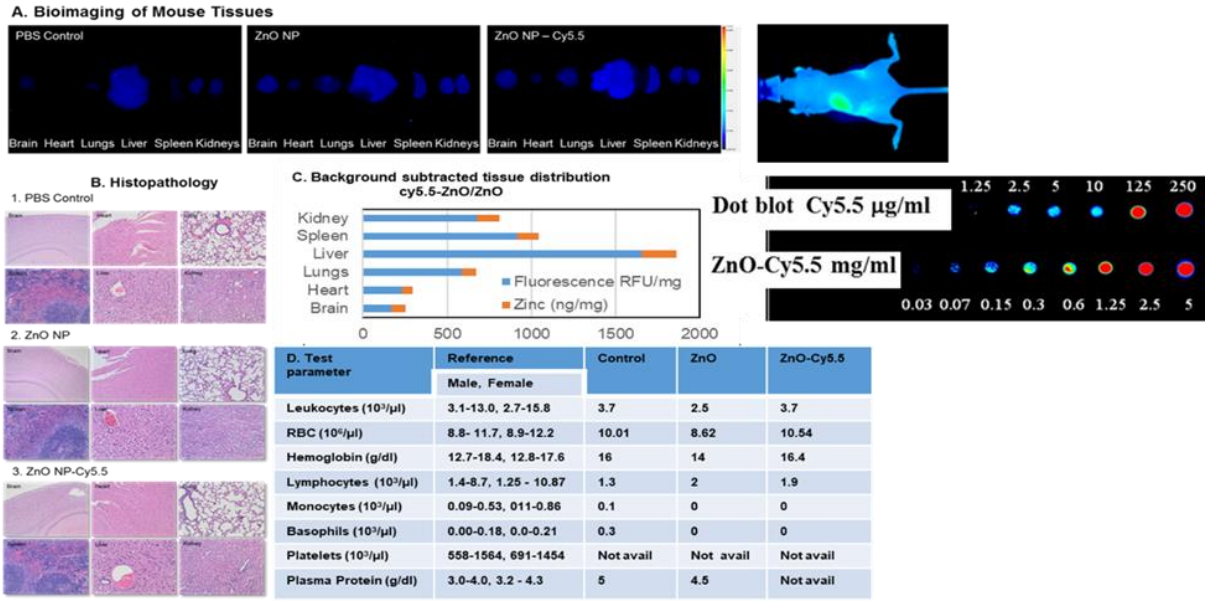

D. Test parameter	Reference Male, Female	Control	ZnO	ZnO-Cy5.5
Leukocytes (10^3/µl)	3.1-13.0, 2.7-15.8	3.7	2.5	3.7
RBC (10^6/µl)	8.8- 11.7, 8.9-12.2	10.01	8.62	10.54
Hemoglobin (g/dl)	12.7-18.4, 12.8-17.6	16	14	16.4
Lymphocytes (10^3/µl)	1.4-8.7, 1.25 - 10.87	1.3	2	1.9
Monocytes (10^3/µl)	0.09-0.53, 011-0.86	0.1	0	0
Basophils (10^3/µl)	0.00-0.18, 0.0-0.21	0.3	0	0
Platelets (10^3/µl)	558-1564, 691-1454	Not avail	Not avail	Not avail
Plasma Protein (g/dl)	3.0-4.0, 3.2 - 4.3	5	4.5	Not avail

Figure 1.2. In vivo biodistribution and tolerance of ZnO NP in mice. A. Bioimaging of tissues from BALB/C mice administered with 100 µl phosphate buffered saline (PBS) control or 2 mg/kg single intravenous dose of ZnO-NP or Cy5.5-ZnO NP-PEG. Tissues were collected post-euthanasia within 30 minutes after administration of PBS, 5 days after

ZnO NP and 6h after Cy5.5-ZnO NP-PEG. B. Histopathology C. Biodistribution of zinc (estimated by ICP-MS) compared to fluorescence in tissues D. Hematology

As shown in figure 1.2., localization of ZnO NP to liver and kidneys was appreciated at 30 minutes post injection of Cy5.5-ZnO-PEG NP. Biodistribution of zinc assessed by ICP-MS was comparable with the fluorescence measurements with the highest accumulation found in the liver. Interestingly, ZnO NP accumulation was found in brain tissue specimen as well. No pathology was seen in the tissues 5 days or 6h after exposure to ZnO-NP or Cy5.5-ZnO NP-PEG respectively.

Melanoma – Overview

Melanoma refers to the cancer of the pigment producing cells of the skin. Malignant melanoma is the most lethal form of skin cancer which becomes extremely dangerous upon metastasis, which means spreading to other organs in the body. Approximately, 2.3% of the population is estimated to be diagnosed with melanoma during their lifetime. Among the different stages of melanoma, the late-stage or metastatic melanoma has the lowest five-year survival rate of 27.3% [49]. Melanoma is associated with the third highest mortality rate amongst all cancer types. Different causes of melanoma include positive family history, personal characteristics, sun exposure over a lifetime, atypical mole syndrome and socioeconomic status.

Mucosal melanoma is a rare disease with a very poor prognosis constituting about 1.4% of all melanomas and 0.03% of all cancer cases [50]. Metastases of mucosal melanoma were found in regional lymph nodes, lung, liver, and distant nodes. Irrespective of their locations, the disease showed similar survival rates over years. The five-year survival rate was found to be as low as 16% [49]. Complete surgical excision is the only complete cure for this disease. However, the anatomical locations are quite challenging for this option.

Uveal melanoma is the most common primary intraocular tumor in adults. Surgical resection, photodynamic thermotherapy, radiation and enucleation are the common modes of treatment for this disease. The highest incidence has been noted in older age groups above 70 years. No targeted therapies are currently approved for treating uveal melanoma [51]. The common sites of metastasis include skin, lung, brain, liver, bone, and intestine [52,53]. Companion animals represent excellent comparative oncology models because of the similarities between canine and human disease [48].

Oncogenic pathways for melanomagenesis

According to the Cancer Genome Atlas, there are four most prevalent mutations causing melanoma – BRAF, *RAS, NF1,* and Triple-WT (wild-type) [54]. However, there is no correlation between the outcome of the disease and its genetic subtype. Mutations in BRAF and RAS are the most frequently encountered genetic alterations in melanoma based on next-generation sequencing (NGS) [55].

The highest incidence of BRAF mutations is associated with melanoma [56]. BRAF mutation leads to oncogenesis through the activation of the mitogen activated protein kinase (MAPK) pathway. Activation of MAPK pathway results in the activation of the enzymes ERK and AKT which is responsible for melanoma progression and metastasis [48]. Mutation in RAS and BRAF along with growth factors can lead to hyperactivation of ERK which is found in 90% of human melanomas [57]. AKT is associated with cell survival, proliferation, cancer promotion, and antiapoptotic signaling through mTOR (mammalian target of rapamycin) and NF-κB pathways in melanoma [58]. Activation of ERK and AKT has been found to be involved in uveal melanoma and mucosal melanoma [59–61]. Sustained ERK and AKT signaling has been associated with resistance to BRAF-targeted drugs [62].

Treatment for Melanoma

Treatment options for melanoma include surgery, chemotherapy, radiation, immunotherapy, photodynamic therapy and targeted drug therapy [63]. The treatment options depend on the behavioral features of the tumor such as location, stage and genetic profile. Surgery is the primary line of treatment for stage I-IIIB melanoma [64]. Even though surgical removal increases the survival rate in the initial stages, it is not enough to treat metastatic melanoma [65]. Therefore, one or more of the other modes of therapy enlisted above are recommended to improve survival as and when required [64]. The use of conventional chemotherapy alone no longer remains a reliable option for treating melanoma. Combining immunotherapy or targeted therapies is the avenue of interest nowadays [50].

Vemurafenib and dabrafenib are BRAF inhibitors that are approved for treating metastatic melanoma [66]. Despite the advent of novel therapies along with conventional treatments, mortality due to cancer is still not under control. The major limitation of the current therapeutic approaches is the lack of selective and targeted delivery to the tumor tissue [3]. This demands the persistent search for better treatment options, both in terms of safety and efficacy. The emergence of new therapeutic targets from genetic profiling and identification of molecular factors involved in melanomagenesis is a promising direction towards efficient melanoma drug discovery.

Use of B16F10 mouse melanoma model for melanoma

Owing to their capacity to elicit distant metastases *in vivo ,* B16F10 mouse melanoma cells are the most widely used metastatic model for preclinical studies [67]. Upon tail vein injection, B16F10 cells produce metastases mainly in lung tissues. However, local injections of these cells including subcutaneous and intradermal, have been found to be inadequate to initiate metastasis [67].

Subcutaneous injection of B16 cells will form a palpable tumor in mice within 5-10 days of administration. This will develop into a 1×1×1 cm tumor in 14-21 days. Beyond this, the tumor tends to necrotize. It is highly recommended to sacrifice the mouse before this. The typical dose used is 1×10^5 cells/mouse, which is 1.5 to 2 times the minimal tumorigenic dose in normal C57BL/6 mice [17,68,69].

Objective of the Dissertation

The comprehensive goal of the proposed research is to elucidate the biophysical, biochemical, and biological mechanism of anti-cancer activity of ZnO NP and its PMCs. An in-depth investigation of the mechanisms and effects is expected to help in molding new therapeutic targets and approaches. For biophysical and biochemical characterization, dynamic light scattering (DLS), two-dimensional fluorescence difference spectroscopy (2-D FDS), transmission electron microscopy (TEM) and inductively coupled plasma mass spectrometry (ICP-MS) have been used. The biological activity of the different nanoparticles was investigated in NIH3T3 mouse fibroblast cells, B16F10 mouse melanoma cells and canine melanoma cells followed by *in vivo* investigation in mouse model. The behavior of the nanoparticles in different mouse tissues was also monitored *ex vivo*. This dissertation presents the significant findings of this study.

Chapter 2 is a detailed review of the anticancer activity of zinc oxide nanoparticles and combining ZnO NPs with nucleic acid therapeutic and protein delivery against metastatic melanoma. This chapter summarizes the current literature about the biochemical effects of ZnO NP on melanoma, its biologic activity, and pharmacokinetics and biodistribution in rodents and its translation potential into spontaneously developing higher animal models of melanoma and other cancers.

Chapter 3 elaborates on the immunological activity of zinc oxide nanoparticle and its anticancer peptide and RNA complexes. The molecular immunogenicity of zinc, cobalt, magnesium, and nickel oxide NPs have been compared finding the superior immunogenicity of ZnO NP *in vitro* and *ex vivo*. *In vitro/in vivo* immunogenic potential of these NPs in complex with an anticancer peptide (ACP) or anticancer RNA (ACR) were also evaluated.

Chapter 4 deals with the characterization of biochemical activities of ZnO NP and its PMCs in terms of inhibition of enzyme activities and associations of enzymes involved in RAS pathway of metastatic progression. This chapter explored the chemical composition of the metamaterials and characterized them by ninhydrin chemical staining, low UV spectral shift and zeta potential analysis. Inhibition of biochemical activity was demonstrated in terms of inhibition of fluorescence and bioluminescence of β-Gal and Luc respectively. Association of multiple enzymes in RAS/ERK/AKT pathway was confirmed by the proteomics analysis of B16F10 metastatic melanoma tumor induced in a BALB/c mouse model. Considering this information along with the fact that antimicrobial peptides such as LL-37 and NZX express anticancer activity, the inhibition of key cellular enzymes may be suggested as the potential mechanism behind the regulatory effects of microbiome on cancer cells.

In Chapter 5, the interaction of ZnO NP with proteins is elaborated using Ras binding Domain (RBD) as the model protein. The physico-chemical properties of ZnO NP of two different sizes — 14 nm and 100 nm — were compared using dynamic light scattering (DLS) and ICP-MS. Formation of RBD-NP complexes were confirmed by fluorescent spectroscopy, DLS and SDS-PAGE. The complex caused cancer cell apoptosis in B16F10 mouse melanoma cells. Intracellular delivery of RBD in combination with ZnO NP may serve as a novel strategy to inhibit the critical

RAS pathway. This *protein interference* approach may have potential as an experimental therapeutic approach against melanoma and potentially other RAS-dependent cancers.

In chapter 6, we investigated the combinatory anti-melanoma potential of ZnO NP and LL-37, an antimicrobial peptide, which is currently in clinical trials against melanoma. LL-37 is an antimicrobial peptide with dual anticancer activity, which is already in clinical trials against melanoma [70]. A similar line of methodological approach as with RBD was used for the characterization of LL-37 interaction with ZnO NP and its PMCs. High-resolution mass spectrometry (HR-MS) was used to assess the purity of the LL-37 peptide. The binding parameters were investigated by the bicinchinonic acid (BCA) assay. DLS and SDS-PAGE were used to assess the binding of LL-37 peptide on the NP surface. Antimelanoma activity of ZnO and its PMC NPs was assessed in B16F10 mouse melanoma cells using MTT assay. RT-qPCR was used to assess the ERK and AKT gene expression in mouse melanoma cells.

Chapter 2 - Translating Nanomedicine to Comparative Oncology—the Case for Combining Zinc Oxide Nanomaterials with Nucleic Acid Therapeutic and Protein Delivery for Treating Metastatic Cancer

[Reprint of the article published in the Journal of Pharmacology and Experimental Therapeutics, Special Issue on Drug Delivery Technologies; R.K. DeLong, Yi-Hsien Cheng, Paige Pearson, Zhoumeng Lin, Calli Coffee, Elza Neelima Mathew, Amanda Hoffman, Raelene M. Wouda and Mary Lynn Higginbotham. Journal of Pharmacology and Experimental Therapeutics September 2019, 370 (3) 671-681; DOI: https://doi.org/10.1124/jpet.118.256230; Copyright © 2019 by The American Society for Pharmacology and Experimental Therapeutics

Abstract

The unique anticancer, biochemical, and immunologic properties of nanomaterials are becoming a new tool in biomedical research. Their translation into the clinic promises a new wave of targeted therapies. One nanomaterial of particular interest are zinc oxide (ZnO) nanoparticles (NPs), which has distinct mechanisms of anticancer activity including unique surface, induction of reactive oxygen species, lipid oxidation, pH, and also ionic gradients within cancer cells and the tumor microenvironment. It is recognized that ZnO NPs can serve as a direct enzyme inhibitor. Significantly, ZnO NPs inhibit extracellular signal–regulated kinase (ERK) and protein kinase B (AKT) associated with melanoma progression, drug resistance, and metastasis. Indeed, direct

intratumoral injection of ZnO NPs or a complex of ZnO with RNA significantly suppresses ERK and AKT phosphorylation. These data suggest ZnO NPs and their complexes or conjugates with nucleic acid therapeutic or anticancer protein may represent a potential new strategy for the treatment of metastatic melanoma, and potentially other cancers. This review focuses on the anticancer mechanisms of ZnO NPs and what is currently known about its biochemical effects on melanoma, biologic activity, and pharmacokinetics in rodents and its potential for translation into large animal, spontaneously developing models of melanoma and other cancers, which represent models of comparative oncology.

Introduction

Cancer and Nanomedicine.

Based on recent World Health Organization estimates, cancer is responsible for nearly one in six deaths and has a significant and increasing worldwide economic impact [1]. Traditional treatment methods including surgery, radiation, and chemotherapy have limited success in controlling metastatic disease. While better therapies are needed for many, if not most, metastatic cancers, the incidence and associated death rate of melanoma (cancer of the skin) continues to climb despite the availability of targeted small molecule inhibitors and newer immunotherapies [71–73]. Thus, additional treatment options are urgently needed for metastatic melanoma.

Importantly in the last decade, nanomedicine has emerged with transformative power and its cancer treatment potential is just beginning to be realized [2,74–76]. While chemotherapy drugs act systemically, once bound to a tiny nanoparticle (NP) with an inversely proportionate large surface area, the drug concentration—and, hence, effective dose delivered—is substantially increased. However, in the absence of a targeting agent such as an antibody conjugated to the NP, NPs indiscriminately bind or enter cancerous and normal cells,

which may result in toxicity and suboptimal tumor targeting, much the same as conventional chemotherapy agents. There are two mechanisms by which NP targeting of tumor cells may be achieved. Passive targeting of NPs occurs because of the small size of the NPs and their ability to carry drug payload into the tumor microenvironment due to its microvascularization, whereas active targeting of NPs occurs due to functionalization of the surface of the NP with, for example, an antibody or aptamer to target a particular receptor on the surface of a cancer cell (Danhier et al., 2010). In addition to targeting and payload advantages, NPs can, in some cases, contribute to anticancer activity. They can also be loaded with nucleic acid therapeutics (NAT) and anticancer protein (ACP) in order to have multiple layers or modes of pharmacologic action. Much effort has been aimed at NP tumor targeting [2,74–79]; however, a significant barrier in cancer nanomedicine remains with regard to effective metastases targeting. This review focuses on the anticancer mechanisms of the zinc oxide (ZnO) NP, a physiologically based metal-oxide NP our group has studied extensively, and what is currently known about its biologic activity. ZnO NPs have the ability to bind, stabilize, and deliver NAT and ACP, thus representing an exciting new strategy in combatting metastatic disease. It has become increasingly important to translate anticancer ZnO NAT or ZnO ACP beyond rodents and into spontaneously developing tumors in large animals such as pet dogs, which represent excellent comparative oncology models for multiple cancer types, including melanoma.

Advantages of ZnO NPs.

A wide variety of NP types has been employed for drug delivery to melanoma as well as other cancer models in animals including, but not limited to, polymers, dendrimers, liposomes, polymeric micelles, nanogels, and microneedles targeting [74–80]. Of the limited amount of data available to date, inorganic nanorod shapes are believed to have slightly higher tumor delivery

efficiency than comparably sized and shaped organic, liposomal, or polymeric NP [81]. Our group has experience with gold (Au)-NP NAT delivery [82,83] including its clinical translation [84]. However, thiol (-sulfhydryl) conjugation is in common use for Au NPs and is unnatural in nucleic acids. Disulfide bonds that stabilize protein structure may be disrupted upon Au-NP nanobio interaction. Instead, in cells and tissues, zinc is best known for stabilizing nucleic acid and protein interactions. In the nanoscale, metals such as zinc are known to oxidize to the metal oxide. Unlike other physiologic metals such as iron, cobalt, and manganese, a significant advantage of ZnO is that it exists in only one chemically stable form (ZnO). More importantly, in the last few years the unique indigenous anticancer activity of ZnO NPs has come to light [13,85–88]. Thus, in the next sections we review what is currently known about the mechanisms of ZnO NP anticancer activity and its biochemical activity and experience in animal models, with a future focus on nanomedicines designed to target NAT and ACP to melanoma and potentially other cancers.

Anticancer Properties of Zinc Oxide

Although the mechanisms by which ZnO exhibits selective anticancer properties are incompletely understood, several themes are beginning to emerge. These include cancer cell susceptibility due to the unique surface chemistry, reactive oxygen species (ROS) generation, intracellular gradients of free zinc ions, and biochemical effects on enzyme activity.

ZnO Surface Chemistry

ZnO is thought to be selective for cancer cells, in part due to its unique surface chemistry. ZnO NPs have been shown to be approximately 28–35 times more toxic to neoplastic T cells than normal cells, suggesting cancer-selective cytotoxicity as one of their innate characteristics [14]. These data are consistent with our work, where we reported a 39:1 selectivity ratio in melanoma [17]. Using reactive molecular dynamic simulations, we reported that ZnO can form $ZnOH^{2+,}$ leading

to positive zeta potential surface charge analysis in water suspension [19]. At low pH, which occurs in cancer cells, this effect should be amplified. Because cancer cells have a higher concentration of anionic phospholipid, the positive charge of $ZnOH^{2+}$ may drive electrostatic interactions at the membrane. Current dogma suggests that this property may underlie both the anticancer and drug delivery properties of ZnO NPs. The surface chemistry of ZnO NPs may also be related to their anticancer activity and ability to induce apoptosis in cancer cells [13].

Reactive Oxygen Species Generation

Zinc oxide is known to generate ROS, which induces apoptosis in cancer cells [13,89]. This is another cancer-selective property since rapidly dividing cells are more susceptible to biomolecular and organellar destruction caused by ROS. The presence of ROS induces redox cycling cascades and depletes the cellular reserve of antioxidants [13]. Once these reserves have been depleted, the presence of ROS will induce apoptosis [13]. In comparing the redox potential of various physiologic metal oxide NPs, linear regression analysis suggests that this parameter is correlated with ZnO NP antibacterial activity [90]. In a comprehensive comparison of BEAS-2B transformed lung cells versus macrophages (RAW 264.7), physiologically based ZnO or cobalt oxide NPs compared favorably versus other metal oxide NPs in terms of the slope of their EC50; however, both NPs exhibited a broad ROS heat map [91]. This aspect likely, again, implicates ZnO NP oxidative activity as an additional mechanism for its cancer cell–selective cytotoxicity.

Intracellular Gradients of Free Zn Ions

Toxicity of ZnO NPs to cancer cells has also been partially attributed to the accumulation of Zn^{2+} in the cytosol of cancer cells [85,87]. Intracellular, cytosolic concentrations of free zinc cations are low and strictly regulated by homeostatic variables [88]. Normal cells reuse and recycle, sequester, or excrete increased Zn concentrations; however, cancer cells, with unregulated growth

and malfunctioning cellular metabolism, may be more susceptible to these ionicity-based mechanisms [85,87].

Biochemical Effects on Enzyme Activity

Reports suggest that zinc and magnesium oxide NPs may act as catalysts [92,93]. There are many classes of enzymes within cancer cells that catalyze important biochemical reactions for cell metabolism, growth, division, etc. Indeed, the effects of NPs on tumor biochemistry and cancer immunology are a critical gap in our knowledge. However, the impact of NPs on the enzymes that regulate these activities is likely an important aspect of their anticancer activity.

At present, there is extensive literature regarding protein interaction to NPs, and the mechanisms of protein and RNA nanobio interaction to a variety of physiologic metal oxides have been characterized [17,19,94–97]. The ZnO NP interaction to protein enzymes inhibits biochemical activity, including model enzymes belonging to the hydrolase class [98(p),99] and the oxido-reductase class [19]. Enzymes from these two classes are important in cancer cell metabolism; when secreted, they can assist in cellular invasion by degrading components of the extracellular matrix. Enzymes in the RAS signaling pathway are activated in many aggressive cancers, and in melanoma this is hallmark. Importantly, we reported on the phosphorylation of extracellular signal–regulated kinase (ERK) and protein kinase B (AKT) enzymes [17]. These data strongly suggest that the ability of ZnO NPs to inhibit enzymes that drive cancer cell progression, drug resistance, and metastasis is of fundamental importance in their anticancer mechanisms. Figure 1 illustrates a cancer cell such as melanoma in the presence of ZnO NPs and the associated anticancer mechanisms (Fig. 2.1.). As shown in figure 2.1., accumulating evidence suggests multiple mechanisms of anticancer activity for ZnO NPs including: 1) unique surface-forming $ZnOH^{2+}$ interacting to anionic cancer cell

membrane, 2) ROS-induced apoptosis, 3) tumor pH-dependent Zn^{2+} disrupting ion homeostasis, and 4) enzyme inhibition.

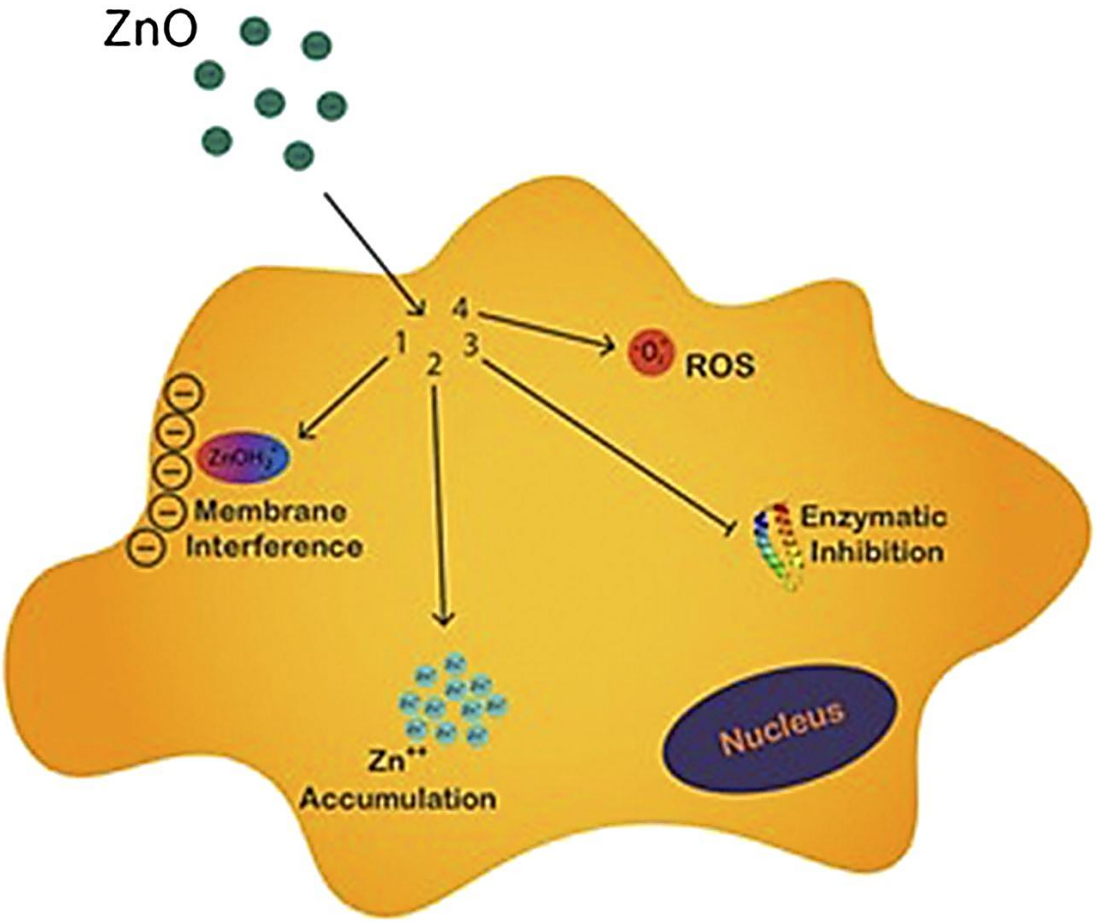

Figure 2.1. Anticancer activity of ZnO NPs. Anticancer mechanisms include ROS, membrane interference, pH-dependent zinc ion flux or gradients, and enzyme inhibition.

Biologic Activity of ZnO NPs in Animal Models

Very little work has been done thus far on ZnO NPs *in vivo* , with much of the literature focused on Au, silicate, and iron oxide (Fe3O4) NPs [82,100–104]. Characterization of the conjugates was shown to be less than 100 nm by transmission electron microscopy and dynamic light scattering. Treated mice experienced no significant weight loss in comparison with control mice and drug could be detected in the plasma for up to 50 hours [101]. In another study, Au NPs were

functionalized with polyethylene glycol (PEG) and/or peptide derived from myxoma virus (MDDRWPLEYTDDTYEIPW) or cyclic arginine-glycine-aspartic acid targeting integrin, which can be confirmed by shifts in the zeta potential surface charge and the molar ratio of peptide to Au NPs based on absorbance spectroscopy. In this case, Au-NP conjugation to the peptide did not appear to impact cell survival, which is consistent with our results for Au-NP short interfering RNA delivery [82,104]. However, functionalization did have a dramatic effect on tissue distribution, specifically early tumor accumulation, clearance from the blood, and urine excretion in the B16 melanoma grafted on C57/BL6 mice [104]. In another study, Nu/Nu mice bearing human M21 melanoma were administered silica NPs radiolabeled with iodine-124; based on radiation dosimetry data, 6.4% of the injected dose was detected within the untargeted and 8.9% within the targeted tumor tissue [100], which is somewhat higher than recent meta-analysis would suggest [81]. Bioimager analysis of Cy5.5-labeleled thermally crosslinked iron oxide suggested organ distribution was in the following order: liver > spleen ∼ lung > kidney > blood > stomach > brain > lymph node > all other organs, based on fluorescent signals in these tissues several hours after intravenous administration [102]. It should be noted that after 3 days, fluorescence in the liver and spleen accounted for >90% of the residual fluorescence with near background levels in all other tissues except kidney and lung. These data may have profound implications for NP targeting, especially for cancers originating in these organs or those with propensity to metastasize to the liver or lung, such as melanoma. Recently, maghemite NPs doped with lanthanide, referred to as magnetic reagent for efficient transfection NPs, have been assessed. When functionalized with polyethyleneimine, magnetic reagent for efficient transfection NPs penetrate SK-OV-3 cells as shown by confocal fluorescence microscopy. Therefore, when loaded with short interfering RNA, these NPs could silence both marker and cancer-associated genes [103]. Importantly,

polyethyleneimine toxicity could be greatly mitigated by ligation to short interfering RNA functionalized magnetic reagent for efficient transfection. These data strongly support NP surface activity, as performed here with RNA functionalization, in the underlying anticancer mechanism.

The Case for Zinc Oxide Nanoparticles

Inorganic NPs are thought to have slightly higher tumor delivery efficiency than comparable sized or shaped liposome or polymer nanomaterials [81]. Data are beginning to emerge that indicate the anticancer activity of ZnO NPs observed in in vitro models may extend into *in vivo* rodent models. One group synthesized core-shell NPs (CSNPs) of Fe_3O_4-ZnO and tested this CSNP in tumor-bearing DBA/2 mice. After peritumoral injection of the CSNP, tumor growth inhibition increased with increasing zinc percentage of the CSNP [81]. Another group tested the toxicity of Fe_3O_4-ZnO CSNPs in C57BL/6 mice receiving subcutaneous injections of 4, 20, or 200 mg/kg dosages of Fe_3O_4-ZnO CSNPs. These mice exhibited no toxicity, with no significant weight loss or food and water consumption changes noted [105]. Table 2 presents an overview of ZnO NP data in mice to date. The nanomaterial synthesis and characterization, as well as the animal model in which testing was performed and the biologic activity data in each model, are briefly summarized.

Table 2.1. Effects of ZnO-based NPs in rodents

NP	**Synthesis**	**Characterization**	**Animal Model**	**Biologic Activity**	**Reference**
Fe-doped ZnO	Atomization of zinc or iron napthenate	TEM	DBA/2 Mice bearing	Luciferase expressing KLN 205 cells	[81]

	with CH4/O2 combustion		KLN 205 tumor	showed tumor growth was inhibited more after peritumoral injection with higher percentages of ZnO relative to Fe.	
Fe_3O_4-ZnO CSNP	Modified nanoemulsion method	TEM (<100 nm) DLS (>100 nm), ZP −16 to −25 mV (in PBS)	C57BL/6 mice	Hematology, serum biochemistry, and organ Zn was assayed by ICP-AES after subcutaneous injection of 4 and 20–200 mg/kg. Some agglomeration and	[105]

				granulomas were observed but no other dose-dependent overt toxicity was reported.	
Cy5.5-ZnO	Cy5-NHS reacted with citrate-ZnO-EDEA	FTIR and optical images of Cy5.5-ZnO NP	Sprague-Dawley Rats	Micro-, nano-ZnO, or dye control was compared after oral administration. Cy5.5 blood concentration peaked at 5 h, and at 7 h was in the order: kidney > liver > lung ~ pancreas > all other tissues	[106]

ZnO	Purchased from Sigma-Aldrich	None shown	Female ICR mice (CLEA, Japan)	A single 0.05 or 0.2 mg/kg dose was given via the tail vein. Zn levels in the blood were followed at 20, 40, and 60 min, and were in the order: spleen ≥ lung ≥ kidney ≥ liver at days 1, 3, and 6.	[107]
ZnO	Purchased from Sigma-Aldrich	None shown	In-bred strains of female Balb/c	A single 500 µl intraperitoneal injection of 0.25, 0.5, 1, or 3 mg ZnO NP. Anaphylaxis score was ZnO < Ova < ZnO-Ova (20% of	[108]

				the ZnO NP mice rubbed their eyes and snout). Histologic differences in the lung, intestine, and spleen were observed and changes in IL-2, 4, 6, 10, and 17; TNF-a; and MHC I and II were observed, presumably at the highest dose.	
NOTA-ZnO-PEG-TRC105	Calcination followed by thiol conversion	TEM, fluorescence spectrum	BALB/c bearing murine	TRC105 functionalized conjugates increase cell	[109]

(targeting antibody)	and maleimide reaction to attach PEG and targeting agent, filter purified, washed with water and ethanol		breast 4T1 tumor	association as shown by CFM. Using PET analysis of Cu-64 conjugates, tumor uptake varies from 6% of administered dose initially to about 4% after 24 h. Histologic analysis confirmed tumor uptake.	
ZnO-Gd-Dox	Zinc methacrylate reacted with AIBN and PEG-methyl	TEM, UV and T1-weighted MR, and UV and PL spectra	BxPC-3 tumor-bearing nude mice	Tumor volume growth vs. initial volume was significantly reduced for	[110]

	ether methacrylate			ZnO-Gd-Dox vs. controls, Significant histologic improvement in tumor.	

As shown in Table 2.1., dosages from 0.05 to 200 mg/kg were tested in mice or rats. Thus far, the synthesis or conjugation method has not been standardized, although both PEG and Cy5.5 tracking dye have been tested, as previously mentioned, with excellent results. The data, thus far, suggest that bioavailability in kidney, liver, lung, and spleen is good. Although little information is available on tumor uptake, two reports suggest significant tumor uptake and histologic improvements of the tumor [109,110]. However, as can be seen there is some interest in doping or functionalizing ZnO NPs, and a variety of different synthetic procedures and characterization methods have been employed. At present, none of these have been standardized nor have they been compared in a standard animal or tumor-bearing model, thus there remains a great deal of work to be done for *in vivo* assessment of ZnO NPs.

Effect of ZnO or ZnO-RNA on Experimental Melanoma in Mice

Currently, there is interest in the nexus between cancer immunology and nanotechnology. The anticancer and immunogenic properties of polyinosinic:polycytidylic acid (poly I:C), a synthetic analog of double-stranded RNA, has long been known. Our group first reported combined antitumor activity of ZnO NPs with poly I:C in the immunocompetent B16F10-BALB/c experimental melanoma mouse model (Ramani et al., 2017). Analysis of the tumor proteome

within this model at the time of metastasis revealed significant ERK and AKT activation in the mice, consistent with what is reported for malignant melanoma in the National Cancer Institute Cancer Genome Atlas [54]. We observed that the ZnO or ZnO/poly I:C NP significantly suppresses the phosphorylation of both these key downstream drivers of melanoma in the mouse model (Fig. 2.2.).

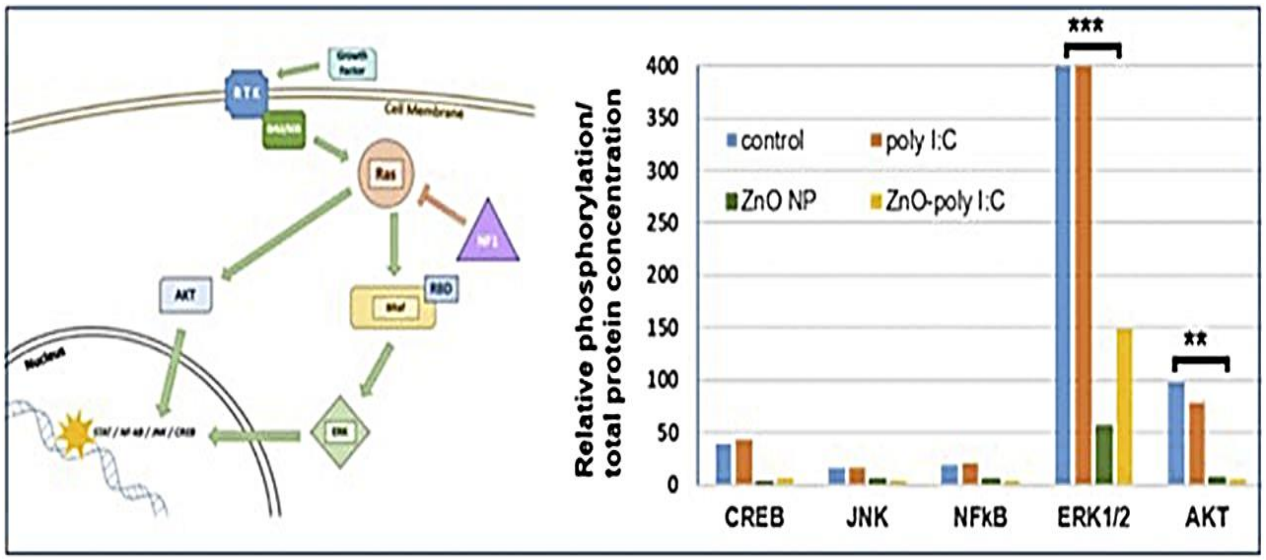

Figure 2.2. Altered NF1-RAS-BRAF axis and interactions in RBD lead to downstream ERK and AKT activation in melanoma tumor at-the-time-of-metastasis [adapted from Ramani et al. (2017a,b) and DeLong et al. (2017)].

As shown in figure 2.2., the majority of human melanomas analyzed by the National Cancer Institute Cancer Genome Atlas have an altered NF1-RAS-BRAF axis, where drug resistance has been linked to an altered splicing and protein interaction in the Ras-binding domain (RBD). Ultimately, this leads to activation of ERK and AKT and is associated with melanoma progression and metastasis. Injection of either ZnO NP or ZnO-poly I:C complexes directly into the tumor causes tumor regression. Analysis of these key drivers of melanoma revealed substantial abatement of both enzymes' phosphorylation, albeit ERK is only partially blocked. These results

suggest that either NAT or ACP, targeting RAS or RBD, could suppress ERK activation altogether and lead to complete melanoma regression.

Pharmacokinetics of ZnO NPs

Pharmacokinetics and Biodistribution of ZnO NPs in Healthy Animals.

Pharmacokinetics (PK) is the science of studying the rate and extent of absorption, distribution, metabolism, and elimination of chemicals, drugs, or NPs by systemically and quantitatively using experimental and mathematical approaches [93,111,112]. PK data provide critical information about the entry of NPs into systemic circulation (bioavailability), their distribution (volume of distribution), and accumulation in the target organs (C_{max} and area under the time-concentration curve), as well as the time required for clearance (mean residence time, clearance, and half-life). A comprehensive review of the PK information of delivered NPs will contribute to designing an optimal therapeutic with higher delivery efficiency to target organs and tissues, maintaining desired therapeutic time, and avoiding unwanted toxicity.

Baek et al. (2012) and Paek et al. (2013) investigated the pharmacokinetics and biodistribution of various sizes of ZnO NPs (20 and 70 nm) in Sprague-Dawley rats following a single oral administration. Their results showed that the absorption profiles in rat plasma were dose dependent with approximate absorption efficiency estimates to be 13%, 25%, and 31% after oral exposure to 50, 300, and 2000 mg/kg of negatively charged ZnO NPs, respectively [113]. However, no significant differences in absorption efficiency were demonstrated between NP size and gender. Similar dose dependency was identified in rat plasma after rats orally received the same doses of positively charged ZnO NPs with lower absorption efficiency estimates of 11%, 15%, and 16%, respectively [114].

Tissue distribution profiles suggest that orally administered ZnO NPs tend to accumulate in lungs, liver, and kidneys of rats, regardless of NP size, surface charge, or gender [113,114]. Long-term exposure of 50, 500, and 5000 mg/kg ZnO NPs added in the diet of Institute of Cancer Research mice from week 3 to 35 suggests higher Zn accumulation in liver, pancreas, kidney, and bones [115]. After intravenous injection of 10 and 71 nm neutron-activated ^{65}ZnO NPs, the liver, spleen, kidneys, and lungs were determined to be target organs with 10 nm ^{65}ZnO NPs being most widespread in lungs, revealing a size-varied biodistribution effect [116]. Li et al. (2012) reported that 93 nm ZnO NPs in male Institute of Cancer Research mice following intraperitoneal injection were more effectively distributed to liver, spleen, kidneys, lungs, and heart, compared with their distribution to liver, spleen, and kidneys after oral administration [117]. In summary, liver and kidneys are likely to be common target organs, regardless of the various physicochemical properties of ZnO NPs, administration routes, and experimental species. Note that the primary excretion pathway of Zn is via feces, while urinary excretion through kidneys only plays a minor role following different administration routes [113,114,116,118].

Pharmacokinetics and Biodistribution of ZnO NPs in Tumor-Bearing Animals

Over the past decade, unique physicochemical and biologic properties of engineered NPs have led to key biomedical applications for diagnosis and cancer targeting therapy. However, the translation of nanomedicine into clinical applications is limited partly due to low delivery efficiency to the tumor and lack of knowledge on the quantitative effects of various physicochemical factors of NPs on tissue/tumor distribution. Therefore, systemic understanding of PKs in NP delivery to tumor using mathematical approaches may significantly contribute to NP-based anticancer drug design with higher tumor delivery efficiency and optimal therapeutic index [81]. In view of the optimal design of nanomedicine with higher targeting power in cancer

therapy with lower toxicity, the biodistribution of administered Zn-associated NPs with increased accumulation in the tumor and decreased accumulation in normal tissues, especially for liver and kidneys, is desired [119]. There are only limited PK studies using Zn-based NPs to investigate the NP tissue/tumor biodistribution in tumor-bearing animals. The focus of this review is on representative articles associated with the effects of various NP physicochemical properties and targeting strategies (i.e., passive vs. active targeting) on tumor delivery efficiency of ZnO NPs.

Hong et al. (2015) employed radiolabeled targeting ligand (TRC105) conjugated ZnO NPs to examine the differences in tumor delivery efficiency between passive (64Cu-C12H21N3O6-ZnO-PEG-NH2) and active targeting NPs (64Cu-C12H21N3O6-ZnO-PEG-TRC105) at 0.5, 3, 16, and 24 hours following intravenous injection using a positron emission tomography imaging method. Comparing the differences in tumor accumulation, there was an approximate 2.5-fold enhancement in tumor delivery efficiency with active targeting TRC105 nanoconjugate of 4.9% of the injected dose per gram of tissue over passive targeting ZnO NPs of 1.9% of the injected dose per gram of tissue at 24 hours post intravenous injection into 4T1 tumor-bearing mice. In addition, the uptake of 64Cu-C12H21N3O6-ZnO-PEG-TRC105 was demonstrated mainly in the 4T1 tumor compared with the major organs or tissues except liver and spleen that were responsible for primary clearance [109]. Higher tumor accumulation of active targeting doxorubicin-loaded folate conjugated Zn(II)-crosslinked polymeric nanohydrogels (FPZCLNs-15) was also indicated by Zhang et al. (2016) compared with the accumulation of passive targeting NPs (PZCLN-15) in the H22 tumor in tumor-bearing mice following intravenous injection (~1.4-fold higher). It is worth noting that a favorable biodistribution with lower doxorubicin accumulation in liver and kidneys and higher tumor delivery was demonstrated by Zhang et al. (2016) [120].

Physiologically Based Pharmacokinetic Model for ZnO NPs

Besides traditional pharmacokinetic analyses, another technique that can integrate and compare PK data derived from healthy and tumor-bearing animal studies in order to gain deeper insights into the biodistribution and tumor delivery of administered NPs is physiologically based pharmacokinetics (PBPK) modeling [121–123]. PBPK modeling is a mechanistic and mathematical modeling approach based on the physicochemical properties of NPs coupled with anatomy and physiology within a living body with organs and tissues interconnected by blood flow to characterize the process of absorption, distribution, metabolism, and elimination. The advantages of implementing PBPK models include their great extrapolation power across doses, routes, and species, as well as the ability to predict target tissue and in-site tumor dosimetry from various external administrations, which is important in nanomedicine applications. Among the few available PBPK models developed for metallic NPs [124–129], only one PBPK modeling study was developed to describe the tissue biodistribution of ZnO NPs in healthy mice [126]. Chen et al. (2015) developed a perfusion-limited PBPK model for healthy mice to simulate the target tissue pharmacokinetics of 10 and 71 nm ^{65}ZnO NPs and ^{65}Zn(NO3)2, including blood, brain, lungs, heart, spleen, liver, gastrointestinal tract, kidneys, and carcass up to 28 days after intravenous injection via tail vein. Specifically, they estimated the time-dependent partition coefficients and excretion rates based on previously published biodistribution data of healthy mice. The developed PBPK model reasonably predicted target tissue distribution of ZnO NPs with mean absolute percentage of error estimates of <50%. Currently, there is no PBPK modeling framework available for tumor-bearing animals to simulate nontumor and tumor tissue distribution and to facilitate the design of new NP-based anticancer drugs with higher tumor targeting efficiency and optimal therapeutic index. To gain more insight into the PKs of delivered ZnO NPs in nontumor as well as

in-site tumor tissues in tumor-bearing animals, a PBPK modeling framework in tumor-bearing animals needs to be developed, which is our future direction.

Comparative Oncology

Animal models have long provided the means to test novel anticancer agents and diagnostic modalities in a preclinical setting. Such animal models function as the final filters in selecting drugs for clinical trials. Although rodents are most frequently used in this setting, and do provide some distinct advantages in terms of experimental tractability, there are also well-recognized limitations of the mouse model. Murine models often lack key characteristics of human cancers, such as long latency, genomic instability, and heterogeneity among the tumor cells and the surrounding microenvironment. Consequently, the immensely complex biology of cancer development, recurrence, and metastasis is not sufficiently recapitulated in mice, and unfortunately these limitations are often reflected in the unacceptably high drug candidate attrition rate of subsequent clinical trials [130–140].

Larger animal models, specifically dogs, have been gaining traction over the preceding decade as preclinical and early clinical models to facilitate the drug and diagnostic development pathway, and our canine companions possess several advantages over traditional rodent models [130–140]. Of the approximately 70 million pet dogs in the United States, it is estimated that one in four will develop cancer during their lifetime, and nearly 50% over the age of 10 years will die as a result [141,142]. Dogs spontaneously develop many of the same malignancies as people as they age, and have intact immune systems compared with rodent models. Because they are physiologically similar, share environmental exposures without unhealthy habits, and have access to high level healthcare, dogs function as ideal comparative models for human disease. Canine and human tumors also share genetic complexity, overlapping mutations, similar tumor microenvironments,

potential for therapeutic resistance, and in many cases similar responsiveness to conventional therapeutics. When practically considered, cancer evolves comparatively quickly in the dog, such that the time from carcinogen exposure to disease development is shorter, disease progression is more rapid, and therapeutic responses are observed more expeditiously; therefore, answers to critical questions can be obtained more readily and cost effectively [130–140].

Several canine cancers have demonstrated applicability as translational models [143] including non-Hodgkin's lymphoma [144], osteosarcoma [145], urothelial cell carcinoma [146], brain tumors [147], and malignant melanoma [148]. These canine tumors share histologic appearance, genetic and/or molecular aberrations, biologic behavior, and response to specific therapeutics with their human counterparts [143–148]. A pertinent example is malignant melanoma [148]. In humans, melanoma most often arises in the skin and is associated with lack of pigmentation and UV light exposure. It is estimated that it will be responsible for approximately 10,000 cancer-related deaths this year alone in the United States [149]. Melanoma is diagnosed in nearly 100,000 dogs per year in the United States [150] and most commonly develops in the oral mucosa. Oral melanomas typically exhibit aggressive local behavior and frequent metastasis [151,152], warranting a poor prognosis with short survival times for affected animals. Currently, the management of melanoma in dogs is similar to the disease in humans with initial therapy aimed at local disease control, utilizing a combination of surgery, radiation therapy, chemotherapy, and immunotherapy [151–153].

Human cutaneous melanomas often contain an activating BRAF mutation [56,151,154], resulting in constitutive mitogen-activated protein kinase pathway activation. Other activating mutations recognized include RAS (~20%) [155], NF1 (~25%) [156], and occasionally KIT [157]. However, some have no documented mutations and are considered triple wild-type melanoma [54]. The similarities between human and canine melanoma were compared by the Comparative

Melanoma Tumor Board [97], which found substantial common characteristics between human mucosal and canine melanoma [97,158] and confirmed that canine melanoma dysregulates and constitutively activates the mitogen-activated protein kinase and PI3K/AKT pathways.

With evidence of activation of the same molecular pathways in human and canine melanoma, canine malignant melanoma is an excellent translational model for drug-resistant BRAF-mutated melanoma as well as melanoma with a triple wild-type phenotype [97,158,159]. Because of the disease similarities, the dog provides an outstanding model for further investigation into melanoma pathogenesis as well as the development of urgently needed novel therapeutic interventions for this devastating disease in dogs and humans alike.

Conclusions and Outlook

In conclusion, nanomedicines are becoming a vital new weapon in the cancer treatment arsenal. This is especially important for highly metastatic cancers such as melanoma, where treatment options beyond the newer kinase inhibitors and immunotherapies are currently limited. One approach gaining acceptance within the community that presents a potential solution to this complex problem is to use a physiologically based nanoparticle with intrinsic or indigenous anticancer properties, such as ZnO, and to load it for delivery with NAT and ACP, which can target the molecular basis for metastasis.

Such combinatorial bionanotechnology is an exciting possibility with a number of compelling and distinct advantages. As such, the surface properties of ZnO NPs provide a substrate to attach the NAT and ACP, yet also enable ROS, Zn ions, and membrane interactions, which underlie its anticancer activity. So, too, ZnO NPs can act as a direct enzyme inhibitor, in some cases inhibiting oxido-reductases, hydrolases, and synthetases generally thought to be important in cancer, or as is the case for treating melanoma with ZnO NPs, inhibiting transferases such as

ERK and AKT kinases, which have been directly linked to melanoma progression and metastasis [17,54,69].

Although there is a limited data set for ZnO NPs *in vivo*, the data thus far appear very promising. Oral doses of 50–2000 mg/kg have been tested with bioavailability ranging from 11% to 31% and distribution in the liver, pancreas, kidney, and bones observed. After intraperitoneal administration of ZnO NPs, uptake was seen primarily in the liver and kidney but was also notable in lung and spleen. These data are highly favorable for delivery of NAT, ACP, or other types of anticancer therapies to cancer in these organs by ZnO NPs. Although there are very few studies thus far for ZnO NPs in mice, particularly tumor-bearing animals, based on the data shown in Table 1 these results look promising with tumor delivery efficiencies of more than the 0.9%–1% efficiency expected for inorganic NPs [81]. Furthermore, data for ZnO NPs loaded with doxorubicin suggest redirection of the drug from liver and kidney to the tumor, and targeting of ZnO NPs to tumor is facilitated by monoclonal antibody conjugation [110].

Comparative oncology studies in the dog as a model for melanoma and other cancers has a number of distinct advantages. These include (but are not limited to) latency of disease, genomic instability and heterogeneity, microenvironment surrounding the tumor, common cellular and molecular features, and others. Besides malignant melanoma, other cancers considered as comparative oncology models are non-Hodgkin's lymphoma [148] osteosarcoma [149] (American Cancer Society, 2018), urothelial cell carcinoma [160], brain tumor [153], and others. For malignant melanoma, clinical management is also similar in dogs and humans; however, the options for advanced disease are limited, making the search for a nanomedicine approach an important prerogative. Although the characteristic BRAF and RAS mutations are not prevalent in canine melanoma, constitutive activation of the mitogen-activated protein kinase and PI3K/AKT

pathways is hallmark. Given that ZnO NP treatment significantly inhibits ERK and AKT activation of murine and human melanoma in cell culture and mice (Fig. 2), the activity of ZnO NPs on canine melanoma is of considerable importance and is currently being assessed.

On the Horizon

The ability of ZnO NPs to deliver biomacromolecules into cancer cells makes this treatment option an attractive mechanism by which to potentiate cancer therapy by combining its attractive anticancer activity with other drugs, NAT and ACP, or immunologically active compounds. Indeed, the excellent antitumor activity of zinc-doped superparamagnetic iron oxide nanoparticles combined with the anticancer immunopotentiator RNA, poly I:C, and small molecule, imiquimod, has recently been reported against experimental melanoma [161](Bocanegra Gondan et al., 2018). Zinc-doped superparamagnetic iron oxide nanocrystals exhibited excellent magnetic properties and could be visualized by magnetic resonance imaging after peritumoral administration. This combination protected against melanoma challenge and also had significant therapeutic activity against established disease. Hence, it is likely that such combination nanomedicines will be necessary to combat metastatic disease.

Due to their exquisite sequence selectivity, NAT delivery by ZnO NPs holds promise in targeting RAS and other important pathways contributing to cancer drug resistance and metastasis. Thus far, three classes of NAT have received clinical approval: antisense, splice switching oligomer, and aptamer, albeit, not yet for cancer indication [162–164]. Previously, we reported on antisense oligomer targeting K-RAS against experimental pancreatic cancer in mice [165]; however, for melanoma, as shown in figure 2, alterations in the NF1-RAS-BRAF nexus are implicated in the majority of human melanomas analyzed thus far by the National Cancer Institute Cancer Genome Atlas Program [54]. Furthermore, kinase inhibitor resistance in melanoma develops

primarily due to splicing alterations in the RBD [166] (Salton et al., 2015), which leads to altered interactions with RAS [167]. Since this is upstream of both ERK and AKT, this is a highly attractive target. To address this, we are studying the interaction and delivery of the RBD itself as a decoy, and have designed RBD-specific switching oligomer or aptamer sequences for targeting RAS by NAT [168]. As a first approach, we modified the full-length RBD aptamer with a phosphorothioate backbone, which has improved tumor delivery efficiency, target affinity, and *in vivo* stability [165,169]. In this case, since its RBD interaction site is known and the bases implicated in RBD interaction have been identified by nuclease mapping [170], it was possible to retain these as RNA. The remaining structural portion of the molecule could be further stabilized by DNA substitution to create a DNA-RNA hybrid molecule replacing uracil with deoxyuridine (Fig. 2.3.).

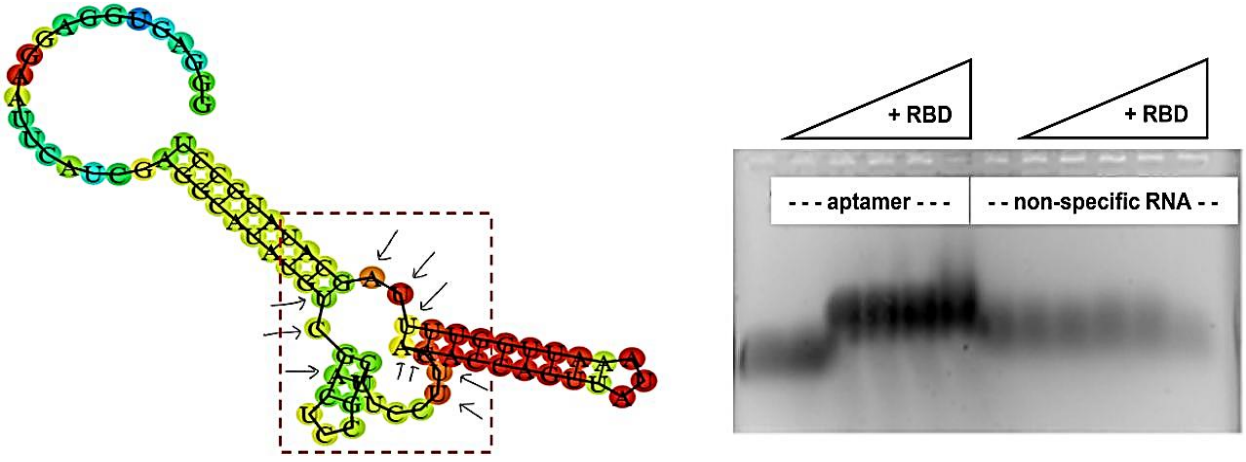

Figure 2.3. (Left) RNAfold predicted structure for full-length RBD-specific aptamer with interaction site in the hashed box and bases known to interact with RBD retained as RNA indicated by arrows. (Right) Specificity of its interaction to RBD is shown by the gel shift with micromolar affinity vs. nonspecific RNA control (torula yeast RNA). RBD was tested at 0, 1:10,000, 1:1000, 1:100, or 1:10 dilution of stock at constant RNA concentration (100 µg/ml).

The RNAfold (Institute for Theoretical Chemistry, University of Vienna) computational prediction for the full-length RBD-specific aptamer, where target interaction is confirmed by gel shift, is shown in figure 2.3. Thus far, we do know that interaction of RNA (poly I:C) to ZnO NPs improves its resistance to RNase A digestion and degradation from exposure to serum, liver, or

tumor homogenate [99]. However, based on the ZnO NP strength of interaction to the RBD (Kd < 10−5) and the fact that this interaction inhibits enzyme activity [19,98,99], its impact on RNA structure, function, and activity is at present a critical unknown. When ZnO NPs are incubated with either torula yeast RNA or poly I:C, we observe a distinct gel shift with an associated change in fluorescence intensity, suggesting a strong interaction between the NP and RNA (DeLong Lab, n.d.; Ramani, et al., 2017; Ramani,et al., 2017). However, the mechanism of ZnO NP RNA interaction and structure-function impact is poorly understood. Based on our Raman and Fourier-transform infrared spectroscopy studies of ZnO NP interaction to adenosine triphosphate or inosine and cytosine model molecules, stabilizing ionic interactions occur primarily through the phosphodiester backbone but also through what appear to be hydrogen bond–type interactions to the various nucleic acid functional groups [18,172]. However, based on our recent liquid chromatography analysis, amino acid interactions to ZnO NPs appear to be much more complex [19] and need to be further studied for both NAT and ACP. When poly I:C is incubated in the presence of ZnO NPs and analyzed by circular dichroism spectroscopy, there appears to be little structural disturbance [168]. Recently, we patented two-dimensional fluorescence difference spectroscopy as a new quality control assay for measuring nanoparticles, and more importantly their biomolecular interaction [173,174]. Based on two-dimensional fluorescence difference spectroscopy, utilizing a magnesium-doped ZnO NP synthesized by our collaborator, we do see evidence that the surface of the ZnO NP enables coattachment of both aptamer and its protein target [174]. Furthermore, in the case of the most well-characterized aptamer-thrombin system, introduction of ZnO NPs does not appear to interfere with the binding isotherm of this interaction [174]. However, it remains to be seen whether NAT- or ACP-bound ZnO NPs are physicochemically stable in biologic media, are able to functionally deliver these biomacromolecules in order to retain

target interaction and biochemical activity in cells and tissues, and ultimately be used for effective tumor or metastasis delivery *in vivo*. This is, quite obviously, an important research goal moving forward.

Targeting Metastases

Despite a strong body of literature utilizing antibody-targeted NPs for drug delivery to tumor [75,76], there is a movement to simplify the use of antibodies by using synthetic, less immunogenic substitutes; for example, using RNA such as poly I:C, aptamer, or shorter peptides. These may contribute less untoward autoimmunity, which will limit the ability to readminister the nanomedicine. Use of poly I:C–targeted superparamagnetic iron oxide nanocrystals may improve delivery to the lymphatic system [175], which is a common site of metastasis. Although poly I:C TLR3 signaling is well known, other receptors such as MDA5 and signaling mediated by antibacterial peptide LL-37, may target the surface of both lung and metastatic melanoma cells [176–178]. Anticancer activity is associated with a portion of the LL-37 sequence, which bears significant homology with several other ACP classes [179]. These data suggest that LL-37–derived ACP may serve as a melanoma-specific or lung cancer–selective targeting peptide. Through comparative proteomics analysis, it may be possible to design metastasis-targeting peptides in order to better address multifunctionalized anticancer NPs for delivery to sites of metastases in the creation of antimetastatic nanomedicines.

Acknowledgements

R.K.D. acknowledges the start-up received from the Nanotechnology Innovation Center at Kansas State, which supported E.N.M. and A.H.

Authorship Contributions

Participated in research design: Pearson, Hoffman, Mathew, DeLong.

Conducted experiments: Cheng, Lin, Coffee, Wouda, Higginbotham.

Wrote or contributed to the writing of the manuscript: Higginbotham, DeLong.

Chapter 3 - Comparative Molecular Immunological Activity of Physiological Metal Oxide Nanoparticle and its Anticancer Peptide and RNA Complexes

[Reprint of the article published in Nanomaterials; Robert K. DeLong, Jeffrey Comer, Elza Neelima Mathew and Majid Jaberi-Douraki. Nanomaterials 2019, 9(12), 1670; https://doi.org/10.3390/nano9121670]

Abstract

Currently, there is a great interest in nanoparticle-based vaccine delivery. Recent studies suggest that nanoparticles when introduced into the biological milieu are not simply passive carriers but may also contribute immunological activity themselves or of their own accord. For example there is considerable interest in the biomedical applications of one of the physiologically-based inorganic metal oxide nanoparticle, zinc oxide (ZnO). Indeed zinc oxide (ZnO) NP are now recognized as a nanoscale chemotherapeutic or anticancer nanoparticle (ANP) and several recent reports suggest ZnO NP and/or its complexes with drug and RNA induce a potent antitumor response in immuno-competent mouse models. A variety of cell culture studies have shown that ZnO NP can induce cytokines such as IFN-γ, TNF-α, IL-2, and IL-12 which are known to regulate the tumor microenvironment. Much less work has been done on magnesium oxide (MgO), cobalt oxide (Co3O4), or nickel oxide (NiO); however, despite the fact that these physiologically-based metal oxide NP are reported to functionally load and assemble RNA and protein onto their surface and may thus also be of potential interest as nanovaccine platform. Here we initially compared in vitro immunogenicity of ZnO and Co3O4 NP and their effects on cancer-associated or tolerogenic cytokines. Based on these data we moved ZnO NP forward to testing in the *ex vivo* splenocyte

assay relative to MgO and NiO NP and these data showed significant difference for flow cytometry sorted population for ZnO-NP, relative to NiO and MgO. These data suggesting both molecular and cellular immunogenic activity, a double-stranded anticancer RNA (ACR), polyinosinic:poly cytidylic acid (poly I:C) known to bind ZnO NP; when ZnO-poly I:C was injected into B16F10-BALB/C tumor significantly induced, IL-2 and IL-12 as shown by Cohen's d test. LL37 is an anticancer peptide (ACP) currently in clinical trials as an intratumoral immuno-therapeutic agent against metastatic melanoma. LL37 is known to bind poly I:C where it is thought to compete for receptor binding on the surface of some immune cells, metastatic melanoma and lung cells. Molecular dynamic simulations revealed association of LL37 onto ZnO NP confirmed by gel shift assay. Thus using the well-characterized model human lung cancer model cell line (BEAS-2B), poly I:C RNA, LL37 peptide, or LL37-poly I:C complexes were loaded onto ZnO NP and delivered to BEAS-2B lung cells, and the effect on the main cancer regulating cytokine, IL-6 determined by ELISA. Surprisingly ZnO-LL37, but not ZnO-poly I:C or the more novel tricomplex (ZnO-LL37-poly I:C) significantly suppressed IL-6 by >98–99%. These data support the further evaluation of physiological metal oxide compositions, so-called physiometacomposite (PMC) materials and their formulation with anticancer peptide (ACP) and/or anticancer RNA (ACR) as a potential new class of immuno-therapeutic against melanoma and potentially lung carcinoma or other cancers.

Keywords: nanomaterials; molecular immunology; molecular dynamic simulations; tumor immunology biostatistical analysis

Introduction

There is a great deal of current interest in nanoparticle delivery of vaccines and immuno-therapeutics [180,181]. Whereas lipid nanoparticle formulations are in common use, inorganic nanoparticles may act synergistically to induce a beneficial immune response in concert with vaccine antigen or RNA immunogen [176]. For example, physiologically-based zinc oxide (ZnO) nanoparticles (NP) or their composites with iron oxide in complex with a drug and/or RNA with poly inosinic:poly cytdylic acid (poly I:C) generate potent antitumor immunological responses against experimental melanoma in immuno-competent mice [161]. Poly I:C-iron oxide nanoparticle complexes have also been used for immune cell targeting [175]. Certain cytokines such as interleukin-6 (IL-6) are thought to play a key role in cancer progression and resistance to therapy [182]. Whereas others such as IL-1, IL-4, IL-10 may be involved in cancer tolerogenicity [183]. Indeed other cytokines such as IL-2, IL-2, TNF-α, and IFN-γ are thought to regulate the metastatic tumor niche and play a key role in regulating cells of the immune system recruited into this environment [176]. Therefore the effect of inorganic NP such as ZnO and others or their RNA and peptide complexes on tumor associated cytokines is a very important question.

Thus far, much of the work on the immunological activity of ZnO NP has been done in cell culture against a variety of different cell types. Some but not all of these were cells of the immune system or from appropriate tissue compartments where these cells reside such as the skin and spleen. For example treating neutrophils or THP-1 cells with ZnO NP has been shown to affect the expression of a variety of different CD molecules, whereas in PBMC (peripheral blood mononuclear cells) induction of IFN-γ, TNF-α, and IL-12 was reported [184]. That same report referenced an earlier work where ZnO NP-treated RAW264.7 cells (a macrophage line) or bone marrow derived dendritic cells (BMDC) also induced CD and MHC mRNA expression as well as

IL-1β and various chemokines (CXCL-5, 9, and 10) [184]. Our lab reported that nanoparticle delivery of tuberculosis antigen 85B induced IL-2 as a bio-marker of antigen presentation in a T cell co-culture assay [82]. We noted molecular and cellular immunogenic activation upon nanoparticle exposure in the *ex vivo* splenocyte assay [185] or after direct intradermal or intratumoral administration [15,83,186]. Therefore here we endeavored to compare the molecular immunogenicity of zinc, cobalt, magnesium, and nickel oxide NP, finding that the ZnO NP generated superior immunogenicity in these in vitro and *ex vivo* assays. We then evaluated the *in vitro*/*in vivo* immunogenic potential of these NP in complex with an anticancer peptide (ACP) or anticancer RNA (ACR).

Materials and Methods

Materials

ZnO nanoparticles (NP) and MgO NP were obtained from Sigma-Aldrich (St. Louis, MO, USA) and the nickel oxide NP (NiO) were synthesized as a grey-white powder by our collaborator (Kartik Ghosh, Missouri State University Department of Physics and Materials Science). The purity and elemental composition of all materials were confirmed by elemental analysis and their size was confirmed <100 nm either by dynamic laser light scattering spectroscopy or transmission electron microscopy within the Nanotechnology Innovation Center Kansas State (NICKS, Manhattan, KS, USA). Materials were washed with USP grade 70% ethanol/water followed by pure alcohol, dried in a sterile hood, suspended in sterile phosphate buffered saline (PBS) buffer and sonicated for several minutes in a probe sonicator to disburse the suspension prior to administration to cells or tumor in a 200 microliter volume containing 20 μg/mL NP.

Cytokine Panel

This experiment was conducted similarly to Murray et al. [187]. Briefly, 105 neonatal human epidermal keratinocytes (HEK) were seeded in 96-well plates and treated with nanoparticle concentrations of 1.25, 2.5, 5, 10, 20, 40, 80, 160, and 320 μg/mL for 24 or 48 h. At the end of each time point, the conditioned media was harvested to obtain cytokine levels. Samples were analyzed on the Milliplex analyzer with the detection limit for the analytes IL-1b, IL-6, IL-8, IL10, and TNF-α was between 2.1 to 2.8 pg/mL. The coefficient of variation (CV) of the analysis varied from 0.79% to 40.6% with a median CV of approximately 7–8% depending on the cytokine and NP concentration. The data plot shown in figure 3.1. (B) inset were obtained from treating HeLa cells with Co3O4 NP and imaged according to manufacturer's recommendations using the Cytoviva® nanoscale microscope (Olympus BX51) and hyperspectral imaging (Auburn, AL).

Ex vivo Splenocyte Assay

Briefly, this assay was also conducted similarly to what we previously described [185]. Mouse spleens were collected from donor mice from the laboratory of Dr. Sherry Fleming (Kansas State University Biology Department). The spleen was isolated and minced in buffer, the cells were separated from the tissue fragments and incubated in PBS buffer containing a 20 μg/mL suspension of the nanoparticles after which the cells were stained with propidium iodide and analyzed by flow cytometry (BD FACSDiva, Warwick, RI, USA) by the Kansas State University Veterinary Diagnostic Laboratory. The cells separated into two populations in the all event forward scatter (FSC-A) and gated in the P1 and P2 channel (PE-A). The ratio of these two populations from two different trials is plotted in figure 3.2.

High Throughput Tumor Proteomics Analysis

BALB/c mice were inoculated with a B16F10 tumor and treated with ZnO-poly I:C complex, as previously described; computational analysis for Table 3.1. was performed using MATLAB® R2019a. Data for high throughput tumor proteomics analysis were collected in a spreadsheet (Microsoft Excel® 2016, Microsoft Corporation, Redmond, WA, USA) for subsequent calculation using (x,y) protein locations. The mean ± SEM (standard error of the mean) were estimated for each set of proteins (probesets). In total, we conducted experiments for unique proteins, approximately 300 (9 × 31) probesets. Each probeset includes a group of six experiments. Pixel intensities at a wavelength of 532 nm, based on mean and standard deviation analysis, were used to reflect the relative abundance of all proteins in the tumor. Group differences amongst probesets were evaluated with the assumption that data were not normally distributed using Kruskal–Wallis ANOVA on ranks for independent unequal-sized data to perform follow-up multiple comparison tests and identify most significant probesets. P-values for statistical significance were set to ≤ 0.05.

Effect size calculation: A sample-based effect size is distinguished from the test statistics. For independent samples, effect size from Cohen's d is determined by calculating the mean difference between your two groups (μ_1: control vs μ_2: treated), and then dividing the result by the pooled standard deviation.

Effect size = $\mu_1 - \mu_2$ / pooled s

where the pooled standard deviation is obtained by

pooled s= $\sqrt{(n_1-1)s_1+(n_2-1)s_2 / (n1+n2-2)}$

We can interpret the effect size measures by the values of Cohen's d [188,189]; small: 0.2, medium: 0.5, large: 0.80, very large: 1.20, and huge: 2.0. This shows that TNF-α has a medium effect size, IL-2 shows very large effect size, and the other cytokines have huge effect sizes.

Molecular Dynamics

A slab of ZnO was constructed based on the wurzite crystal structure and simulated under the ReaxFF force field [190] using the program LAMMPS [191]. This slab was periodic along the x and y axes, while the surfaces perpendicular to the z-axis, Zn-terminated {0001} facets, were exposed to an aqueous region consisting of 311 water molecules. After equilibration at a temperature of 300 K and pressure of 1 atm, the dimensions of the ZnO slab converged to 20.1 × 17.7 × 8.5 Å3. This ZnO structure was replicated 6 × 6 times to produce a continuous slab with dimensions of 120.6 × 106.2 × 8.5 Å3, a size suitable for simulations with the LL-37 peptide. For accurate representation of the peptide conformational transitions and better computational efficiency, all further simulations were performed using nonreactive force fields, with the protein described by the CHARMM36m force field [192] and the ZnO described by a CHARMM-compatible force field for ZnO parameterized using experimentally derived adsorption free energies for small molecules on ZnO nanoparticles [193]. The model of the LL-37 peptide was constructed from the NMR structure of the human form [194]. It was initially placed 20 Å from the ZnO surface. Three different initial conditions were created by rotating the peptide 0°, 90°, and 180° around its helical axis, causing a different set of residues to be facing the ZnO surface in the three replicas. The system was filled with water, giving it mean periodic dimensions of 120.6 × 106.2 × 78.7 Å3. Na+ and Cl− ions were added to obtain an electrically neutral system containing NaCl solution at ≈150 mmol/L. Molecular dynamics simulation was performed using the program NAMD 2.13 [195]. Mass repartitioning of non-water hydrogens enabled the use of a 4 fs timestep [196]. Rigid water molecules

were implemented using the SETTLE algorithm [197]. After 50 ps of equilibration in which the atoms of the peptide were restrained to their initial positions, a 500 ns production simulation was performed for each replica. During these simulations, the temperature was maintained at 295 K by a Langevin thermostat and the pressure, at 1.0 atm by a Langevin piston barostat [198].

IL-6 Assay

This assay followed our collaborators' previously reported conditions except the BEAS-2B cells were cultured and exposed to 10 ug/mL nanoparticles spun down in the presence of 1.3 μg/mL poly I:C and/or LL-37, and IL-6 production relative to LPS or mock infection or medium only controls was assayed by ELISA[178].

MTT Assay

This assay was conducted as we previously described [19]. Briefly 8000 B16F10 cells were added per well of a 96-well plate and treated with 20 mg/mL ZnO-NP loaded in the presence of 3 mM LL37 or carboplatin sedimented from those suspensions and taken up in 10% FBS/DMEM and added to the cells. The cells (n = 3 wells/treatment group) were incubated for 96 h and assayed by MTT on a plate reader (Molecular Devices Corp.) at 562 nm absorbance. The plotted bars are the means with standard error shown.

Results and Discussion

In Vitro Immunogenicity

Our early work suggested particle delivery into the skin can generate significant protective immunity [83,186]. ZnO and Co3O4 NP have been evaluated against macrophages (RAW264.7) and transformed lung cells (BEAS-2B) [91]. Co_3O_4 NP have been shown to penetrate human skin and shown some toxicity and immunostimulatory properties when pulsed with macrophages [199,200]. Thus, here we investigated ZnO and Co_3O_4 NP in vitro immunogenicity head-to-head when

exposed to a standard human skin cell line, human epidermal keratinocytes (HEK) [187]. In this experiment HEK cells were incubated for 24 and 48 h with NP and their cytokine panels measured by milliplex analyzer (Fig. 3.1.).

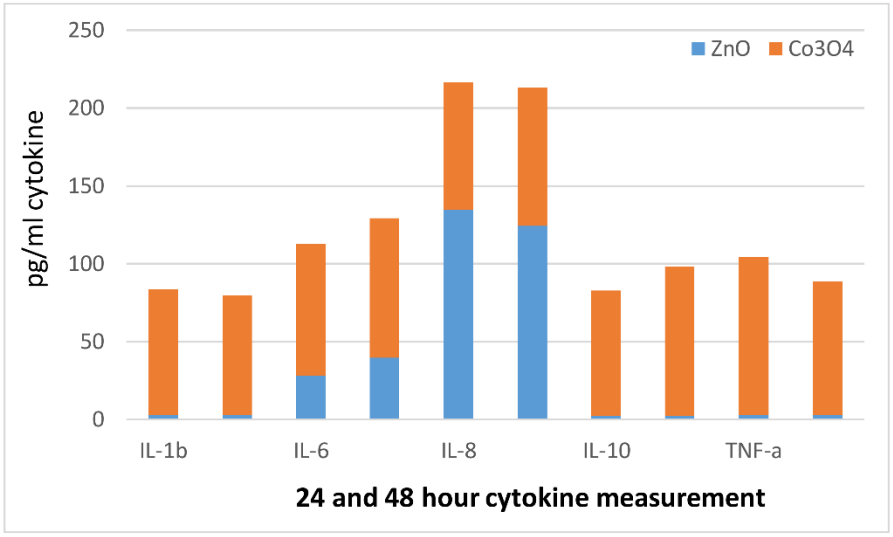

(**A**)

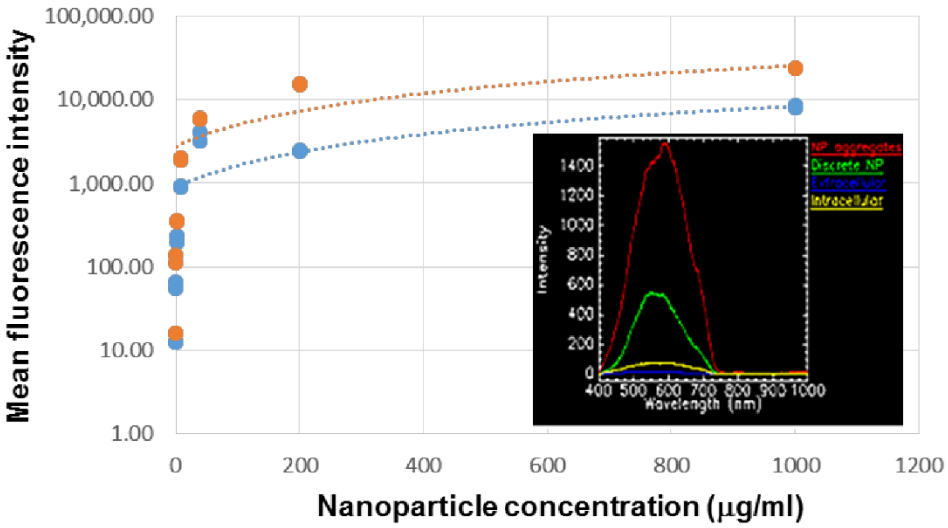

(**B**)

Figure 3.1. (A) Comparing in vitro immunological activity for two physiological metal oxide nanoparticles (NP). (B) Dose-response of NP on IL-8 (inset plots HSI results for Co_3O_4 NP)

Figure 3.1. shows a comparative cytokine panel for an 80 ug/mL dosage of either ZnO or Co_3O_4 NP after 24 or 48 h in the left or right bar respectively. With the exception of IL-8, the

induction of cancer promoting or tolerogenic cytokines was in the order; Co_3O_4 NP > ZnO NP. Dose-response is shown in figure 3.1. indicating maximal effect occurs at about 80 ug/mL NP concentration in which case the induction of cytokine begins to top out. Hyperspectral imaging (HSI) experiments confirmed Co_3O_4 intracellular uptake (data not shown) and the summary plot of this data is shown in the inset in figure 3.1. (B).

Ex vivo Splenocyte Assay

Although iron oxide nanoparticles have been clinically approved and elevated IL-8 levels have been seen when administered systemically, there is some concern reported for their splenic toxicity [201]. The spleen is a rich source and depot of immune cells. Therefore, we investigated ZnO NP in an *ex vivo* splenocyte assay similar to our earlier report [185]. In this experiment we compared ZnO to nickel oxide (NiO) or magnesium oxide (MgO) NP, where our group and one other have shown that these compositions may be able to functionally load protein or protein-RNA complexes onto their surfaces [18,202,203], making their baseline immunogenicity of great interest as a potential carrier of peptide/protein or RNA-based immuno-therapeutics. Based on earlier dose ranging experiments and our experience, splenocytes were incubated with a 20 μg/mL dose of ZnO, MgO, or NiO NP [69,82,185,201,202]. Splenocytes were isolated from the mouse spleen, exposed to concentrations and stained with propidium iodide (PI) and the cell populations separated and counted by flow cytometry (Figure 3.2.).

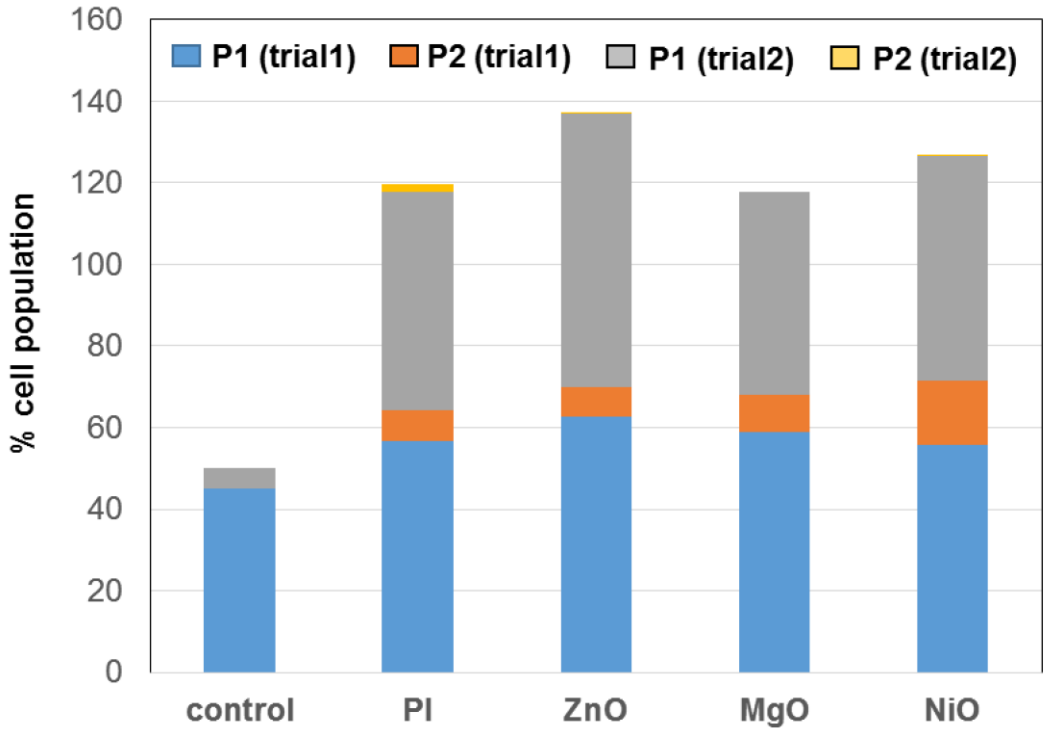

Figure 3.2. Comparing activity of the physiological metal oxide NP by ex vivo splenocyte assay.

As seen in figure 3.2. the sorted splenocyte cell populations after PI staining were distinct for ZnO NP in each trial in comparison to untreated or PI treated controls or the other two physiological metal oxide NP tested, MgO or NiO NP. Based on the cellular and molecular immunogenicity of ZnO NP we investigated the immunological activity of loading it with anticancer peptide and RNA described next.

In vivo Direct Intratumoral Injection Model

Poly inosinic:poly cytidylic acid (poly I:C) is an RNA immunogen used widely in cancer research [161,175,176]. In a relatively recent report we reviewed the molecular cell immunology of the metastatic tumor niche and the cytokines which are thought to regulate it [176]. We previously characterized the interaction of poly I:C to ZnO to form poly I:C-ZnO nano-complexes [18] and consistent with another recent study [161], demonstrated inhibition of experimental melanoma in B16F10-BALB/c mice by poly I:C-ZnO nano-complexes relative to ZnO NP or poly I:C controls

[69]. Analysis of the poly I:C-ZnO-treated tumors relative to control mice receiving sham PBS intratumoral injection in this immuno-competent B16F10-BALB/c mouse model demonstrates significant antitumor cytokine response (Table 3.1.). In the figure 3.3., binding isotherm of poly I:C onto 14 nm zinc oxide (ZnO) nanoparticle measured by the loss in UV absorbance at 260 nm as a function of increased mass per volume (NP) added is shown. This data is in concordance with other measurements in which we have studied the poly I:C nanobio interface to ZnO NP [18]. The table below summarizes cytokines which are thought to regulate immunology of the melanoma metastatic tumor microenvironment and their putative role [176]. Tumors exposed to poly I:C-ZnO had from a 5.8-fold to as much as a 148-fold increase in these antitumor cytokines, the significance of which was demonstrated by Cohen's d effect size [188,189].

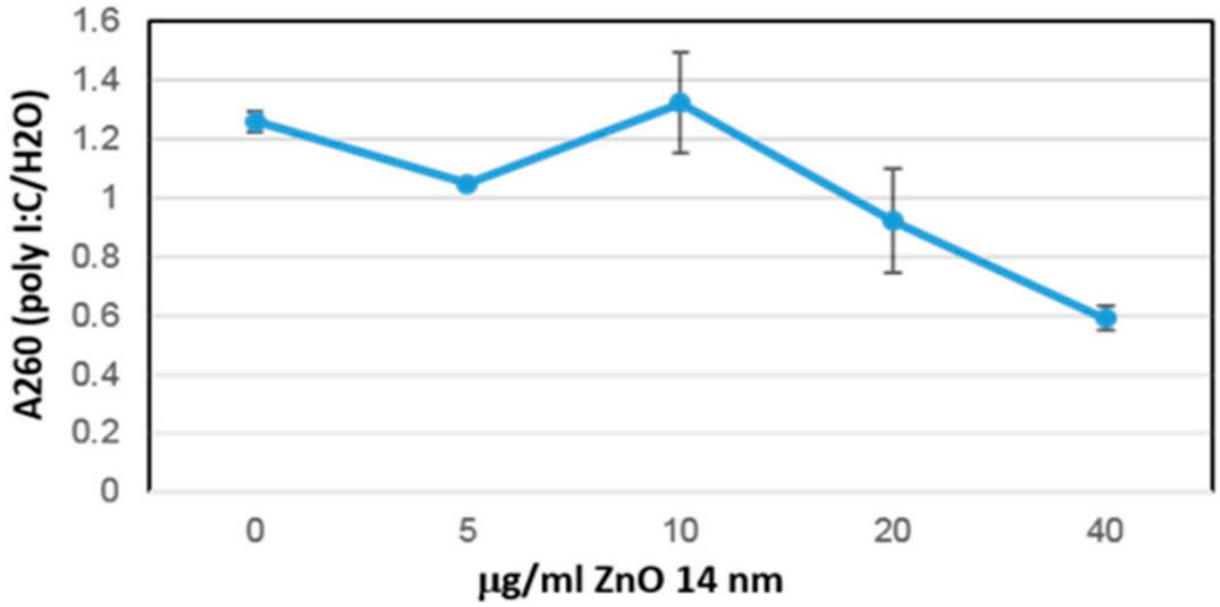

Figure 3.3. Loss of poly I:C from water supernatant as it associates to ZnO NP after brief spin down in micro-centrifuge.

Table 3.1. Intratumoral administration of ZnO-poly I:C nanocomplex induces tumor-regulating cytokine response relative to PBS sham injected controls.

Cytokine	Putative Role in Metastatic Tumor Niche	Effect of ZnO-Poly I:C (Fold Over Control)	Effect Size Analysis (Cohen's d Measure)
NF-α	Chemotaxis, leukocyte recruitment, extracellular killing	148.3+/−33.7	−0.59
IFN-γ	Secreted by cancer, T, natural killer (NK) cells and macrophages (Macs), MHCI/II, involved in Th1 and Th2	6.0+/−0.92	−2.81
IL-2	CD8 and NK activation, activates antigen presentation and B cell response (BCR)	5.8+/−3.2	1.24
IL-12	Growth factor, increases NK action, stimulates antibody production	9.9+/−4.3	18.58

Immunological Activity of ZnO NP Antimicrobial Peptide Complexes

LL-37 is an antimicrobial peptide currently in clinical trials as an intratumoral injection immuno-therapy against melanoma [70]. LL37 binds poly I:C and is thought to partially inhibit its TLR3 based signaling in some cells of the immune system as well as BEAS-2B transformed lung cells [178,204]. Molecular dynamic simulations indicated LL-37 interacts with the surface of ZnO NP and we were able to use its RNA binding properties to assemble RNA-peptide nanoparticle (RNP)

onto ZnO NP testing the ability of these novel co-conjugates to inhibit BEAS-2B interleukin-6 (IL-6) expression by ELISA (Fig. 3.4.).

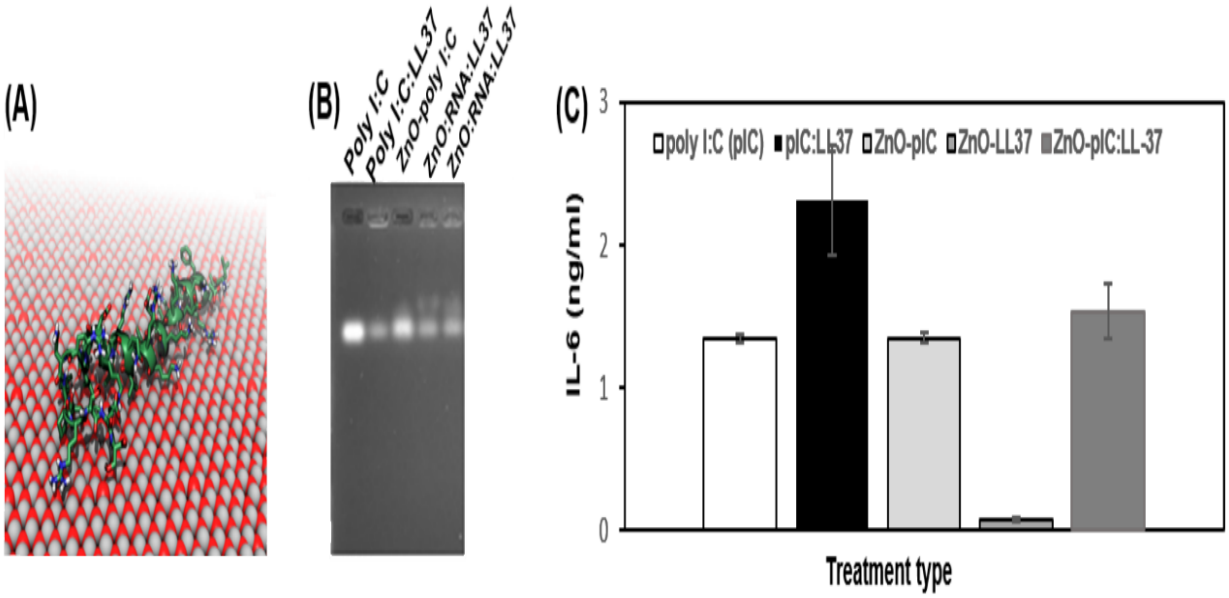

Figure 3.4. Interaction of LL37 to ZnO NP as shown by molecular dynamic simulation (A), electrophoretic gel mobility shift (B) suppresses IL-6 cytokine secretion by BEAS-2B transformed lung cells (C).

As shown in figure 3.4. (A), the molecular dynamics simulations showed a strong interaction between the ZnO surface and the LL-37 peptide. Within 10 ns, the peptide adsorbed to the ZnO in all three simulations. Despite beginning with different orientations of peptide, the final structures in these simulations were remarkably similar. Over the course of 100 ns, the peptides reoriented in such a way that the hydrophobic side chains of the residues L1, L2, F6, I13, F17, I24, F27, L28, L31, and V32 made direct contact with the surface, while most of the charged residues, including D4, K8, K12, R19, D26, and R29, remained extended into the solution. During the remaining 400 ns of simulation, the peptide conformations remained stable, retaining most of their native α-helical structure. A gel shift effect was observed consistent with LL37 binding poly I:C [178] as well as ZnO interacting with both poly I:C or poly I:C-LL37 (9B). Interestingly the delivery

of these co-complexes to BEAS-2B transformed lung cells resulted in significant IL-6 suppression by ZnO-LL37 and not the RNA or RNA-peptide complex (Fig. 3.4. (C).

Combination Therapy Experiment

As shown in figure 3.5. next we investigated whether loading ZnO-LL37 with chemotherapy drug would improve cytotoxicity to B16F10 melanoma cells (Fig. 3.5.).

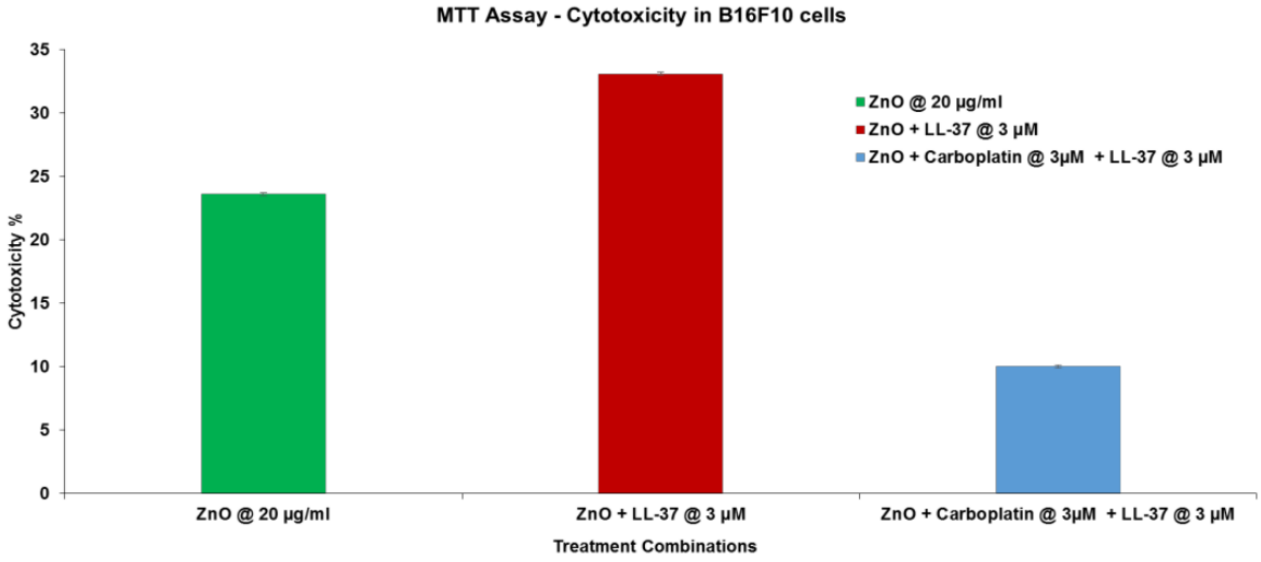

Figure 3.5. Cytotoxic activity of ZnO, ZnO-LL37 or ZnO-LL37/carboplatin combination.

As shown in figure 3.5., loading the ZnO-LL37 complex with melanoma-specific chemotherapy drug did not show any additional advantage. In this case ZnO NP gave 20% cytotoxicity, the ZnO-LL37 increase cytotoxicity to 30%, but at an equivalent dose (3 µM) and exposure (96 h) we observed no advantage of the additional drug.

Conclusions

Overall these data suggest that the physiological metal oxide NP are likely to be quite variable in their immunological activity dependent on the composition and the protein and RNA to which they are complexed. This can be seen as shown in figure 6 at a dosage of 80 µg/mL in the differential effects of ZnO or Co_3O_4 NP on IL-8 considered an immuno-toxicity marker versus

IL-6 considered a pro-cancer cytokine associated with drug resistance [176,182]. ZnO activity was further distinguished in the *ex vivo* splenocyte assay [185] where relative to MgO or NiO NP differences in the two distinct propidium iodide populations were shown, these data suggesting distinct activity of these metal oxide NP on splenocytes as well. Complexation of ZnO to immunogenic RNA (poly I:C) or anticancer peptide (ACP) such as LL37 also had quite distinct effects, in the former case inducing cytokines associated with regulating the metastatic tumor niche (Table 3.1.) and in the latter inhibiting pro-tumor cytokine (Figure 3.4.). These data suggest that the anticancer immunity of either ZnO-RNA or ZnO-peptide will likely need to be evaluated on a case by case basis and may vary depending on the cell type, tissue and tumor to which they are administered. A recent report suggests that loading liposome with butyric acid may lower IL-8, IL-6, TNF-α, and TGF-β similar to our data [205]. Combination therapies show great promise such as the recent report by Serri et al. who used nanoparticles loaded with quercetin and gemcitabine and surface-decorated with hyaluronic acid (HA) which improved anticancer activity and lowered their interleukin profile [206]. An analogous LL37/carboplatin co-loaded ZnO NP formulation did not show combination or synergistic effects. This suggests future work on surface decoration of ZnO NP may warrant further investigation.

Author Contributions

R.K.D. mentored the work, collated the data and wrote the paper, E.N.M. performed the MTT experiment and analyzed the data, M.J.-D. performed the tumor proteomics data and statistical analysis and Cohen's d significance effect test; J.C. did the molecular dynamics simulation shown in figure 3.4. (A).

Funding

This work was funded in part from an Innovative Research Award from the Kansas State University Johnson Cancer Research Center. Simulations were performed on the Beocat Research Cluster at Kansas State University, which is supported in part by NSF grant CHE-1726332.

Acknowledgments

We would like to thank Cheng Kao (Indiana University), Nancy Monteiro-Riviere (Kansas State University Nanotechnology Innovation Center), and Sheri Fleming (Kansas State University Department of Biology) for their assistance with the IL-6 ELISA and cytokine panel assays and provision of mouse spleens. Former students Stanislaw Warcholek, Mary Post, Grant Huslig and Nina Marchell were involved in data collection, operated the flow cytometer, and/or assisted with the ex vivo splenocyte and tumor cytokine data organization or ran the gel electrophoresis, stained and imaged the gels.

Conflicts of Interest

The authors declare no conflicts of interest.

Chapter 4 - Challenging the tumor-microbe biomolecular interface: characterizing antimicrobial physiometacomposite, RNA and protein nanoparticle interactions, enzyme inhibition, signaling and splicing changes in metastatic melanoma cells and tumor

Abstract

Microbiome regulates cancer, the impact of introducing antimicrobial physiometacomposite RNA and protein nanoparticles into metastatic tumor environment unknown. Chemotherapeutic zinc oxide (ZnO) nanoparticle antimicrobial activity correlates with beta-galactosidase (β-Gal) inhibition, its anticancer/antitumor activity well-accepted. Metamaterials combine the advantage of multiple elements in the nanoscale, cobalt (Co) and nickel (Ni) libraries have been described, here this physiometacomposite (PMC) space was rationally explored combining Zn, Co, Ni, Mg, Fe, Mn as binary, ternary, quaternary or higher-order oxide or sulfides. β-Gal and Luciferase (Luc) interaction was characterized and dose-dependent PMC inhibition (e.g. MnZnO, MnZnS Co/ZnO, Ni/ZnO) quantified by fluorescence and bioluminescence assays, inhibiting cell morphology, invasion and 3-D spheroid metastatic phenotype. Altered RAS/RBD interaction and splicing cause ERK/AKT activation in drug-resistant metastatic melanoma. Circos plot proteomics confirmed this, the multi-node drugged by PMC-RBD or splice-shifting-oligomer (SSO). These data suggest antimicrobial physiometacomposite (PMC) RNA and protein nanoparticles may regulate molecular cell metastasis mechanisms.

Introduction

Metamaterials or nanoparticle composites have unique physico-chemical properties [207,208]. Nanoparticle libraries containing cobalt (Co) and nickel (Ni) were synthesized in the context of small quantities of precious metals [209]. ZnO NP antimicrobial activity has been correlated to β-Gal enzyme inhibition [98] and its selective anticancer activity against a variety of different cancer lines has been shown [210]. While *in vivo* ZnO NP anticancer studies are few [48], elegant comparative whole body *in vivo* tolerance studies in zebrafish strongly support its incorporation with cobalt oxide (Co_3O_4) and nickel oxide (NiO) [211,212].

Materials and methods

Materials

Obtained β-Galactosidase (β-Gal) from *Aspergillus oryzae* from Sigma Aldrich (≥8.0 units/mg solid, Louis, MI, USA) and was diluted to a 1 mg/kg solution in spectral grade H20. β-Gal substrate, Resorufin β-D-galactopyranoside was purchased in a 10 g vile from Marker Gene Technologies (Eugene, OR, USA) and was diluted down into ten 10 mg/kg aliquots in spectral grade H20 and re-suspended into a 1 mg/kg solution for experimentation. Excitation (ex) and emission (em) were given by Marker Gene as 573 and 585 nm respectively. Acquired Sigma-Aldrich Luciferase (Luc) enzyme (Photinus pyralis, ≥10x1010 (units/mg) protein) and diluted it to a .2% solution [1:500 dilution with PBS buffer]. Luc enzyme-substrate buffer (ATP, Mg) was diluted and frozen into [1:1] filtered PBS buffer aliquots. Silver (Ag) and Magnesium Oxide (MgO) were purchased from Sigma-Aldrich (St. Louis, MI, USA) at 150 and 50 nm respectively. 80 and 50 nm Aluminum (Al) NPs were synthesized by nanoComposix (San Diego, CA, USA). 44.15 g NanoArmor and 51.71 g Alfa Aesar Titanium Dioxide (TiO_2) NPs were purchased from Thermo Fisher Scientific (Waltham, MA, USA). Copper (Cu), Boron Carbide (B_4C), Zinc Oxide

(ZnO), were purchased from PlasmaChem GmbH (Berlin, Germany), 10-100 nm in size. 3/97% Manganese Zinc Sulfide (MnZnS), 5/95% MnZnS, 1/99% MnZnS, 50/50% Nickel Zinc Oxide (NiZnO), 5/95% NiZnO, 1/99% NiZnO, 0.1/99.9% NiZnO, Zinc Sulfide (ZnS, 180S), ZnS (130S) and Iron Zinc Sulfide (FeZnS) were all synthesized by Dr. G Glaspell's laboratory (Virginia Commonwealth University). Cobalt Oxide (Co3O4), Nickel Oxide (NiO), 2/98% Cobalt Zinc Oxide (CoZnO) and 5/95% CoZnO were synthesized by Dr. KC Ghosh's laboratory (Missouri State University). PMC composite synthesis was as recently described [7], briefly, pure powders were physically mixed, heated to a flux, allowed to cool in oxygen-purged atmosphere and jet ball milled to nanoscale. The NPs were washed with double-distilled ddH20, 70% ethanol/water, ethanol, and were stored dry prior to use. Costar (Corning, NY, USA) 96-well black, clear bottom assay plates were used for the assays. Ras Binding Domain (RBD) protein was obtained from Millipore (Cat# 14-863) and polyinosinic: polycytidylic acid [poly(I:C)] from Sigma-Aldrich (Cat# P958250MG). Cy5.5-labelled SSO (sequence: 3-CCUCUUACCUCAGUUACA-5) was obtained from Trilink Biotechnologies. RT-PCR primers—(Forward: 5'-ACACTTGGTAGACGGGACT-3'. Reverse: 5'-GAGGCACTCTGCCATTAATCT-3') were obtained from IDT. B16F10 and A375 were obtained from ATCC. All NP and RNA were precipitated from 70% alcohol/H2O washed once with 100% alcohol, air dried in the biosafety cabinet prior to RNA and protein complexation, cell or animal administration.

Methods

β-Gal and Luc assays. These were conducted essentially similar to our previous reports [213,214]. ***Fluorescence/bioluminescence readings:*** ZnO, NiO, and Co3O4 nanomaterials were incubated with β-Gal (20 µl) at a concentration of 1, 2, 5, 10, 50, 100, 200 and 400 µg/ml dose in Costar (Corning, NY, USA) 96-well black, clear-bottom assay plates. Cu, 50/50% NiZnO, NiO,

MnZnS, and FeZnS nanomaterials were incubated with Luc (10 µl) in Costar (Corning, NY, USA) 96-well, white polystyrene assay plates with a rounded bottom. Fluorescence was determined by the SpectraMax i3x by Molecular Devices (San Jose, CA, USA). The plate was agitated for 5 seconds before fluorescence readings were taken at an em/ex of 570/590 nm for β-Gal and bioluminescent readings for Luc taken at 578 nm, each with their respective nanomaterials.

MTT assay and proteomic microarray analysis: MTT assay and proteomic microarray analysis were performed according to manufacturer's instructions, the latter using Cancer Signaling Phospho Antibody or Cytokine Profiling Antibody array (Full Moon Biosystems, Sunnyvale, CA, USA). Mouse tumor was isolated at the time of metastasis, 20 mg samples lysed, the proteins extracted (2-3 tumors were pooled), and standardized to A280 (Molecular Devices Spectramax i3x, Sunnyvale, CA, USA). Slides were incubated with Cy3-Streptavidin (Sigma Aldrich, St. Louis, MO, USA), dried by centrifugation and stored under dark conditions, and imaged using Molecular Devices Genepix 4000B (Sunnyvale, CA, USA).

Circos high throughput tumor proteomics analysis: In total, we conducted experiments for approximately 150 unique proteins with 12 independent readings/protein. The data arrays represent feature pixel intensities wavelength (532 nm) based on mean and standard deviation analysis reflecting the relative abundance of all proteins. The PI (Jaberi) analyzed the high throughput tumor proteomics data to identify EGFR as the most over-expressed surface-associated target in the tumor at-the-time-of-metastasis. The network plot shows the associations found using model selection by cross-validation for control cancer data against experimental data. Cohen's d analysis was used for the cross-validation procedure. Instead of testing the relationships for each pair of proteins that requires numerous hypothesis testings such as Bonferroni correction multiple comparisons methods, we employed Markov random fields defined here: Given n=12 independent

and identically distributed samples (readings) {X^((1)),⋯,X^((n))}, where X^((i)) is a p-dimensional vector of the expression changes (p=150) of proteins in the sample; we reconstruct the underlying network G defined by the set of proteins V corresponding to p random variables, and weighted edges E representing the conditional dependencies between the expression changes of proteins (as shown in figure 4.2. by associated linkages). This network is known as Markov random field and represents nonzero joint dependencies between expression changes of all protein pairs given changes of others. Markov networks follow pairwise Markov property: if there is no edge between random variables A,B∈V, they are conditionally independent, i.e., X_A⊥X_B |X_(\A,B) associated with melanoma tumor using the Markov network in figure 4.5.

NP and PMC zeta potential measurements were taken on Malvern Zetasizer Nano ZS (Worcestershire, UK). 98% CoZnO, 0.1%, 10%, and 50% NiZnO, and CaCO3 ± β-Gal were diluted in 1 ml of spectral grade H20 and placed into a disposable folded capillary cell DS1070 (Westborough, MA). Zeta potential measurements were taken in triplicate with 5 sample runs per each measurement. Sample values were average and standard deviation applied for the analysis of surface charge alteration.

Results and Discussion

Physiometacomposites (PMC)

Anticipating the utility of these compositions for chemotherapy and the delivery of antimicrobial peptide and RNA nanoparticles, here we explored the synthesis and characterization of the physiological metamaterials, physiometacomposites (PMCs) containing zinc (Zn), cobalt (Co) and nickel (Ni). PMCs included magnesium (Mg), manganese (Mn) and iron (Fe), also known for their physiological role in enzyme, protein and RNA interaction and stability. PMC derivatives

contained the physiological metals as binary, ternary, quaternary or higher-order oxides or sulfides at either 0.1, 1, 3, 5, 10 or 50% substitution (Fig. 4.1).

B) PMC series

PMC Compositions	Binary	Ternary	Quaternary	Hi Order
[O] or [S]		x	[O]	[O]
Magnesium	control	x	n.t.	n.t.
Manganese	n.t.	x	n.t.	n.t.
Iron	control	x	x	x
Zinc	control	x	x	x
Cobalt	control	x	x	x
Nickel	x	x	nt	nt

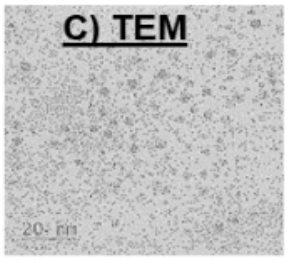

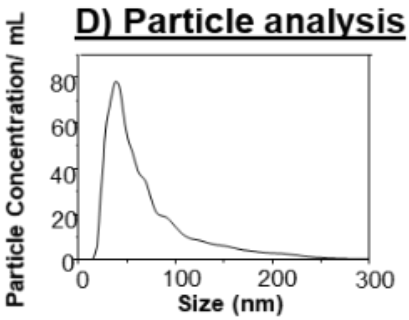

Figure 4.1. A) Hierarchy degree of order (binary, ternary, quaternary and hi-order), B) Representative electron microscope image of hi-order PMC, C) Nanoparticle tracking analysis of the hi-order PMC.

PMC compositions are shown in figure 4.3. whereby the physiological metal oxide or sulfide series was explored as binary, ternary (3 elements), quaternary (4 elements) or 5 or more elements (hi-order) containing manganese, magnesium, iron, zinc, cobalt and/or nickel at 0.1, 1, 3, 5, 10 or 50% mass:mass ratios. In the hi-order case, the raw material was taken from the rocky mountain cobalt belt, compositional analysis suggested the presence of cobalt, iron and the other bio-metals in trace amounts.

Characterization

PMC biomolecular interactions were next characterized by ninhydrin chemical staining, low UV spectral shift and zeta potential analysis [211,214,215].

(C) Zeta potential surface charge shift

PMC	Naked	+ protein/peptide
Ni/ZnO	- 19.54 +/- 0.42	-10.87 (β-Gal)
Ni/ZnO	-21.17 +/- 0.81	-6.298 +/- 1.76 (LL-37)
FeZnS	-13.46 +/- 2.1	-9.42 ± 0.46 (Luc)
Co/ZnO	-17.13 +/- 0.86	-15.86 ± 0.9595 (RBD)
Co/ZnO	-18.35	-8.32 +/ 2.56 (LL-37)
CoFe/ZnO	-12.53 +/- 0.17	-14.02 ± 0.8182 (RBD)
MnZnS	-9.692 +/- 0.0678	-4.693 +/- 1.24 (LL-37)

(F) Electrophoretic gel mobility shift

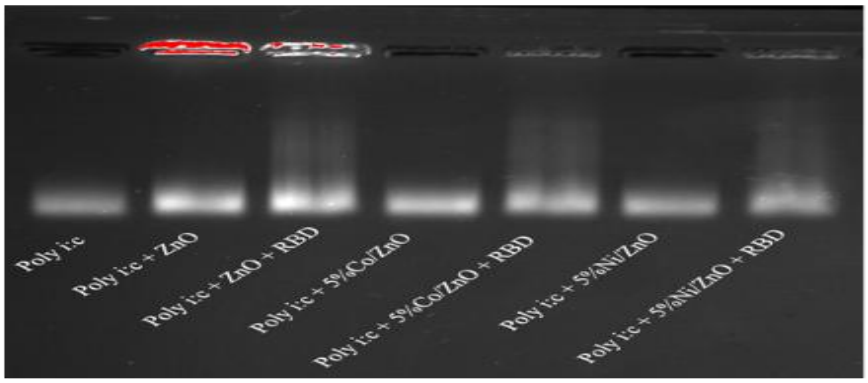

Figure 4.2. A) Zeta potential surface charge shift of PMC nanomaterials in the presence of protein, signifying protein-NP conjugation. B) Gel shift assay with Poly I:C + ZnO, 5%Co/ZnO, 5%Ni/ZnO and RBD complexes.

Zeta potential shift in the PMC surface charge was also consistent with protein interaction, depending on whether the protein was cationic or anionic caused the concomitant expected shift. For example, the antimicrobial LL-37 peptide sequence is H - Leu - Leu - Gly - Asp - Phe - Phe - Arg - Lys - Ser - Lys - Glu - Lys - Ile - Gly - Lys - Glu - Phe - Lys - Arg - Ile - Val - Gln - Arg - Ile - Lys - Asp - Phe - Leu - Arg - Asn - Leu - Val - Pro - Arg - Thr - Glu - Ser - OH

(LLGDFFRKSKEKIGKEFKRIVQRIKDFLRNLVPRTES), having 5 Arg, 7 Lys, 1 Asn, and 1 Gln residues for conjugation to the Co surface with an overall cationic charge calculated as +5.9. Interestingly the cationic shift is less significant for RBD protein, particularly for the

quaternary Co/Fe/ZnO material. Gel shift assay confirmed the interaction whereby a super-shift occurs when the RBD binds to the PMC-poly I:C, dramatically changing the charge:mass ratio as expected resulting in the substantial migrational change through the gel.

Biochemical inhibition

PMC biochemical inhibition of enzyme activity for β-Gal and *Luc* fluorescence and bioluminescence assays is shown (Fig. 4.3).

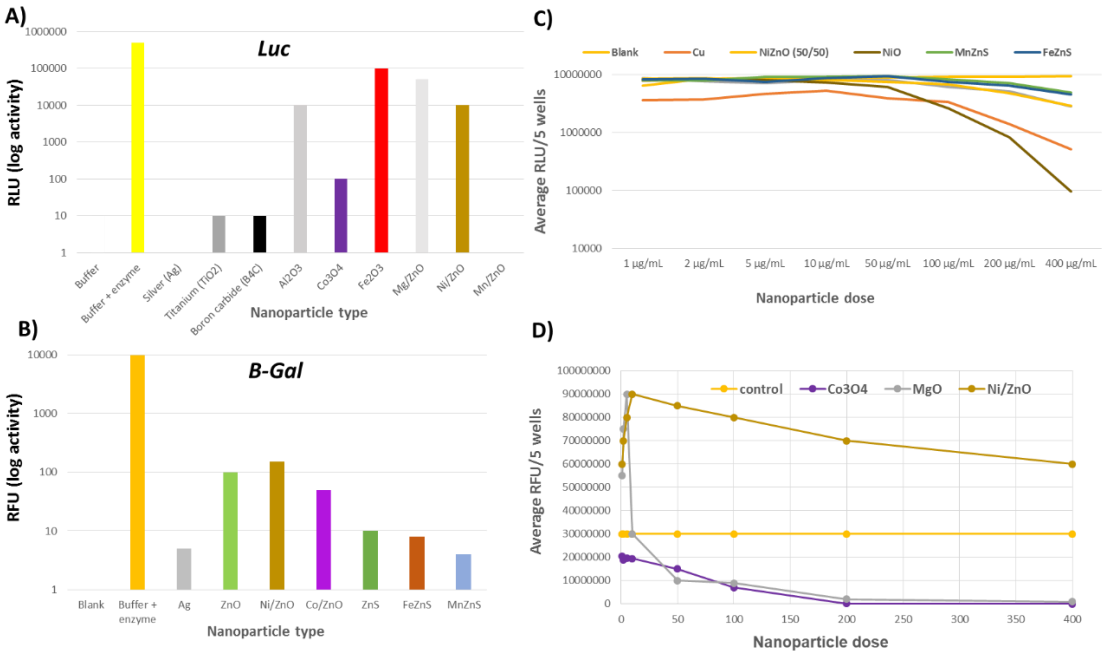

Figure 4.3. Biochemical inhibition of Luc enzyme with bioluminescent readings at 578 nm (A) and β-Gal enzyme with fluorescence readings ex/em 570/590 (B) and the dose-response of NP or PMC against Luc (C) or β-Gal (D). [Data generated in collaboration with Ryan Swanson and Julie Majka]

As shown in figure 4.3., PMCs were tested against both beta-galactosidase (β-Gal) and Luciferase (*Luc*) enzymes, and the production of their fluorescence (1a) or bioluminescence (1b) measured as a function of nanoparticle type and dose. Inhibition was apparent at dosages between 10 to 20 µg/ml, where silver (Ag), boron carbide (B_4C), and titanium dioxide (TiO_2) NP were used as controls [19]. Although all NPs and PMCs tested were at least partially inhibitory at higher doses,

the Mn/ZnO and MnZnS effect was dramatic for Luc and b-Gal respectively, the Co and Ni-based composites [203] consistently gave dose-dependent inhibition for both enzymes, interestingly low dose MgO or Ni/ZnO activated β-Gal. None-the-less these data strongly implicated PMC biochemical activity.

In vivo metastatic tumor analysis

ERK and AKT activation is a hallmark of drug-resistant and metastatic melanoma and has been linked to abrogated RAS regulation [216], specifically to altered RBD interactions [167] and splicing [166]. Proteomics analysis of the B16F10-BALB/C metastatic tumor confirmed association to multiple enzymes in this pathway and was drugged by PMC delivery of RBD protein or RBD-directed splice shifting oligomer (SSO) (Fig. 4.4.).

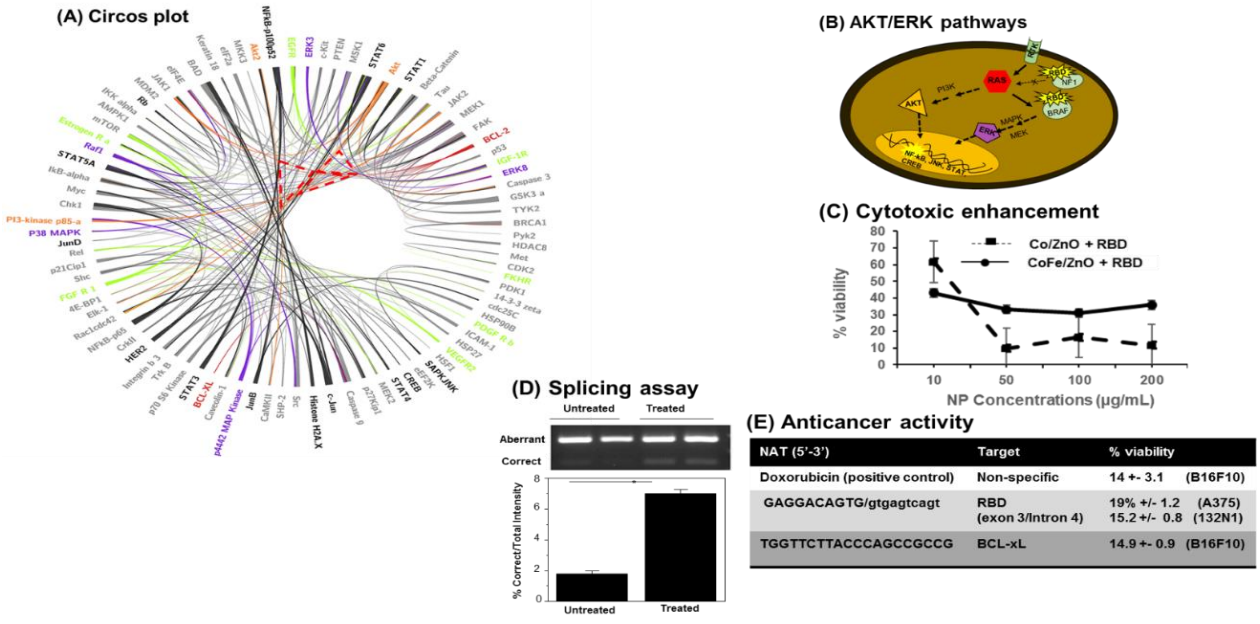

NAT (5'-3')	Target	% viability
Doxorubicin (positive control)	Non-specific	14 +- 3.1 (B16F10)
GAGGACAGTG/gtgagtcagt	RBD (exon 3/intron 4)	19% +/- 1.2 (A375) 15.2 +/- 0.8 (132N1)
TGGTTCTTACCCAGCCGCCG	BCL-xL	14.9 +- 0.9 (B16F10)

Figure 4.4. A) Circos plot proteomics analysis of metastatic B16F10-BALB/c tumor [Data generated in collaboration with Dr. Majid Jaberi], B) RAS/ERK/AKT pathway and enzyme associations, C) B16F10 cellular viability in the presence of Co/ZnO + RBD and CoFe/ZnO + RBD with increasing concentration of NP eliciting stable cell death throughout biological dosages (50-200 µg/ml), D) Splicing correction induced by SSO targeting exon 3/intron 4 junction associated with melanoma drug resistance, E) Anticancer activity of the anti-RBD

SSO compared to BCL-xL ASO or doxorubicin chemotherapy drug [Data generated in collaboration with Miranda Hurst].

Figure 4.4. shows proteomics pattern by Circos plot connecting multiple associations to the RAS/ERK/AKT pathway [Fig. 4.4.(A)] known to be abrogated by altered BRAF/NF-1 RBD interactions and alternative splicing [166,167,216]. Consistent with this PMC-RBD decoy delivery inhibited B16F10 growth by as much as 90-95%, and the anti-RBD SSO chemotherapeutic activity comparable to doxorubicin or the anti-BCL-xL antisense oligomer (ASO) [213], correcting splicing in the exon3/intron 4 associated with drug resistance with activity in A375, B16F10 and 132N1 a model human astrocytoma/glioblastoma brain cancer cell line.

In brief, here PMC space was explored identifying and characterizing compositions with Zn, Co, Ni and Mn with enhanced biomolecular interaction, biochemical inhibition, biological and anticancer activity. Antimicrobial peptide (LL-37) has been tested clinically against metastatic melanoma (https://clinicaltrials.gov/ct2/show/NCT02225366). The chemotherapeutic activity of another antimicrobial peptide, NZX, derived from fungal-bacterial challenge has also recently been tested as a nanoparticle [217]. Taken together these data suggest that a mechanism by which the microbiome may impact the metastatic tumor is to cause the expression of antimicrobial peptide and RNA in this environment and the regulation of key enzymes and cell behavior such as morphology and invasion. The onus will now be on isolating these new microbially-based anticancer biomacromolecules and to studying their interactions and delivery by PMC.

Author Contributions

Conducted experiments: Ryan Swanson, Julie Majka, Majid Jaberi, Nina Marchell, Miranda Hurst, Elza Mathew

Wrote or contributed to the writing of the manuscript: Ryan Swanson, Elza Mathew, Robert DeLong

Chapter 5 - Interaction of Ras Binding Domain (RBD) with Chemotherapeutic Zinc Oxide Nanoparticles: Progress towards RAS Pathway Protein Interference

[Reprint of an article resubmitted to PLOS One Elza N. Mathew, Miranda N. Hurst, Baolin Wang, Vaibhav Murthy, Yuntao Zhang, and Robert K. DeLong]

Abstract

Zinc oxide (ZnO) NP considered a nanoscale chemotherapeutic. Thus, the drug delivery of this inorganic NP is of considerable importance. Ras mutations are common in cancer and the activation of this signaling pathway is a hallmark in carcinoma, melanoma, and many other aggressive malignancies. Thus, here we examined the binding and delivery of Ras binding domain (RBD), a model cancer-relevant protein and effector of Ras by ZnO NP. Shifts in zeta potential in water, PBS, DMEM and DMEM supplemented with FBS supported NP interaction to RBD. Fluorescence quenching of the NP was concentration-dependent for RBD, Stern–Volmer analysis of this data used to estimate binding strength which was significant for ZnO-RBD ($K_d < 10^{-5}$). ZnO NP interaction to RBD was further confirmed by pull-down assay followed by elution and SDS-PAGE analysis. The ability of ZnO NP to inhibit 3-D tumor spheroid was compared, the ZnO NP breaking apart these structures revealing a significant (>50%) zone of killing as shown by light and fluorescence microscopy after intra-vital staining. ZnO 100 nm was superior to ZnO 14 nm in terms of anticancer activity when bound to RBD. These data indicate the potential diagnostic application or therapeutic activity of RBD-NP complexes *in vivo* which demands further investigation.

Introduction

Ras is a protein along the cellular pathway between mitogen-activated protein kinases and extracellular signal activated kinases (MAPK-ERK pathway) which has thus far eluded traditional drug discovery. There are three different human Ras genes – KRas, NRas and HRas, the mutation predominance of which varies with the cancer type [218]. Given the importance of Ras signaling pathways in many cancers, an elegant approach to target this therefore would be intracellular delivery of Ras binding domain (RBD). Enrichment of metal oxide nanoparticles via surface functionalization of tissue-specific biological or chemical agents makes it easier to navigate to the exact locus [219]. While RBD lacks the kinase domain of B-Raf, abolishing its ability to upregulate this pathway, the 149 amino acid portion of BRAF, is responsible for binding to RAS and thought to act as a decoy. However RBD does not contain any hydrophobic sequence or membrane penetration sequence, thus requiring an NP such as ZnO NP for increased delivery to cancer cells. Therefore it seemed plausible to interact RBD with zinc oxide (ZnO) NP and this novel approach might otherwise improve the drug delivery and anticancer activity [86].

Physiologically-based zinc oxide (ZnO) is a highly sought after nanoparticle owing to its unique intrinsic and indigenous anticancer activity and has been shown to be selectively toxic to a variety of cancer cell types including cancerous T cells, human hepatocellular carcinoma (HepG2), human bronchial epithelial cells (BEAS-2B) and human lung adenocarcinoma (A549) cells [13,14]. ZnO NP generates reactive oxygen species (ROS) which can also trigger cancer cells to undergo apoptosis [21]. Intraperitoneal administration of ZnO has been associated with an increase in superoxide dismutase activity and total antioxidant status in male rats [22]. Its unique surface chemistry allows the formation of ZnOH+ species which likely underlies its interaction with the anionic membrane of cancer cells and its drug delivery activity [19,20]. Recent work from our

research group suggests ZnO NP inhibition of experimental melanoma [17] can be improved by its interaction to poly I:C RNA (Ramani, et al., 2017).

In this study, we comparatively characterized ZnO NP—14 nm and 100 nm—association to RBD and their potential for RBD delivery and the anticancer activity associated therewith.

Materials & Methods

Materials and Equipment

ZnO NPs (size < 100nm) were purchased from Sigma –Aldrich (St. Louis, MO). Raf-1 RBD, GST (recombinant protein expressed in *E. coli*: purity > 50%) was purchased from EMD Millipore Corporation (California, USA). Dynamic light scattering and zeta potential measurements were performed using Malvern Zetasizer Nano ZSP (Worcestershire, UK). Fluorescence spectroscopy was conducted using SpectraMax® i3x multimode microplate reader (Molecular Devices, California, USA). For SDS-PAGE**,** RunBlue™ precast gels were purchased from Expedeon Ltd. (Cambridge, UK), and GelCode™ Blue safe protein stain was purchased from ThermoFisher Scientific (Waltham, MA, USA). Gel imaging was conducted using Gel Doc™ XR+ gel documentation system (BIO-RAD, California, USA).

B16-F10 mouse melanoma cells and Dulbecco's Modified Eagle's Medium (DMEM) with high glucose and L-glutamine for cell culture were purchased from ATCC® (Virginia, USA). Phosphate buffered saline (PBS) was purchased from Corning® (Pennsylvania, USA). FITC Annexin V Apoptosis Detection Kit I was purchased from BD Biosciences (Maryland, USA).

NP stock preparation

Nanoparticles (~1 mg) were washed two times in 70% isopropanol followed by two times in 100% isopropanol. Washed nanoparticles were air-dried overnight. The dry pellets were dispersed in 1 mL of HPLC grade water to make 1mg/mL stock solutions.

Zeta potential measurement

Samples were prepared by adding 20µL of nanoparticle stock solution (1mg/mL) in the 980µL of different dispersants namely 1) HPLC grade water, 2) DMEM with fetal bovine serum (FBS), 3) DMEM without FBS, and 4) PBS. Afterwards, the samples were analyzed at a volume of 1 mL in a capillary cell cuvette (Malvern) on a Malvern Zetasizer Nano Range Dynamic Light Scattering instrument.

Fluorescence spectroscopy

Samples were prepared at a final volume of 200 µL, and transferred to a black 96 well microplate (MIDSCI, St.Louis, MO). Fluorescence spectra were taken at an excitation wavelength of 350 nm using the SpectraMax® i3x multimode microplate reader with steps of 2 nm and a read height of 1 mm. The binding constant was evaluated by analyzing the fluorescence quenching with the Stern-Volmer equation (Ramani, et al., 2017; Stern & Volmer, 1919).

SDS – PAGE

RBD-NP samples were prepared by combining 2µg of RBD (1 µL of 2µg/µL stock solution) and 5µg of ZnO NP or ZnO/Fe_3O_4 NP (5µL of 1mg/mL stock solution). The RBD-NP samples were incubated at room temperature for 15 minutes with gentle shaking. Following incubation, the samples were subjected to sodium dodecyl sulfate polyacrylamide gel electrophoresis (SDS-PAGE) at 100V for 2 h hours and 30 minutes. BEPAR Bullseye pre-stained protein ladder (10-180 kDa) was used as the reference.

[*Loading sample composition:* Sample loading buffer- 5µL; Sample (NP and BSA - 5µL each) - 10 µL; HPLC grade water - 5 µL; Total - 20 µL

Running buffer composition: RunBlue™ 20X buffer - 50 mL; Deionized water - 950 mL; Total - 1L]

The protein bands were visualized using GelCode™ Blue Safe Protein Stain. The gel was imaged using Gel Doc™ XR+ gel documentation system and analyzed with Image Lab™ software.

Determination of hydrodynamic size of ZnO NP in cell culture medium over time

The size of ZnO NPs in cell culture medium was determined using dynamic light scattering analysis. In brief, 20µg/ml solutions of ZnO NP (14 nm and 100 nm) were incubated at 37^0 C with shaking for 72 h. Size measurements were taken at 0h, 1h, 2h, 4h, 8h, 12h, 24h, 48h, and 72h in duplicates on a Malvern Zetasizer Nano Range Dynamic Light Scattering instrument.

Determination of dissolution of ZnO NPs in cell culture medium

The concentration of ZnO NPs in the cell culture medium was determined using ICP-MS analysis [221]. In brief, 20µg/ml solutions of ZnO NP (14 nm and 100 nm) were incubated at 37^0 C with shaking for 72 h. Size measurements were taken at 0h, 1h, 2h, 4h, 8h, 12h, 24h, 48h, and 72h in duplicates on a Malvern Zetasizer Nano Range Dynamic Light Scattering instrument. Following size measurement, the samples were centrifuged at 14,000 rpm for 1 minute. 100 µl of the supernatant containing ZnO NP was digested using 1 ml of 70% nitric acid (HNO3). The digestion was performed in a hot water bath at 60^0 C for 45 minutes. Following digestion, all the digests were diluted by the addition of 9 ml deionized water. Zinc ion concentration was measured on a PerkinElmer NexION® 350D ICP-MS using Syngistix™ software (Shelton, CT, USA).

Spheroid Assay

HeLa cells were plated at $5.0x10^3$ cells per well in inSpheroGravityTRAP ULA plates (*PerkinElmer, Cat# ISP-09-001*) following the manufacturer's protocol. Spheroids were allowed to form for 2 days, the NP treatment was applied (10 to 20 ug/ml) and the cells were imaged by light microscopy or after staining with Invitrogen live/dead green/red fluorescent staining kit by fluorescence microscopy.

MTT assay

B16F10 cells were plated on a 96-well plate at 5,000 cells/ well and were allowed to establish overnight. The next day, they were treated with either 1, 5, 10, 20, 50, or 100 µg/mL of the given NP. After 24 hours with the above treatments, cells were rinsed with PBS, and MTT reagent was added for 5 hours. After incubation with the MTT, DMSO was used to dissolve the formazan crystals and the plate was read for absorption at 562 nm using a Synergy H1 Hybrid Multi-Mode Reader (BioTek, VT) to calculate cell viability data.

For testing the effect of RBD bound NPs, 20 µg/mL of ZnO NP-100 nm was used with a final concentration of 25µg/mL RBD bound. An additional group of RBD alone was tested, also at a final concentration of 25 µg/mL.

Untreated cell culture medium served as the blank. Untreated cells have been used as the control. The experiment was done in quadruplicate wells.

Apoptosis assay

B16F10 cells were plated on 8 – well chamber plates at 3×10^4 cells per well and allowed to establish overnight. Cells were treated with washed nanoparticles at a concentration of 0.05 mg/mL. Cells were stained using FITC Annexin V Apoptosis Detection Kit I and imaged at 0 and

12 hours using an Olympus CKX41 Inverted Microscope with Olympus SC100 camera and Analysis getIT imaging Software. As the positive control, 50µM H_2O_2 was used.

Results and Discussion

Confirming interaction of RBD to ZnO NPs

Many proteins contain charged amino acids which can facilitate interaction to the surface of nanoparticles. Such ionic interactions and the close association of the protein to the surface of the nanoparticle causes a change in its surface charge and this can be measured by zeta potential analysis. As shown in table 4, zeta potential measurements revealed a shift in the surface charge of ZnO NPs following incubation with RBD, suggesting interaction to protein. The zeta potential here is reported as the average of the multiple peaks as the sample was polydispersed [44].

Table 5.1. Zeta potential measurements of ZnO NP in response to RBD binding

Solvent	**ZnO NP Alone**	**ZnO NP + RBD**
HPLC Grade Water	-17.86±0.3628	-17.86±0.5307
PBS	-23.22±0.6807	--11.14±0.3709
DMEM	-13.3±0.7797	-10.86±0.34
DMEM + FBS	-6.91±0.1881	-8.152±0.4776

Zeta potential and size variations both in the presence and absence of RBD was also compared with two differently sized ZnO NPs – 14 nm and 100 nm as shown in table 5.1. and figure 5.1. respectively.

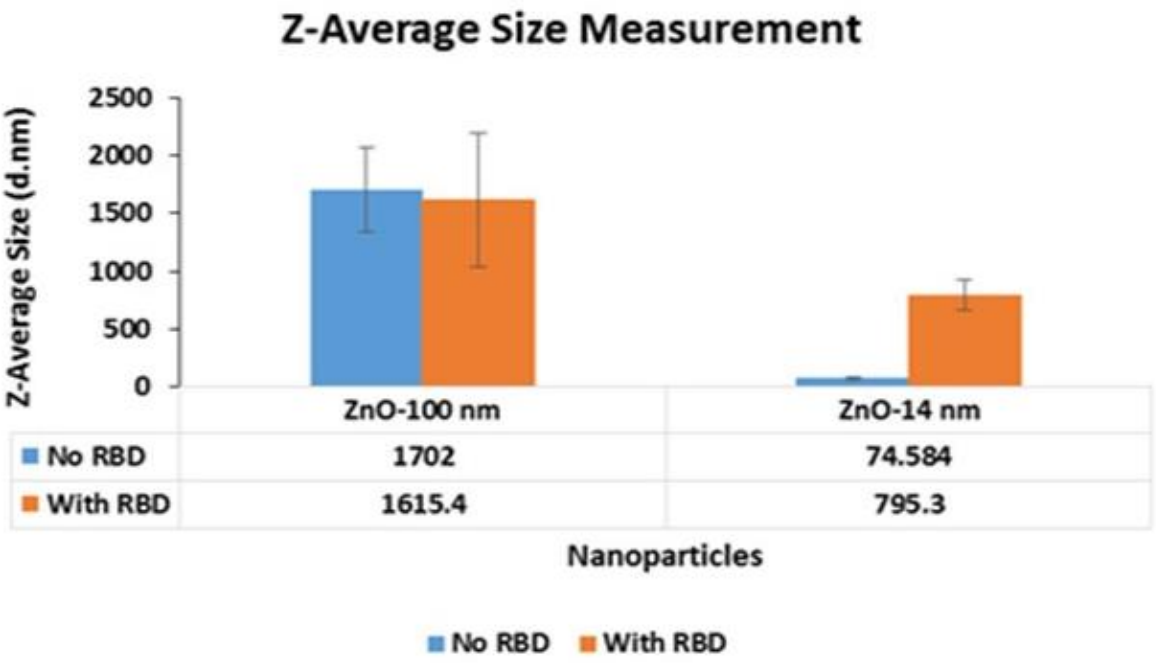

Figure 5.1. Size measurements of ZnO NP-100 nm and 14 nm

The charge of RBD was estimated to be 7.3 at pH 7.0 using the online protein sequence analysis tool Protein Calculator v3.4 (Scripps Research, California, USA). Considering this fact, a positive shift was expected in the zeta potential of nanoparticles bound with RBD. With ZnO NP, such a positive shift was observed when dispersed in DMEM and PBS.

The determination of fluorescence quenching by spectroscopy is a traditional and convenient method to assess protein interaction with nanoparticle [222]. The fluorescence spectra [Fig. 5.2. (A)] suggests a strong association of RBD to ZnO. It also shows a dose dependency, with higher doses of ZnO NP showing higher fluorescence values, which is suppressed upon binding to RBD.

The suppression of the fluorescence with RBD present at equimolar concentrations of NP suggests interaction. Using this data it is possible to apply Stern-Volmer equation to calculate the disassociation constant and a number of binding sites as we have previous described for ZnO NP

but here applied to study RBD binding [17]. These data are shown below. Accordingly, the association of RBD with ZnO NPs appeared to be strong.

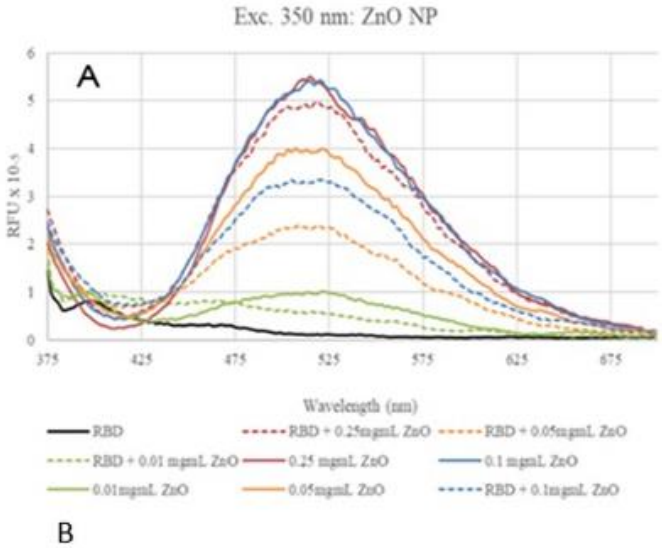

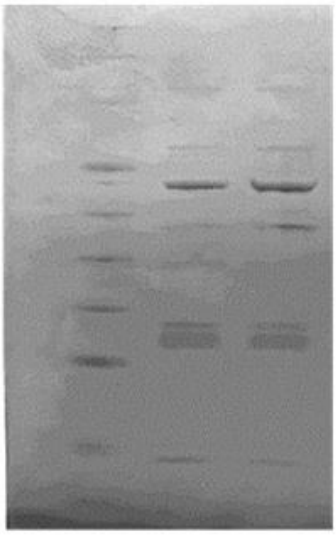

B

Nanoparticle	K_{sv} (1/mM)	n	K_d (mol/L)
Zinc oxide	13.087	1.3696, ~1	1.2306×10^{-5}

Figure 5.2. A. Fluorescence quenching of ZnO NP in the presence and absence of RBD measured at 350 nm further confirming interaction. B. Dissociation constant of RBD complexed to Zinc oxide nanoparticle C. SDS-PAGE analysis of RBD and ZnO nanoparticle combination Lane 1 – Protein Ladder; 2 – RBD alone; 3 – RBD and ZnO NP combination

Protein gel electrophoresis analysis

Protein gel electrophoresis is a standard method for studying protein interaction with NP**.** For example, an earlier study demonstrated the presence of transferrin and/or human serum albumin on the surface of polystyrene nanoparticles were effectively analyzed using SDS-PAGE [222]. SDS-PAGE was also used to compare the amount of proteins adsorbed on gold nanoparticles [223]. To further examine the interaction between RBD and the ZnO NP, the complexes were subjected to protein gel electrophoresis analysis following incubation at room temperature for 15

minutes. ZnO NP pulled down RBD, elution of the protein from the particle demonstrating a banding pattern almost identical to that of the free protein control.

Physical stability of ZnO NP in biological media

It is important that NPs maintain their size stability when incubated in biological fluids. ZnO NPs (14 nm and 100 nm) were incubated in cell culture medium at 37^0 C and agitated on a shaker for 72 h and the effect on size measurements determined at 0h, 1h, 2h, 4h, 8h, 12h, 24h, 48h and 72h. As figure 5.3. A. shows, ZnO NP (14 nm) showed variation in hydrodynamic size all through the time course following an irregular pattern. However, ZnO NP (100 nm) was found to maintain its hydrodynamic size and was quite stable and consistent with very little variation for the duration of the experiment.

ZnO NP does not dissociate in cell culture medium

Current dogma suggests ZnO NP may disassociate into ions limiting its utility as *in vivo* drug carriers [224]. However, this property is thought to underlie its anticancer activity within the tumor microenvironment and cancer cells [48]. To address this, zinc concentration was monitored in the supernatants of ZnO NPs suspended in serum-containing cell culture medium incubated at 37^0 C using ICP-MS. As evident from figure 5.3. (B), zinc concentration in the cell culture medium supernatant followed a decreasing trend over time. This observation suggests that ZnO NP does not dissociate in normal physiological conditions. The cellular effects we see shall be attributed to ZnO NP itself, rather than zinc ions.

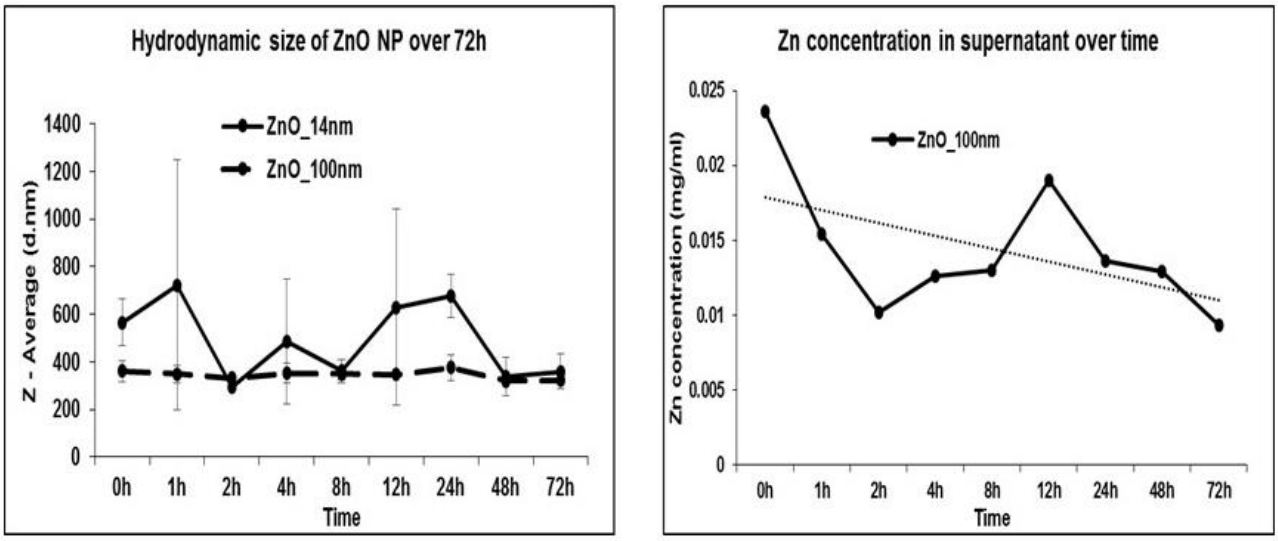

Figure 5.3. A. Hydrodynamic size of ZnO NPs (14 nm and 100 nm) monitored over 72h time course. B. Zinc concentration in supernatant monitored over 72h time course

Zinc oxide nanoparticles inhibit 3-D spheroids

3-D spheroids are important models for drug discovery and tumor delivery [225]. HeLa cell spheroids were cultured and the spheroids allowed to form prior to nanoparticle treatment and were exposed to ZnO NP at 10 or 20 ug/ml concentration respectively in serum-containing media and photographed at time 0, 24 and 5 days by light microscopy as shown in figure 5.4. (A).

As seen in figure 5.4. (A), overt growth inhbition was seen particularly after 5-day exposure. In the case of ZnO NP these structures appeared to break apart and the dense cell growth radiating out from the center of the spheroid was almost completely absent. The degree of disintegration was profound on day 5 the homology of the treated spheroids being quite distinct in comparison to untreated controls.

The spheroids were also stained by intravital stain to assess the relative kill zone from treated versus untreated samples and representative images shown after visualization by fluorescence microscopy seen in figure 5.4. (B).

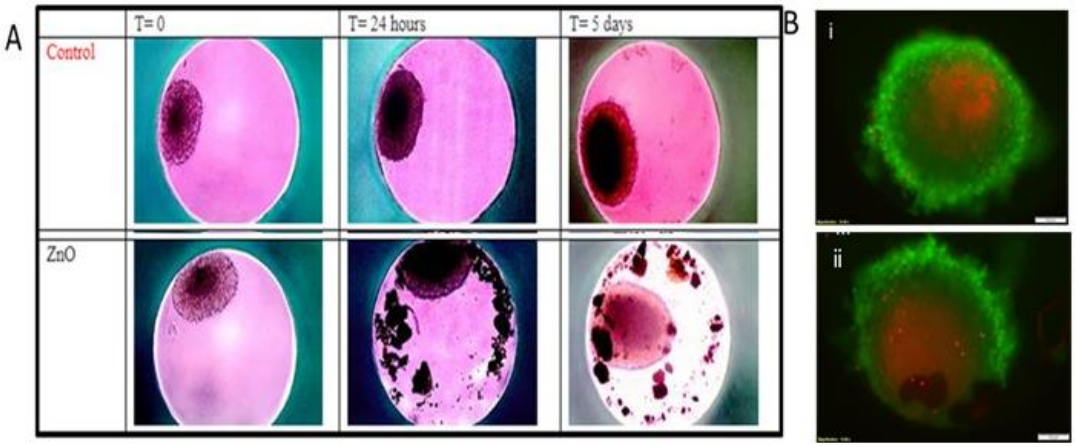

Figure 5.4. Anticancer activity of ZnO NP in HeLa cell spheroids at 0 h, 24 h and day 5 B. i. Untreated spheroids ii. Spheroids treated with ZnO NP

Clearly, the kill zone is significantly increased after exposure to ZnO (5.4. (B). ii.) relative to untreated controls (5.4. (B). i.). These data are consistent with our recent work demonstrating intratumoral injection of ZnO NP in an experimental mouse melanoma model also has significant antitumor activity *in vivo* [69].

Zinc oxide combined with RBD exhibited anticancer activity in mouse melanoma cells

The response of mouse melanoma cells to RBD both in the presence and absence of nanoparticle carriers was measured in terms of cell viability using the colorimetric MTT assay. MTT assay measures the reduction of the water-soluble yellow tetrazolium salt 3-(4,5-Dimethylthiazol-2-yl)-2,5-diphenyltetrazoliumbromide into the insoluble purple formazan compounds by mitochondrial activity [226]. The total mitochondrial activity is directly related to the number of viable cells for most cell populations[227]. Figure 5.5. (B). shows that the anticancer activity of RBD itself in the absence of NP was minimal. However, when the RBD was complexed to ZnO NP to form RBD-ZnO NP was quite potent with > 50% cytotoxic activity at 10 µg/mL

dosage. In our previous work, we have shown that non-malignant cells treated with this concentration are normally 80-90% viable under these conditions. Cell viability could be reduced to 89% at 50 µg/mL RBD-ZnO.

Zinc oxide-RBD complexes induce apoptosis morphology in mouse melanoma cells

Based on the cytotoxic activity, we were interested in visualizing the ZnO NP - induced apoptosis in mouse melanoma cells. B16F10 cells were treated with washed nanoparticles at a concentration of 0.05 mg/mL or 50µM H_2O_2 and imaged using an Olympus CKX41 Inverted Microscope after staining with Annexin-FITC / PI at 0 and 12 h [17,18] [11, 12]. Figure 5.5. (C) shows the cellular effects of ZnO-RBD treatment NPs with panel A showing bright field micrographs and panel B showing fluorescent micrographs. H_2O_2 served as the positive control causing apoptosis with many of the cells staining yellow/orange. Compared to the cells that didn't receive RBD-ZnO, cell density was greatly reduced by H_2O_2 treatment. Some reduction of adherent cells was evident also after RBD-ZnO treatment indicative of cytotoxic activity, however, these cells had a less spindle and more rounded morphology typical of apoptotic cells. These cells also stained yellow/orange consistent with their apoptosis.

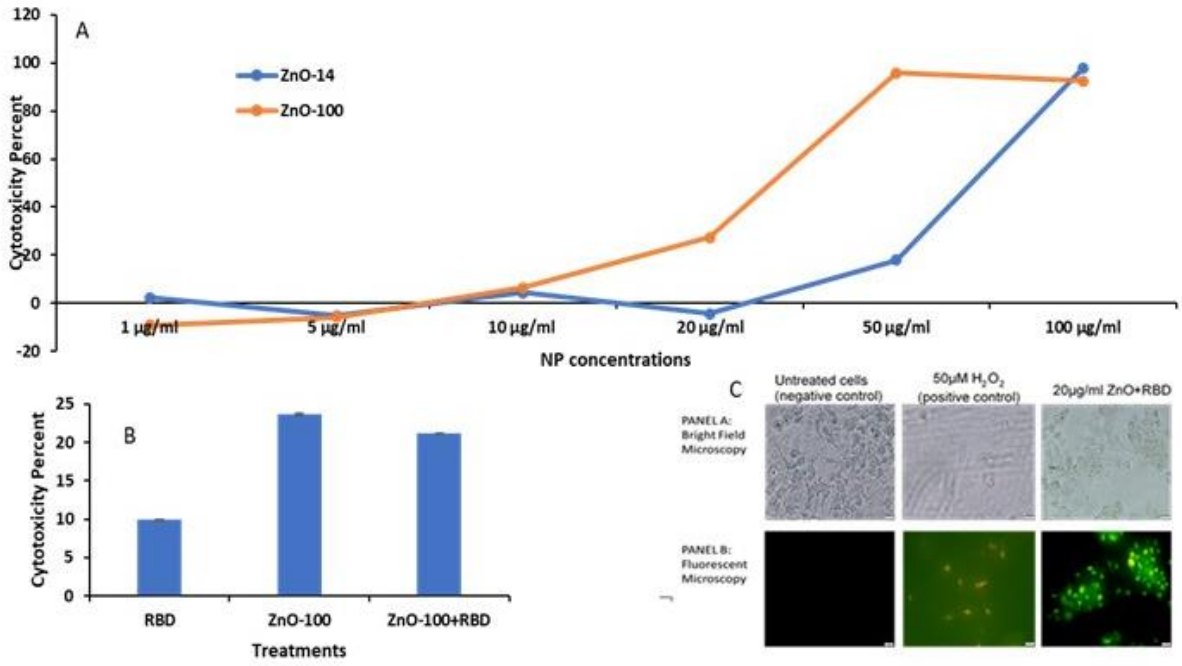

Figure 5.5. A. Comparative dose-dependent cytotoxicity in B16F10 cells in response to increasing doses of ZnO NP 100 nm and ZnO NP – 14 nm B. Comparative cytotoxicity in B16F10 cells in response to RBD-bound ZnO NP 100 nm @ 20 µg/ml C. Bright-field microscopic images (panel A) and fluorescence microscopic images (panel B) of B16F10 cells after 24 h exposure to ZnO + RBD

In brief, the data demonstrate the interaction of RBD to ZnO NP. In this study, zeta potential measurements and elution of the protein followed by gel electrophoresis analysis support the formation of RBD-ZnO complexes. Fluorescent quenching by spectroscopy experiments shows the protein interaction to ZnO NP, which is important for ZnO NP mediated intracellular protein delivery. ZnO NP can inhibit 3-D tumor spheroid phenotype and growth demonstrating a loss of internal cell density and a greater zone of killing red to green ratio than untreated spheroids. ZnO NP particle size is stable in cell culture media and no evidence of substantial ion generation was observed. These data suggest ZnO NP can serve as a protein carrier to deliver RBD into the cells. The fact that RBD itself is non-cytotoxic, but RBD-ZnO gave dose-dependent anticancer

activity strongly supports this. Indeed RBD-ZnO also triggered overt cancer cell apoptosis as evident by the treated cell morphology and also apoptosis specific staining and fluorescence microscopy analysis. The impact of this research is substantial given the importance of the RAS pathway to a variety of difficult to treat cancers, and the lack of a RAS-specific drug. Therefore, nanoparticle delivery of intracellular RBD may serve as *protein interference* as a novel strategy to inhibit the critical RAS pathway and may have potential as an experimental therapeutic approach against melanoma and potentially other RAS-dependent cancers.

Author Contributions

Participated in research design: Mathew, DeLong

Conducted experiments: Hurst, Wang, Murthy, Zhang, Mathew

Wrote or contributed to the writing of the manuscript: Mathew, DeLong

Chapter 6 - Interaction of the antimicrobial peptide LL-37 in with zinc oxide nanoparticle and its physiometacomposites

Introduction

Antimicrobial peptides (AMP) are small molecular weight effector molecules that fight against the foreign microbes, as part of the innate immune system. Their antimicrobial activity has been attributed to their ability to penetrate plasma membrane inducing DNA damage and inhibiting multiple cell signaling cascades [228]. LL-37 is the only cathelicidin-derived AMP found in humans [229]. It is a C- terminal peptide proteolytically derived from the human cathelicidin protein – hCAP18[230–232]. Primarily found in the secondary granules of neutrophils, this peptide is expressed in almost all the tissues including myelocytes, testes, keratinocytes and saliva [233–237]. Upregulation or down regulation of LL-37 has been associated with numerous diseases. In addition to its antimicrobial activity against bacteria, viruses, fungi and parasites, LL-37 also plays an important role in tissue homeostasis and regenerative processes [232,238].

Anticancer Activity of LL-37

Tumor-response of LL-37 has been found to be tissue-specific [232]. LL-37 stimulated cell proliferation and wound closure in airway epithelial cells [238]. In human malignant melanoma cell lines, overexpression of LL-37 was associated with enhanced cell proliferation, cell migration, and invasion of malignant cells [239]. Enhanced cell proliferation was also noticed in breast cancer cell lines [240]. In gastric cancer caused by *Helicobacter pylori*, LL-37 expression was found to be enhanced in the mucosal epithelial cells as a defense mechanism [241]. Serum-independent chemotaxis, induced by LL-37, for neutrophils, monocytes, and T cells was mediated through formyl peptide receptor–like 1 (Fprl1) [242]. Functionalization with aminosilane-modified magnetic nanoparticles enhanced the anticancer activity of LL-37 in colon cancer cells (DLD-1 and HT-29).

In DLD-1 cells, ceragenin, the synthetic analog of LL-37 peptide, was found to induce improved apoptosis [243]. In uveal melanoma cells, LL-37 induced caspase-independent apoptosis associated with a reduction in mitochondrial membrane potential [244]. It has been shown that in skin injury, IFNβ1 is produced by the epidermis in response to LL-37 [245]. FK-16 fragment of the LL-37 peptide which exhibits better anticancer activity has been shown to induce colon cancer cell death due to caspase-independent apoptosis and autophagy [246(p16)].

LL-37 is currently in clinical trials against melanoma where intra-tumoral injections of the molecule are administered weekly for a period of 8 weeks at a starting dose of 250 µg/tumor. This study aims at finding an appropriate dose of the peptide to treat the disease [70]. In preclinical studies, intra-tumoral injections of LL-37 was found to stimulate the innate immune system. This was mediated through the plasmacytoid dendritic cells which causes tumor destruction [247].

Investigating the anticancer effect of LL-37 complexed to ZnO NP

With the available information on tissue-specific LL-37's tumor-response and the intrinsic anticancer activity of ZnO NP, this project proposes to investigate the previously unknown extent as well as deducible mechanisms of anticancer effect of LL-37 against melanoma in combination with ZnO NP. Both zinc oxide and LL-37 have been shown to modulate immune responses. It is worth investigating the nature of their effects – additive, synergistic, or antagonistic – upon combination. The use of oxidative stress-induced changes in cell signaling can be explored as a potential biomarker for melanoma as well. Demonstration of precise mechanisms of action is expected to help with the development of further therapeutic approaches targeting and/or employing the peptide alone or in combination with ZnO NP.

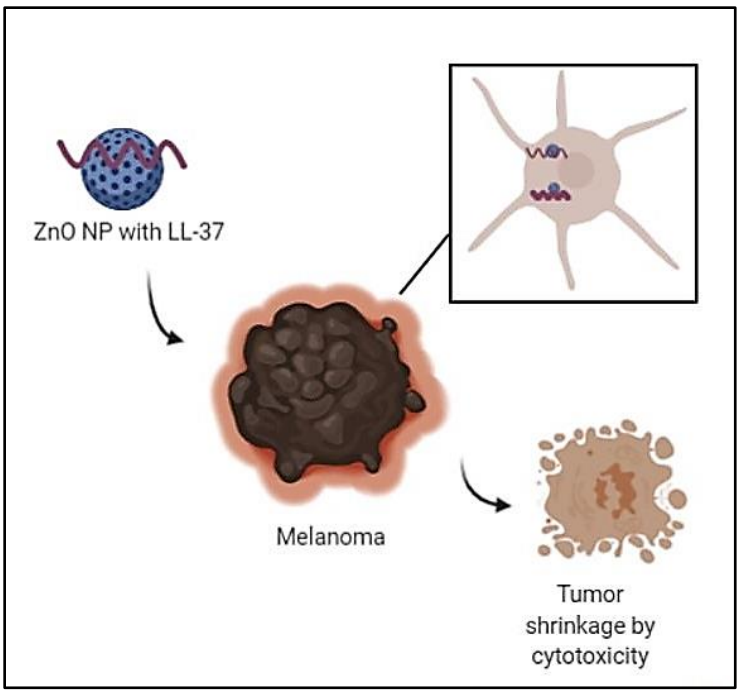

Figure 6.1. Graphical representation of the activity of ZnO in combination with LL-37

The comprehensive goal of the proposed research is to elucidate the mechanism of action of LL-37 in melanoma when administered in combination with ZnO NP. An in-depth investigation of the cellular mechanisms and effects is expected to help in molding new therapeutic targets and approaches. The specific aims towards this goal are:

1. To characterize the physicochemical properties of LL-37 complexed to ZnO NP
2. To characterize the biological effects of the complex *in vitro*

Materials & Methods

Physicochemical Characterization

ZnO NPs (size < 100nm) was purchased from Sigma –Aldrich (St. Louis, MO). LL-37 protein was provided by Dr. Cheng Kao, Indian University). The purity of the peptide was analyzed by High Resolution-Mass Spectrometry (HR-MS) at the Analytical Chemistry Core Laboratory, at ICCM/NICKS, Kansas State University. Dynamic light scattering and zeta potential

measurements were performed using Malvern Zetasizer Nano ZSP (Worcestershire, UK). For SDS-PAGE, RunBlue™ precast gels were purchased from Expedeon Ltd. (Cambridge, UK) and GelCode™ Blue safe protein stain, from ThermoFisher Scientific (Waltham, MA, USA). Gel imaging was conducted using Gel Doc™ XR+ gel documentation system (BIO-RAD, California, USA).

High Resolution-Mass Spectrometry

Peptide preparation 1.7 mg of LL37 (MW=4,493.28 g/mole) was dissolved in 0.5 mL of LC-MS grade water to make a solution at 757 µM.

High-resolution mass spectrometry (HR-MS) A QExactive (Thermo Fisher, Waltham mA) was used for the analysis of the peptide. The peptide solution was infused directly into the Heated Electrospray Ionization (HESI) source in positive mode, using a syringe at a flow rate of 20 µL/minute (see table 6.1. for HESI source parameters). A scan ranging from m/z 450 to 1250 was acquired at a resolution of 140,000 was recorded.

Table 6.1. HESI source parameters used for High resolution mass spectrometry of LL-37 peptide

Sheath gas flow rate	70 psi
Auxilliary gas flow rate	30 psi
Sweep gas flow rate	1 psi
Spray voltage	3.75 kV
Capillary temperature	300 °C
Auxiliary gas heater temperature	200 °C

Optimizing the loading technique/conditions and payload by BCA Assay

The binding parameters were investigated by the bicinchinonic acid (BCA) assay. To acquire a standard curve of LL-37 peptide, BCA assay was used and the absorption spectra were measured at 480 nm using Spectramax™ multiplate reader. For this, serial dilutions of a stock solution of 2 mg/ml of LL-37 peptide were prepared in HPLC grade water to a final volume of 100 µl. Following this, to quantify the payload of the peptide on the ZnO NP, 10 µl of a 10 mg/ml stock solution of ZnO NP was added to the serially diluted peptide solutions. The mixture was shaken vigorously, at 150 rpm for 30 min, followed by centrifugation at 14,000 rpm for 15 minutes at room temperature. The absorbance of both the pellet and the supernatant was measured at 480 nm. The absorption spectra of the supernatant were used to calculate the concentration of unbound LL-37 in the supernatant. Bovine serum albumin (BSA) was used as a standard for the assay.

Using the absorbance values and concentrations of the bound and unbound peptide, the payload was estimated. To identify the ideal proportion of LL-37 peptide and ZnO NP with maximum payload, different combinations of centrifugation and incubation times at room temperature and 37°C were examined.

Dynamic light scattering

Using the Malvern Zetasizer Nano Range Dynamic Light Scattering, the interaction between LL-37 and ZnO NP will be quantified in terms of change in zeta potential using established protocol [168]. Change in these properties will be monitored over a time course of 72 h, at both room temperature and 37°C.

SDS-PAGE

LL-37-NP samples were prepared by combining 2µg of LL-37 (1 µL of 2µg/µL stock solution) and 5µg of ZnO NP (5µL of 1mg/mL stock solution). The LL-37-NP samples were

incubated at room temperature for 15 minutes with gentle shaking. Following incubation, the samples were subjected to sodium dodecyl sulfate polyacrylamide gel electrophoresis (SDS-PAGE) at 100V for 2 h hours and 30 minutes. BEPAR Bullseye pre-stained protein ladder (10-180 kDa) was used as the reference.

Biological Characterization *in vitro*

MTT assay

B16F10 cells were plated on a 96-well plate at 5,000 cells per well and were allowed to establish overnight. The next day, they were treated with either 1, 5, 10, 20, 50, or 100 µg/mL of the given NP. After 24 hours with the above treatments, cells were rinsed with PBS, and MTT reagent was added for 5 hours. After incubation with the MTT, DMSO was used to dissolve the formazan crystals and the plate was read for absorption at 562 nm using a Synergy H1 Hybrid Multi-Mode Reader (BioTek, VT) to calculate cell viability data.

Investigating the changes in gene expression

Real-time Reverse Transcription PCR (RT-qPCR) was used to evaluate the changes in gene expression of cancer-relevant genes including ERK and AKT. The relative fold change in gene expression will be estimated using the $2^{-\Delta\Delta Ct}$ method [248].

B16F10 were seeded in six well plates at 0.25×10^6 cells per well. After 24h of seeding, the cells were treated with ZnO and 0.1%Ni/ZnO at 20µg/ml in duplicate wells. Two wells were left untreated to serve as a control. At 48h of NP exposure, RNA was isolated from the cells using Ribozol™ reagent. The quality and concentration of RNA isolated were estimated using Nanodrop® spectrophotometer. RT-qPCR for ERK and AKT was performed using Applied Biosystems® real-time PCR system at the core molecular biology facility, CVM, KSU. 18S rRNA was used as the endogenous control. SYBR Green One-Step qPCR kit was used.

Reaction Mix Composition: SYBR Green Master Mix: 13.5 µl

Forward Primer: 0.5 µl

Reverse Primer: 0.5 µl

Template RNA: 100 ng

Nuclease Free water: Added to make upto 25 µl per reaction

Table 6.2. Primers used for RT-qPCR

Gene	Forward Primer	Reverse Primer
AKT	5'-AAG CAC CGT GTG ACC ATG AA-3'	5'-CCG TCC TTG ATG CCT TCC TT-3'
ERK	5'-GAC CTA CTG CCA GAG AAC CC-3'	5'-GTC CAG TCC TCT GAG CCC TT-3'

Results and Discussion

Physicochemical Characterization

Relative abundance of LL-37 peptide:

The LL-37 peptide fraction received from Indian University was analyzed using High-Resolution Mass Spectrometry. The most abundant form observed are the peptide protonated as [M+4H]4+, [M+5H]5+ and [M+6H]6+ as shown in figure 6.2.

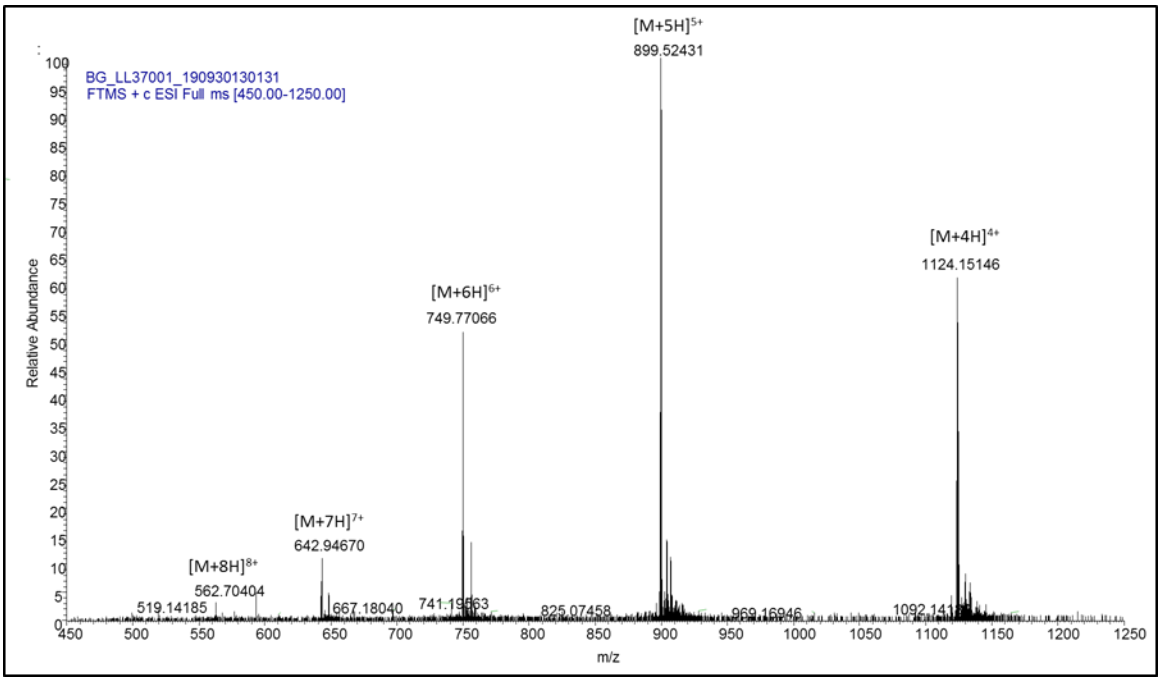

Figure 6.2. Relative abundance of LL-37 peptide in the fraction received from Indiana University demonstrated by High-Resolution Mass Spectrometry [Data generated in collaboration with Dr. Geraldine Magnin]

Zeta potential measurements

Zeta potential measurements have long been used to characterize the interaction of biomolecules with nanoparticles [18]. The charge of LL-37 peptide is estimated to be 5.9 [249]. In the presence of LL-37 peptide, the zeta potentials of ZnO and its PMC NPs showed a positive deflection suggestive of effective surface interaction. Among the different PMCs, 0.1% Ni/ZnO showed the highest interaction as evident from figure 6.3.

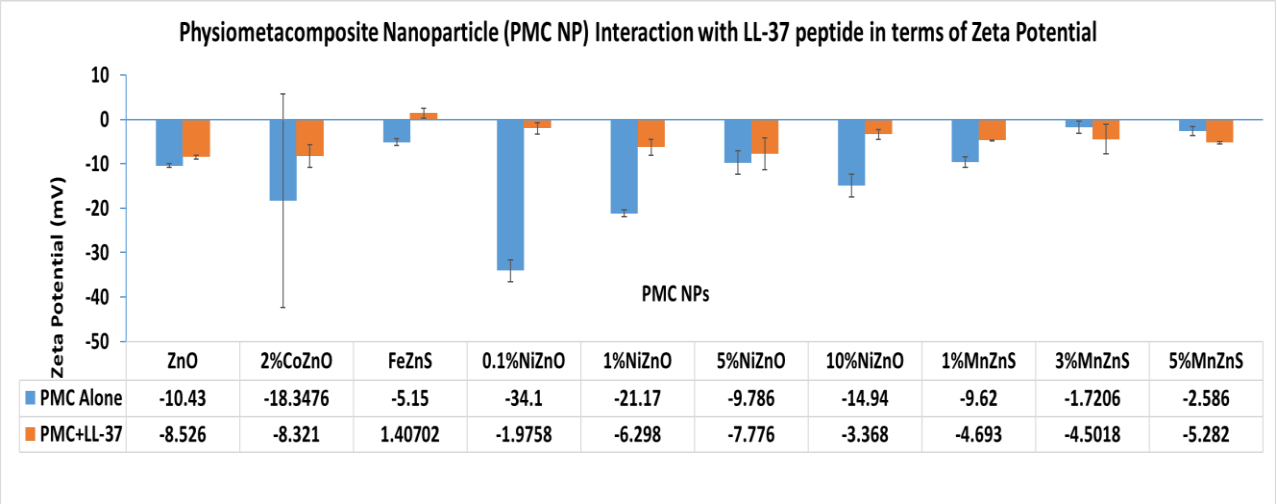

Figure 6.3. Zeta potential measurements showing the interaction of physiometacomposite nanoparticles with LL-37 peptide

Payload estimation

Payload of LL-37 on NP surface was estimated using BCA assay. The BCA assay depends on the reduction of cupric (Cu^{2+}) to cuprous (Cu^{+}) ions as in the Biuret reaction [250,251]. A standard curve was plotted using different concentrations of LL-37. Absorbance (A_{480}) of ZnO NP and 0.1% Ni/ZnO PMC NP combined with LL-37 pellet was found to increase with the concentration of LL-37. No absorbance was found in the supernatant, suggesting effective binding of the peptide on the NP surface.

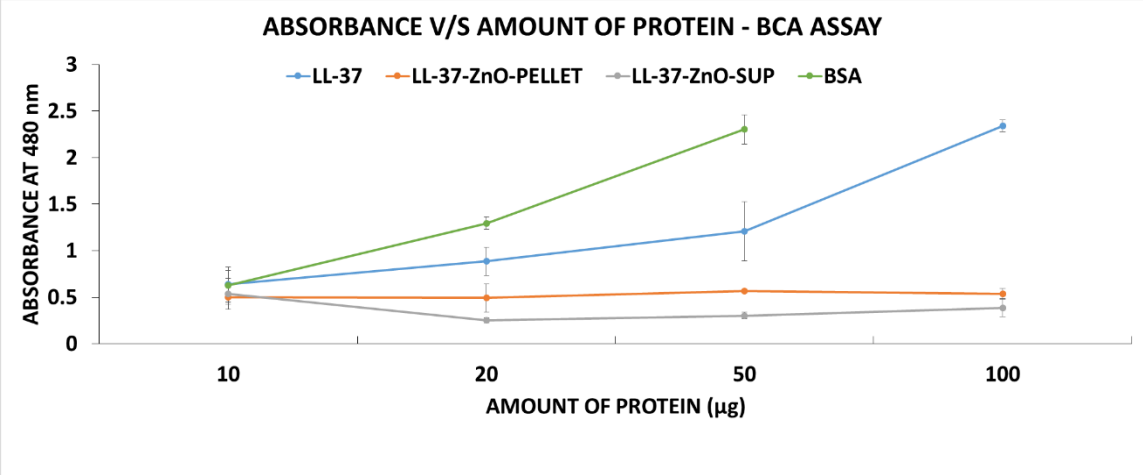

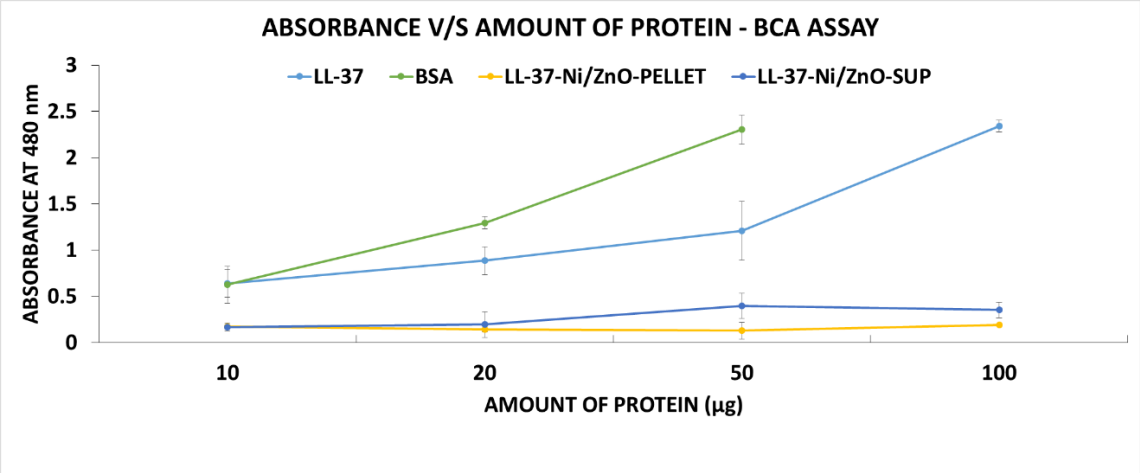

Figure 6.4. Absorbance measurements suggesting binding of LL-37 on the surface of ZnO NP and Ni/ZnO PMC NP

Considering the concentration of bound and unbound LL-37 based on the absorbance measurements, the payload of the peptide on the surface of the nanoparticles was estimated as shown in table 6.3.

Table 6.3. Estimation of payload of LL-37 peptide on ZnO NP and 0.1% Ni/ZnO PMC NP

Amount of LL-37 protein alone (µg)	Amount of protein bound to ZnO NP (µg/µg)	Amount of protein bound to Ni/ZnO NP (µg/µg)
10	0.088480663	0.095230203
20	0.193752302	0.194737569

50	0.492790055	0.49106814
100	0.991247698	0.991841621

SDS-PAGE analysis

SDS-PAGE analysis of LL-37 combined with ZnO NP further demonstrated the interaction between the two. As clearly seen in figure 6.5., the band corresponding to ZnO NP + LL-37was found to be much thinner than the peptide alone.

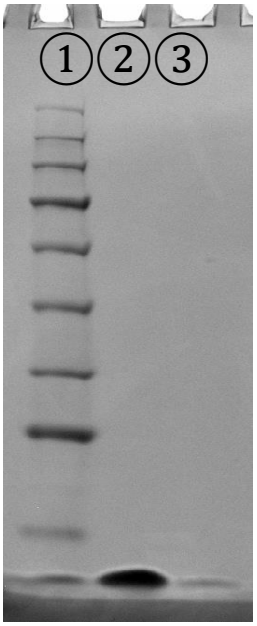

Figure 6.5. SDS-PAGE suggesting interaction of LL-37 with ZnO NP. Lane 1-Protein ladder; 2-LL-37 alone; 3-ZnO NP + LL-37

Cytotoxicity in mouse melanoma cells

Antimelanoma activity of ZnO and its PMC NPs was assessed in B16F10 mouse melanoma cells using MTT assay. It was found to highly dependent on the concentration of the NP used as well as the duration of exposure (Tables 6.4. & 6.5.). For instance, ZnO NP had the highest antimelanoma activity at 48h both in the presence and absence of LL-37 at 20µg/ml and in the presence of LL-37 at 50µg/ml. At 96h, ZnO NP had the best antimelanoma activity in the presence

of LL-37. Biocompatibility of PMCs were also assessed in NIH3T3 mouse fibroblast cells (See supplemental information).

Table 6.4. Time (h) at which various nanoparticles demonstrate the highest anti-melanoma activity

Nanoparticle	Time (h) with the Highest Anti-Melanoma Activity			
	(@20µg/ml)		(@50µg/ml)	
	Intrinsic	NP + LL-37	Intrinsic	NP + LL-37
ZnO	48	48	96	48
0.1%NiZnO	96	48	72	48
1%NiZnO	96	24	96	48
5%NiZnO	48	72	72	96
10%NiZnO	96	24	72	24
1%MnZnS	48	24	96	24
3%MnZnS	96	48	72	48
5%MnZnS	96	48	72	24

Table 6.5. Nanoparticles showing the highest anti-melanoma activity at 24, 48, 72 and 96h

Time (h)	NP with the highest anti-melanoma activity	
	(@20µg/ml)	(@50µg/ml)

	Intrinsic	NP + LL-37	Intrinsic	NP + LL-37
24	0.1%NiZnO	1%MnZnS	5% MnZnS	5% MnZnS
48	1%MnZnS	0.1%NiZnO	ZnO	1%NiZnO
72	3%MnZnS	3%MnZnS	ZnO	1%NiZnO
96	1%NiZnO	ZnO	ZnO	1%NiZnO

Gene expression of ERK and AKT suppressed by ZnO NP and 0.1%Ni/ZnO PMC

RT-qPCR was used to assess the ERK and AKT gene expression in mouse melanoma cells. B16F10 mouse melanoma cells exhibited increased expression of AKT and ERK which was estimated to be ~6 fold and ~7 fold respectively (Fig. 6.6.). ERK expression was found to be depressed in B16F10 cells when treated with ZnO and 0.1%Ni/ZnO for 48 h (Fig. 6.7.). ZnO treatment reduced ERK expression to ~46% and 0.1%Ni/ZnO to ~63% of untreated melanoma cells (Fig. 6.8.).

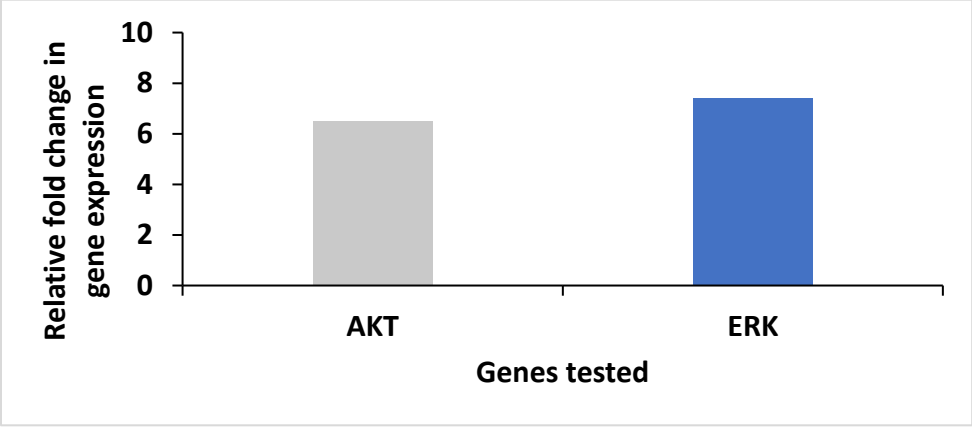

Figure 6.6. Comparative expression of AKT and ERK in mouse melanoma cells and fibroblast cells

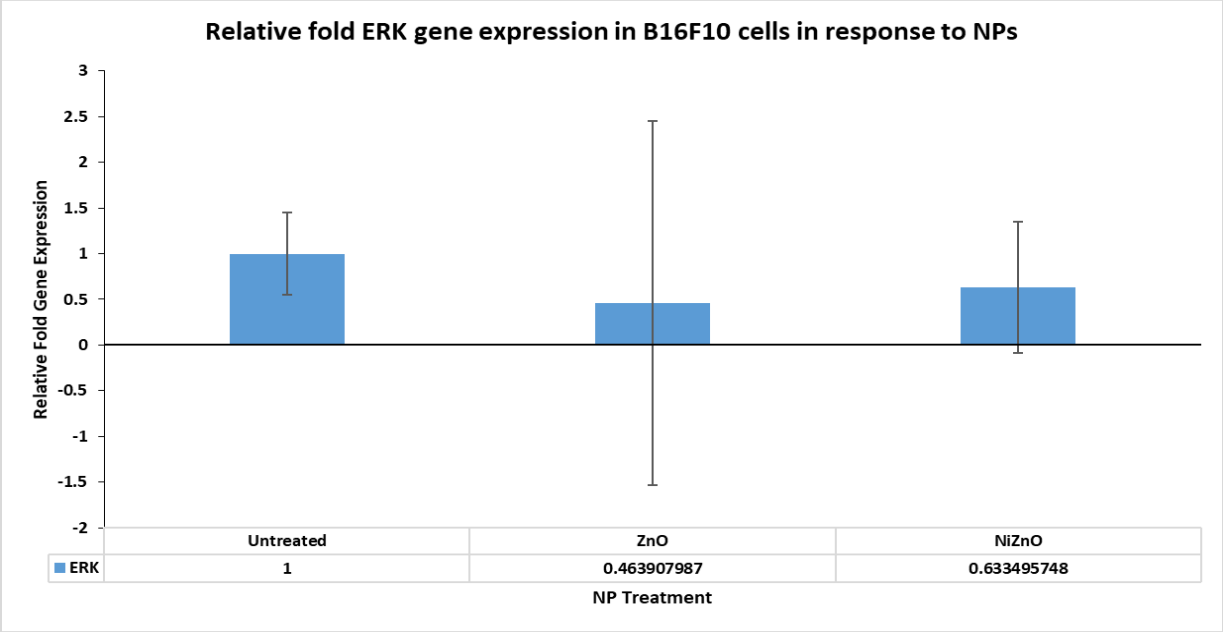

Figure 6.7. Relative fold expression of ERK gene in B16F10 cells in response to ZnO and Ni/ZnO NPs

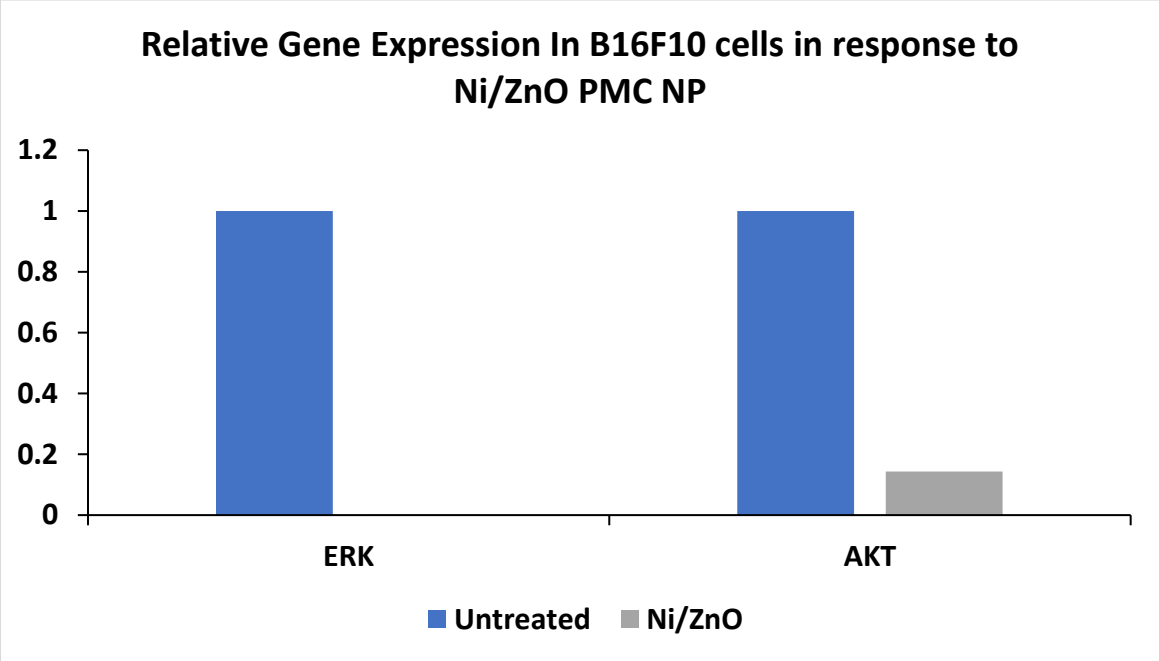

Figure 6.8. Relative fold expression of ERK gene in B16F10 cells in response to Ni/ZnO PMC NP

Conclusion

In this study, zeta potential measurements, the BCA assay, and the elution of the protein followed by gel electrophoresis analysis support formation of the complex between LL-37 peptide and ZnO NP and/or its PMCs. The antimelanoma activity of the complexes was found to be dependent on the NP concentration as well as the duration of exposure. Interaction of ZnO NP and its PMCs with LL-37, an antimicrobial peptide with dual anticancer activity suggests a potential interaction of these NPs with the tumor microbiome. Considering the antimelanoma activity *in vitro*, the ideal NP-LL-37 combination might be able to bring about tumor suppression through the interplay with the tumor microbiome, which demands further investigation *in vivo*.

Author Contributions

Participated in research design: Mathew, DeLong

Conducted experiments: Mathew

Wrote or contributed to the writing of the chapter: Mathew, DeLong

Chapter 7 - Summary

Cancer continues to be the second leading cause of death worldwide, despite the advent of novel therapies along with the conventional treatment options – surgery, chemotherapy and radiation. Malignant melanoma is the most lethal form of skin cancer with the lowest five-year survival rate of 24.8%. Nanomedicine is an emerging candidate for cancer therapy the persistent search for better treatment options. Zinc oxide nanoparticle (ZnO NP) is a chemical with its specific anticancer activity demonstrated in different cancer cell lines. This dissertation was an endeavor to elucidate the biophysical, biochemical, and biological mechanism of anti-cancer activity of ZnO NP and its physiometacomposite (PMC) nanoparticles.

Immediate biodistribution of ZnO NP was found in a BALB/c nude mouse model with no associated pathological changes. ZnO NP has a superior immunogenic activity which varies with the biomolecule —RNA or protein—bound to it. PMCs inhibited luciferase and β-galactosidase enzyme activity as evidenced by reduced bioluminescence and fluorescence. Proteomics analysis of the B16F10-BALB/C metastatic tumor confirmed association to multiple enzymes in RAS/ERK/AKT pathway. Biophysical and Biological characterization suggest the interaction of RBD and LL-37 peptides with ZnO NP resulting in enhanced anticancer activity in B16F10 mouse melanoma cells. This *protein interference* approach may have potential as an experimental therapeutic approach against melanoma and potentially other RAS-dependent cancers. Enhanced gene expression of ERK and AKT was demonstrated in B16F10 mouse melanoma cells, which was found to be suppressed when treated with ZnO NP or Ni/ZnO PMC NP.

Future Perspectives:

Considering canines as the best comparative oncology model for human melanoma, the anticancer activity of ZnO NP and its PMCs need to be assessed in canine melanoma cells and

animal models. The biodistribution of ZnO NP was found in multiple organs—liver, kidneys, lungs, brain, and heart. This suggests the potential of using ZnO NP for developing therapeutic modalities against diseases/pathogenic agents affecting internal organs, particularly, NSARS-COV-2 which affects the internal lining of the respiratory tract with its detection in multiple sites and specimens not limited to feces, blood and urine [252]. However, *via* the screening of the different PMCs of ZnO NP in murine and canine melanoma cells, a better candidate may be chosen for the *in vivo* studies. In addition to quantifying the anticancer activity of different NPs, tumor microenvironment studies may be initiated to unveil the probable mechanisms behind their anticancer activity. The antimelanoma activity of RBD and/or LL-37 in combination with the NPs is recommended to be investigated *in vivo.* Appraising the size of RBD (42 kDa), RBD binding aptamer or RAS antisense oligomer may considered for their potential antimelanoma activity *in vivo* pending *in vitro* examination. Regarding LL-37, its independent anticancer segment — FK-16 — may also be considered a potential candidate for further evaluation of antimelanoma activity *in vitro* and *in vivo*. Being an antimicrobial peptide, the interaction of LL-37 with nanoparticles may be further analyzed with respect to the role of tumor microbiome in tumorigenesis. Based on the fluorescence properties of the NPs, further evaluation is needed to assess their potential as imaging agents.

References

1. WHO. Cancer. Published 2018. Accessed October 17, 2019. https://www.who.int/news-room/fact-sheets/detail/cancer

2. Tran S, DeGiovanni P-J, Piel B, Rai P. Cancer nanomedicine: a review of recent success in drug delivery. *Clin Transl Med*. 2017;6. doi:10.1186/s40169-017-0175-0

3. Wicki A, Witzigmann D, Balasubramanian V, Huwyler J. Nanomedicine in cancer therapy: Challenges, opportunities, and clinical applications. *J Controlled Release*. 2015;200:138-157. doi:10.1016/j.jconrel.2014.12.030

4. Shi J, Kantoff PW, Wooster R, Farokhzad OC. Cancer nanomedicine: progress, challenges and opportunities. *Nat Rev Cancer*. 2017;17(1):20-37. doi:10.1038/nrc.2016.108

5. Mout R, Moyano DF, Rana S, Rotello VM. Surface functionalization of nanoparticles for nanomedicine. *Chem Soc Rev*. 2012;41(7):2539-2544. doi:10.1039/c2cs15294k

6. Kalyane D, Raval N, Maheshwari R, Tambe V, Kalia K, Tekade RK. Employment of enhanced permeability and retention effect (EPR): Nanoparticle-based precision tools for targeting of therapeutic and diagnostic agent in cancer. *Mater Sci Eng C*. 2019;98:1252-1276. doi:10.1016/j.msec.2019.01.066

7. Greish K. Enhanced Permeability and Retention (EPR) Effect for Anticancer Nanomedicine Drug Targeting. In: Grobmyer SR, Moudgil BM, eds. *Cancer Nanotechnology: Methods and Protocols*. Methods in Molecular Biology. Humana Press; 2010:25-37. doi:10.1007/978-1-60761-609-2_3

8. Andreini C, Banci L, Bertini I, Rosato A. Counting the Zinc-Proteins Encoded in the Human Genome. *J Proteome Res*. 2006;5(1):196-201. doi:10.1021/pr050361j

9. Kluska K, Adamczyk J, Krężel A. Metal binding properties, stability and reactivity of zinc fingers. *Coord Chem Rev*. 2018;367:18-64. doi:10.1016/j.ccr.2018.04.009

10. Maret W. Zinc in Cellular Regulation: The Nature and Significance of "Zinc Signals." *Int J Mol Sci*. 2017;18(11). doi:10.3390/ijms18112285

11. CFR - Code of Federal Regulations Title 21. Accessed October 24, 2019. https://www.accessdata.fda.gov/scripts/cdrh/cfdocs/cfcfr/CFRSearch.cfm?fr=182.8991

12. Jiang J, Pi J, Cai J. The Advancing of Zinc Oxide Nanoparticles for Biomedical Applications. *Bioinorg Chem Appl*. 2018;2018. doi:10.1155/2018/1062562

13. Akhtar MJ, Ahamed M, Kumar S, Khan MM, Ahmad J, Alrokayan SA. Zinc oxide nanoparticles selectively induce apoptosis in human cancer cells through reactive oxygen species. *Int J Nanomedicine*. 2012;7:845-858. doi:10.2147/IJN.S29129

14. Hanley C, Layne J, Punnoose A, et al. Preferential killing of cancer cells and activated human T cells using ZnO nanoparticles. *Nanotechnology*. 2008;19(29):295103. doi:10.1088/0957-4484/19/29/295103

15. Ramani M. Zinc Oxide Nanoparticle-Poly I:C RNA Complexes: Implication as Therapeutics against Experimental Melanoma. *Mol Pharm*. 2017;14(3):614-626. doi:10.1021/acs.molpharmaceut.6b00795

16. Gehrke T, Scherzad A, Ickrath P, et al. Zinc oxide nanoparticles antagonize the effect of Cetuximab on head and neck squamous cell carcinoma in vitro. *Cancer Biol Ther*. 2017;18(7):513-518. doi:10.1080/15384047.2017.1323598

17. DeLong RK, Mitchell JA, Morris RT, et al. Enzyme and Cancer Cell Selectivity of Nanoparticles: Inhibition of 3D Metastatic Phenotype and Experimental Melanoma by Zinc Oxide. *J Biomed Nanotechnol*. 2017;13(2):221-232.

18. Ramani M, Nguyen TDT, Aryal S, Ghosh KC, DeLong RK. Elucidating the RNA Nano–Bio Interface: Mechanisms of Anticancer Poly I:C RNA and Zinc Oxide Nanoparticle Interaction. *J Phys Chem C*. 2017;121(29):15702-15711. doi:10.1021/acs.jpcc.7b02954

19. Thomas SE, Comer J, Kim MJ, et al. Comparative functional dynamics studies on the enzyme nano-bio interface. *Int J Nanomedicine*. 2018;13:4523-4537. doi:10.2147/IJN.S152222

20. Zhang Y, Nayak TR, Hong H, Cai W. Biomedical applications of zinc oxide nanomaterials. *Curr Mol Med*. 2013;13(10):1633.

21. Ryter SW, Kim HP, Hoetzel A, et al. Mechanisms of Cell Death in Oxidative Stress. *Antioxid Redox Signal*. 2007;9(1):49-90. doi:10.1089/ars.2007.9.49

22. Zarei S, Moradi H, Asadi S, Aabbasalipourkabir R, Ziamajidi N. Study of the effect of zinc oxide on enzymatic antioxidant activity in male rats. *Pajouhan Sci J*. 2017;15(3):29-36. doi:10.21859/psj-15035

23. Patel P, Kansara K, Senapati VA, Shanker R, Dhawan A, Kumar A. Cell cycle dependent cellular uptake of zinc oxide nanoparticles in human epidermal cells. *Mutagenesis*. 2016;31(4):481-490. doi:10.1093/mutage/gew014

24. Bai D-P, Zhang X-F, Zhang G-L, Huang Y-F, Gurunathan S. Zinc oxide nanoparticles induce apoptosis and autophagy in human ovarian cancer cells. *Int J Nanomedicine*. 2017;12:6521-6535. doi:10.2147/IJN.S140071

25. Pandurangan M, Veerappan M, Kim D. Cytotoxicity of Zinc Oxide Nanoparticles on Antioxidant Enzyme Activities and mRNA Expression in the Cocultured C2C12 and 3T3-L1 Cells. *Appl Biochem Biotechnol*. 2015;175(3):1270-1281. doi:10.1007/s12010-014-1351-y

26. Sharma V, Anderson D, Dhawan A. Zinc oxide nanoparticles induce oxidative DNA damage and ROS-triggered mitochondria mediated apoptosis in human liver cells (HepG2). *Apoptosis Int J Program Cell Death*. 2012;17(8):852-870. doi:10.1007/s10495-012-0705-6

27. De Angelis I, Barone F, Zijno A, et al. Comparative study of ZnO and TiO_2 nanoparticles: physicochemical characterisation and toxicological effects on human colon carcinoma cells. *Nanotoxicology*. 2013;7(8):1361-1372. doi:10.3109/17435390.2012.741724

28. Cao Y, Roursgaard M, Kermanizadeh A, Loft S, Møller P. Synergistic effects of zinc oxide nanoparticles and Fatty acids on toxicity to caco-2 cells. *Int J Toxicol*. 2015;34(1):67-76. doi:10.1177/1091581814560032

29. Fang X, Jiang L, Gong Y, Li J, Liu L, Cao Y. The presence of oleate stabilized ZnO nanoparticles (NPs) and reduced the toxicity of aged NPs to Caco-2 and HepG2 cells. *Chem Biol Interact*. 2017;278:40-47. doi:10.1016/j.cbi.2017.10.002

30. Sanaeimehr Z, Javadi I, Namvar F. Antiangiogenic and antiapoptotic effects of green-synthesized zinc oxide nanoparticles using Sargassum muticum algae extraction. *Cancer Nanotechnol*. 2018;9(1):3. doi:10.1186/s12645-018-0037-5

31. Jin S-E, Jin H-E. Synthesis, Characterization, and Three-Dimensional Structure Generation of Zinc Oxide-Based Nanomedicine for Biomedical Applications. *Pharmaceutics*. 2019;11(11):575. doi:10.3390/pharmaceutics11110575

32. Saptarshi SR, Feltis BN, Wright PF, Lopata AL. Investigating the immunomodulatory nature of zinc oxide nanoparticles at sub-cytotoxic levels in vitro and after intranasal instillation in vivo. *J Nanobiotechnology*. 2015;13. doi:10.1186/s12951-015-0067-7

33. De M, You C-C, Srivastava S, Rotello VM. Biomimetic Interactions of Proteins with Functionalized Nanoparticles: A Thermodynamic Study. *J Am Chem Soc*. 2007;129(35):10747-10753. doi:10.1021/ja071642q

34. Saptarshi SR, Duschl A, Lopata AL. Interaction of nanoparticles with proteins: relation to bio-reactivity of the nanoparticle. *J Nanobiotechnology*. 2013;11(1):26. doi:10.1186/1477-3155-11-26

35. Yu J, Kim H-J, Go M-R, Bae S-H, Choi S-J. ZnO Interactions with Biomatrices: Effect of Particle Size on ZnO-Protein Corona. *Nanomaterials*. 2017;7(11). doi:10.3390/nano7110377

36. Bhunia AK, Samanta PK, Saha S, Kamilya T. ZnO nanoparticle-protein interaction: Corona formation with associated unfolding. *Appl Phys Lett*. 2013;103(14):143701. doi:10.1063/1.4824021

37. Da Silva E, Kembouche Y, Tegner U, Baun A, Jensen KA. Interaction of biologically relevant proteins with ZnO nanomaterials: A confounding factor for in vitro toxicity endpoints. *Toxicol In Vitro*. 2019;56:41-51. doi:10.1016/j.tiv.2018.12.016

38. Bardhan M, Mandal G, Ganguly T. Steady state, time resolved, and circular dichroism spectroscopic studies to reveal the nature of interactions of zinc oxide nanoparticles with transport protein bovine serum albumin and to monitor the possible protein conformational changes. *J Appl Phys*. 2009;106(3):034701. doi:10.1063/1.3190483

39. Kathiravan A, Paramaguru G, Renganathan R. Study on the binding of colloidal zinc oxide nanoparticles with bovine serum albumin. *J Mol Struct*. 2009;934(1):129-137. doi:10.1016/j.molstruc.2009.06.032

40. Marucco A, Fenoglio I, Turci F, Fubini B. Interaction of fibrinogen and albumin with titanium dioxide nanoparticles of different crystalline phases. *J Phys Conf Ser*. 2013;429:012014. doi:10.1088/1742-6596/429/1/012014

41. Schwaminger SP, Blank-Shim SA, Scheifele I, Pipich V, Fraga-García P, Berensmeier S. Design of Interactions Between Nanomaterials and Proteins: A Highly Affine Peptide Tag to Bare Iron Oxide Nanoparticles for Magnetic Protein Separation. *Biotechnol J*. 2019;14(3):1800055. doi:10.1002/biot.201800055

42. Piella J, Bastús NG, Puntes V. Size-Dependent Protein–Nanoparticle Interactions in Citrate-Stabilized Gold Nanoparticles: The Emergence of the Protein Corona. *Bioconjug Chem*. 2017;28(1):88-97. doi:10.1021/acs.bioconjchem.6b00575

43. Calzolai L, Franchini F, Gilliland D, Rossi F. Protein−Nanoparticle Interaction: Identification of the Ubiquitin−Gold Nanoparticle Interaction Site. *Nano Lett*. 2010;10(8):3101-3105. doi:10.1021/nl101746v

44. Clogston JD, Patri AK. Zeta potential measurement. *Methods Mol Biol Clifton NJ*. 2011;697:63-71. doi:10.1007/978-1-60327-198-1_6

45. Asadabad MA, Eskandari MJ. Transmission Electron Microscopy as Best Technique for Characterization in Nanotechnology. *Synth React Inorg Met-Org Nano-Met Chem*. 2015;45(3):323-326. doi:10.1080/15533174.2013.831901

46. Rimkus G, Bremer-Streck S, Grüttner C, Kaiser WA, Hilger I. Can we accurately quantify nanoparticle associated proteins when constructing high-affinity MRI molecular imaging probes? *Contrast Media Mol Imaging*. 2011;6(3):119-125. doi:10.1002/cmmi.405

47. Fornaguera C, Solans C. Methods for the In Vitro Characterization of Nanomedicines—Biological Component Interaction. *J Pers Med*. 2017;7(1). doi:10.3390/jpm7010002

48. DeLong R, Cheng Y-H, Pearson P, et al. Translating nanomedicine to comparative oncology: the case for combining zinc oxide nanomaterials with nucleic acid therapeutic and protein delivery for treating metastatic cancer. *J Pharmacol Exp Ther*. Published online 1904 2019. doi:10.1124/jpet.118.256230

49. Melanoma of the Skin - Cancer Stat Facts. SEER. Published 2020. Accessed August 23, 2020. https://seer.cancer.gov/statfacts/html/melan.html

50. Tyrrell H, Payne M. Combatting mucosal melanoma: recent advances and future perspectives. *Melanoma Manag*. 2018;5(3). doi:10.2217/mmt-2018-0003

51. Yang J, Manson DK, Marr BP, Carvajal RD. Treatment of uveal melanoma: where are we now? *Ther Adv Med Oncol*. 2018;10. doi:10.1177/1758834018757175

52. Balch CM, Houghton AN, Sober AJ, Soong S. Cutaneous Melanoma, 4th Edition. *Dermatol Surg*. 2005;31(12):1715-1715. doi:10.2310/6350.2005.31316

53. Damsky WE, Rosenbaum LE, Bosenberg M. Decoding Melanoma Metastasis. *Cancers*. 2010;3(1):126-163. doi:10.3390/cancers3010126

54. Cancer Genome Atlas Network. Genomic Classification of Cutaneous Melanoma. *Cell*. 2015;161(7):1681-1696. doi:10.1016/j.cell.2015.05.044

55. Palmieri G, Colombino M, Casula M, Manca A, Mandalà M, Cossu A. Molecular Pathways in Melanomagenesis: What We Learned from Next-Generation Sequencing Approaches. *Curr Oncol Rep*. 2018;20(11). doi:10.1007/s11912-018-0733-7

56. Davies H, Bignell GR, Cox C, et al. Mutations of the BRAF gene in human cancer. *Nature*. 2002;417(6892):949-954. doi:10.1038/nature00766

57. Cohen C, Zavala-Pompa A, Sequeira JH, et al. Mitogen-actived protein kinase activation is an early event in melanoma progression. *Clin Cancer Res Off J Am Assoc Cancer Res*. 2002;8(12):3728-3733.

58. Yajima I, Kumasaka MY, Thang ND, et al. RAS/RAF/MEK/ERK and PI3K/PTEN/AKT Signaling in Malignant Melanoma Progression and Therapy. *Dermatol Res Pract*. 2012;2012. doi:10.1155/2012/354191

59. Li Y, Sun D, Sun W, Yin D. Ras-PI3K-AKT signaling promotes the occurrence and development of uveal melanoma by downregulating H3K56ac expression. *J Cell Physiol*. Published online February 15, 2019. doi:10.1002/jcp.28261

60. Omholt K, Grafström E, Kanter-Lewensohn L, Hansson J, Ragnarsson-Olding BK. KIT Pathway Alterations in Mucosal Melanomas of the Vulva and Other Sites. *Clin Cancer Res*. 2011;17(12):3933-3942. doi:10.1158/1078-0432.CCR-10-2917

61. Zuidervaart W, van Nieuwpoort F, Stark M, et al. Activation of the MAPK pathway is a common event in uveal melanomas although it rarely occurs through mutation of BRAF or RAS. *Br J Cancer*. 2005;92(11):2032-2038. doi:10.1038/sj.bjc.6602598

62. Kozar I, Margue C, Rothengatter S, Haan C, Kreis S. Many ways to resistance: How melanoma cells evade targeted therapies. *Biochim Biophys Acta BBA - Rev Cancer*. 2019;1871(2):313-322. doi:10.1016/j.bbcan.2019.02.002

63. ACS. Treating Melanoma Skin Cancer | How Is Melanoma Treated? Published 2019. Accessed October 22, 2019. https://www.cancer.org/cancer/melanoma-skin-cancer/treating.html

64. Domingues B, Lopes JM, Soares P, Pópulo H. Melanoma treatment in review. *ImmunoTargets Ther*. 2018;7:35-49. doi:10.2147/ITT.S134842

65. Matthews NH, Li W-Q, Qureshi AA, Weinstock MA, Cho E. Epidemiology of Melanoma. In: Ward WH, Farma JM, eds. *Cutaneous Melanoma: Etiology and Therapy*. Codon Publications; 2017. Accessed October 22, 2019. http://www.ncbi.nlm.nih.gov/books/NBK481862/

66. Davis LE, Shalin SC, Tackett AJ. Current state of melanoma diagnosis and treatment. *Cancer Biol Ther*. 2019;20(11):1366-1379. doi:10.1080/15384047.2019.1640032

67. Potez M, Trappetti V, Bouchet A, et al. Characterization of a B16-F10 melanoma model locally implanted into the ear pinnae of C57BL/6 mice. *PLoS ONE*. 2018;13(11). doi:10.1371/journal.pone.0206693

68. Overwijk WW, Restifo NP. B16 as a Mouse Model for Human Melanoma. *Curr Protoc Immunol Ed John E Coligan Al*. 2001;CHAPTER:Unit-20.1. doi:10.1002/0471142735.im2001s39

69. Ramani M, Mudge MC, Morris RT, et al. Zinc Oxide Nanoparticle–Poly I:C RNA Complexes: Implication as Therapeutics against Experimental Melanoma. *Mol Pharm*. 2017;14(3):614-625. doi:10.1021/acs.molpharmaceut.6b00795

70. clinicaltrials.gov. Intratumoral Injections of LL37 for Melanoma - Full Text View - ClinicalTrials.gov. Published 2019. Accessed October 22, 2019. https://clinicaltrials.gov/ct2/show/NCT02225366

71. Robert C, Karaszewska B, Schachter J, et al. Improved Overall Survival in Melanoma with Combined Dabrafenib and Trametinib. *N Engl J Med*. 2015;372(1):30-39. doi:10.1056/NEJMoa1412690

72. Sakamuri D, Glitza IC, Cuellar SLB, et al. Phase I Dose-Escalation Study of Anti–CTLA-4 Antibody Ipilimumab and Lenalidomide in Patients with Advanced Cancers. *Mol Cancer Ther*. 2018;17(3):671-676. doi:10.1158/1535-7163.MCT-17-0673

73. Weber J, Mandala M, Del Vecchio M, et al. Adjuvant Nivolumab versus Ipilimumab in Resected Stage III or IV Melanoma. *N Engl J Med*. 2017;377(19):1824-1835. doi:10.1056/NEJMoa1709030

74. First Spherical Nucleic Acid Drug Injected Into Humans Targets Brain Cancer. Northwestern Engineering. Accessed October 7, 2020. https://www.mccormick.northwestern.edu/news/articles/2017/05/first-spherical-nucleic-acid-drug-injected-into-humans-targets-brain-cancer.html

75. Li J, Wang Y, Liang R, et al. Recent advances in targeted nanoparticles drug delivery to melanoma. *Nanomedicine Nanotechnol Biol Med*. 2015;11(3):769-794. doi:10.1016/j.nano.2014.11.006

76. Liu Q, Das M, Liu Y, Huang L. Targeted drug delivery to melanoma. *Adv Drug Deliv Rev*. 2018;127:208-221. doi:10.1016/j.addr.2017.09.016

77. Danhier F, Feron O, Préat V. To exploit the tumor microenvironment: Passive and active tumor targeting of nanocarriers for anti-cancer drug delivery. *J Controlled Release*. 2010;148(2):135-146. doi:10.1016/j.jconrel.2010.08.027

78. Rosenblum D, Joshi N, Tao W, Karp JM, Peer D. Progress and challenges towards targeted delivery of cancer therapeutics. *Nat Commun*. 2018;9(1):1410. doi:10.1038/s41467-018-03705-y

79. Sykes EA, Dai Q, Sarsons CD, et al. Tailoring nanoparticle designs to target cancer based on tumor pathophysiology. *Proc Natl Acad Sci*. 2016;113(9).

80. Cao Y, Wang B, Wang Y, Lou D. Dual Drug Release from Core–Shell Nanoparticles with Distinct Release Profiles. *J Pharm Sci*. 2014;103(10):3205-3216. doi:10.1002/jps.24116

81. Wilhelm S, Tavares AJ, Dai Q, et al. Analysis of nanoparticle delivery to tumours. *Nat Rev Mater*. 2016;1(5):16014. doi:10.1038/natrevmats.2016.14

82. Delong RK, Risor A, Kanomata M, et al. Characterization of biomolecular nanoconjugates by high-throughput delivery and spectroscopic difference. *Nanomed*. 2012;7(12):1851-1862. doi:10.2217/nnm.12.70

83. DeLong RK, Akhtar U, Sallee M, et al. Characterization and performance of nucleic acid nanoparticles combined with protamine and gold. *Biomaterials*. 2009;30(32):6451-6459. doi:10.1016/j.biomaterials.2009.07.067

84. US Patent for Nucleic acid coated particles suitable for temporary storage Patent (Patent # 8,349,364 issued January 8, 2013) - Justia Patents Search. Accessed October 7, 2020. https://patents.justia.com/patent/8349364

85. Gopala Krishna P, Paduvarahalli Ananthaswamy P, Yadavalli T, Bhangi Mutta N, Sannaiah A, Shivanna Y. ZnO nanopellets have selective anticancer activity. *Mater Sci Eng C*. 2016;62:919-926. doi:10.1016/j.msec.2016.02.039

86. Mishra PK, Mishra H, Ekielski A, Talegaonkar S, Vaidya B. Zinc oxide nanoparticles: a promising nanomaterial for biomedical applications. *Drug Discov Today*. 2017;22(12):1825-1835. doi:10.1016/j.drudis.2017.08.006

87. Moon S-H, Choi WJ, Choi S-W, et al. Anti-cancer activity of ZnO chips by sustained zinc ion release. *Toxicol Rep*. 2016;3:430-438. doi:10.1016/j.toxrep.2016.03.008

88. Rasmussen JW, Martinez E, Louka P, Wingett DG. Zinc oxide nanoparticles for selective destruction of tumor cells and potential for drug delivery applications. *Expert Opin Drug Deliv*. 2010;7(9):1063-1078. doi:10.1517/17425247.2010.502560

89. DeLong RK, Reynolds CM, Malcolm Y, Schaeffer A, Severs T, Wanekaya A. Functionalized gold nanoparticles for the binding, stabilization, and delivery of therapeutic DNA, RNA, and other biological macromolecules. *Nanotechnol Sci Appl*. 2010;3:53-63. doi:10.2147/NSA.S8984

90. Dai Q, Wilhelm S, Ding D, et al. Quantifying the Ligand-Coated Nanoparticle Delivery to Cancer Cells in Solid Tumors. *ACS Nano*. 2018;12(8):8423-8435. doi:10.1021/acsnano.8b03900

91. Zhang H, Ji Z, Xia T, et al. Use of metal oxide nanoparticle band gap to develop a predictive paradigm for oxidative stress and acute pulmonary inflammation. *ACS Nano*. 2012;6(5):4349-4368. doi:10.1021/nn3010087

92. Ganguly A, Trinh P, Ramanujachary KV, Ahmad T, Mugweru A, Ganguli AK. Reverse micellar based synthesis of ultrafine MgO nanoparticles (8-10 nm): characterization and catalytic properties. *J Colloid Interface Sci*. 2011;353(1):137-142. doi:10.1016/j.jcis.2010.09.041

93. Lin Y-G, Hsu Y-K, Chen S-Y, Lin Y-K, Chen L-C, Chen K-H. Nanostructured zinc oxide nanorods with copper nanoparticles as a microreformation catalyst. *Angew Chem Int Ed Engl*. 2009;48(41):7586-7590. doi:10.1002/anie.200902907

94. Barber S, Abdelhakiem M, Ghosh K, et al. Effects of nanomaterials on luciferase with significant protection and increased enzyme activity observed for zinc oxide nanomaterials. *J Nanosci Nanotechnol*. 2011;11(12):10309-10319. doi:10.1166/jnn.2011.5013

95. Canoa P, Simón-Vázquez R, Popplewell J, González-Fernández Á. A quantitative binding study of fibrinogen and human serum albumin to metal oxide nanoparticles by surface plasmon resonance. *Biosens Bioelectron*. 2015;74:376-383. doi:10.1016/j.bios.2015.05.070

96. Gann H, Glaspell G, Garrad R, et al. Interaction of MnO and ZnO nanomaterials with biomedically important proteins and cells. *J Biomed Nanotechnol*. 2010;6(1):37-42. doi:10.1166/jbn.2010.1100

97. Simpson RM, Bastian BC, Michael HT, et al. Sporadic naturally occurring melanoma in dogs as a preclinical model for human melanoma. *Pigment Cell Melanoma Res*. 2014;27(1):37-47. doi:10.1111/pcmr.12185

98. Cha S-H, Hong J, McGuffie M, Yeom B, VanEpps JS, Kotov NA. Shape-Dependent Biomimetic Inhibition of Enzyme by Nanoparticles and Their Antibacterial Activity. *ACS Nano*. 2015;9(9):9097-9105. doi:10.1021/acsnano.5b03247

99. McCall J, Smith JJ, Marquardt KN, et al. ZnO Nanoparticles Protect RNA from Degradation Better than DNA. *Nanomater Basel Switz*. 2017;7(11):378. doi:10.3390/nano7110378

100. Benezra M, Penate-Medina O, Zanzonico PB, et al. Multimodal silica nanoparticles are effective cancer-targeted probes in a model of human melanoma. *J Clin Invest*. 2011;121(7):2768-2780. doi:10.1172/JCI45600

101. Du Y, Xia L, Jo A, et al. Synthesis and Evaluation of Doxorubicin-Loaded Gold Nanoparticles for Tumor-Targeted Drug Delivery. *Bioconjug Chem*. 2018;29(2):420-430. doi:10.1021/acs.bioconjchem.7b00756

102. Hue JJ, Lee H-J, Nam SY, Kim J-S, Lee BJ, Yun YW. Distribution and accumulation of ^{177}Lu-labeled thermally cross-linked superparamagnetic iron oxide nanoparticles in the tissues of ICR mice. *Korean J Vet Res*. 2015;55(1):57-60. doi:10.14405/kjvr.2015.55.1.57

103. Lellouche E, Israel LL, Bechor M, et al. MagRET Nanoparticles: An Iron Oxide Nanocomposite Platform for Gene Silencing from MicroRNAs to Long Noncoding RNAs. *Bioconjug Chem*. 2015;26(8):1692-1701. doi:10.1021/acs.bioconjchem.5b00276

104. Poon W, Zhang X, Bekah D, Teodoro JG, Nadeau JL. Targeting B16 tumorsin vivowith peptide-conjugated gold nanoparticles. *Nanotechnology*. 2015;26(28):285101. doi:10.1088/0957-4484/26/28/285101

105. Manshian BB, Pokhrel S, Himmelreich U, et al. In Silico Design of Optimal Dissolution Kinetics of Fe-Doped ZnO Nanoparticles Results in Cancer-Specific Toxicity in a Preclinical Rodent Model. *Adv Healthc Mater*. 2017;6(9):1601379. doi:10.1002/adhm.201601379

106. Lee C-M, Jeong H-J, Yun K-N, et al. Optical imaging to trace near infrared fluorescent zinc oxide nanoparticles following oral exposure. *Int J Nanomedicine*. 2012;7:3203-3209. doi:10.2147/IJN.S32828

107. Fujihara J, Tongu M, Hashimoto H, et al. Distribution and toxicity evaluation of ZnO dispersion nanoparticles in single intravenously exposed mice. *J Med Investig JMI*. 2015;62(1-2):45-50. doi:10.2152/jmi.62.45

108. Roy R, Kumar S, Verma AK, et al. Zinc oxide nanoparticles provide an adjuvant effect to ovalbumin via a Th2 response in Balb/c mice. *Int Immunol*. 2014;26(3):159-172. doi:10.1093/intimm/dxt053

109. Hong H, Wang F, Zhang Y, et al. Red Fluorescent Zinc Oxide Nanoparticle: A Novel Platform for Cancer Targeting. *ACS Appl Mater Interfaces*. 2015;7(5):3373-3381. doi:10.1021/am508440j

110. Ye D-X, Ma Y-Y, Zhao W, et al. ZnO-Based Nanoplatforms for Labeling and Treatment of Mouse Tumors without Detectable Toxic Side Effects. *ACS Nano*. 2016;10(4):4294-4300. doi:10.1021/acsnano.5b07846

111. Choi S-J, Choy J-H. Biokinetics of zinc oxide nanoparticles: toxicokinetics, biological fates, and protein interaction. *Int J Nanomedicine*. 2014;9(Suppl 2):261-269. doi:10.2147/IJN.S57920

112. Riviere JE. Pharmacokinetics of nanomaterials: an overview of carbon nanotubes, fullerenes and quantum dots. *Wiley Interdiscip Rev Nanomed Nanobiotechnol*. 2009;1(1):26-34. doi:10.1002/wnan.24

113. Baek M, Chung H-E, Yu J, et al. Pharmacokinetics, tissue distribution, and excretion of zinc oxide nanoparticles. *Int J Nanomedicine*. 2012;7:3081-3097. doi:10.2147/IJN.S32593

114. Paek H-J, Lee Y-J, Chung H-E, et al. Modulation of the pharmacokinetics of zinc oxide nanoparticles and their fates in vivo. *Nanoscale*. 2013;5(23):11416-11427. doi:10.1039/C3NR02140H

115. Wang C, Lu J, Zhou L, et al. Effects of Long-Term Exposure to Zinc Oxide Nanoparticles on Development, Zinc Metabolism and Biodistribution of Minerals (Zn, Fe, Cu, Mn) in Mice. *PLOS ONE*. 2016;11(10):e0164434. doi:10.1371/journal.pone.0164434

116. Yeh T-K, Chen J-K, Lin C-H, et al. Kinetics and tissue distribution of neutron-activated zinc oxide nanoparticles and zinc nitrate in mice: effects of size and particulate nature. *Nanotechnology*. 2012;23(8):085102. doi:10.1088/0957-4484/23/8/085102

117. Li C-H, Shen C-C, Cheng Y-W, et al. Organ biodistribution, clearance, and genotoxicity of orally administered zinc oxide nanoparticles in mice. *Nanotoxicology*. 2012;6(7):746-756. doi:10.3109/17435390.2011.620717

118. Choi J, Kim H, Kim P, et al. Toxicity of Zinc Oxide Nanoparticles in Rats Treated by Two Different Routes: Single Intravenous Injection and Single Oral Administration. *J Toxicol Environ Health A*. 2015;78(4):226-243. doi:10.1080/15287394.2014.949949

119. Nicolas J, Mura S, Brambilla D, Mackiewicz N, Couvreur P. Design, functionalization strategies and biomedical applications of targeted biodegradable/biocompatible polymer-based nanocarriers for drug delivery. *Chem Soc Rev*. 2013;42(3):1147-1235. doi:10.1039/c2cs35265f

120. Zhang Z, Wan J, Sun L, Li Y, Guo J, Wang C. Zinc finger-inspired nanohydrogels with glutathione/pH triggered degradation based on coordination substitution for highly efficient delivery of anti-cancer drugs. *J Controlled Release*. 2016;225:96-108. doi:10.1016/j.jconrel.2016.01.035

121. Li M, Zou P, Tyner K, Lee S. Physiologically Based Pharmacokinetic (PBPK) Modeling of Pharmaceutical Nanoparticles. *AAPS J*. 2017;19(1):26-42. doi:10.1208/s12248-016-0010-3

122. Li M, Al-Jamal KT, Kostarelos K, Reineke J. Physiologically based pharmacokinetic modeling of nanoparticles. *ACS Nano*. 2010;4(11):6303-6317. doi:10.1021/nn1018818

123. Lin Z, Monteiro-Riviere NA, Riviere JE. Pharmacokinetics of metallic nanoparticles. *WIREs Nanomedicine Nanobiotechnology*. 2015;7(2):189-217. doi:10.1002/wnan.1304

124. Bachler G, Goetz N von, Hungerbuhler K. Using physiologically based pharmacokinetic (PBPK) modeling for dietary risk assessment of titanium dioxide (TiO2) nanoparticles. *Nanotoxicology*. 2015;9(3):373-380. doi:10.3109/17435390.2014.940404

125. Carlander U, Li D, Jolliet O, Emond C, Johanson G. Toward a general physiologically-based pharmacokinetic model for intravenously injected nanoparticles. *Int J Nanomedicine*. 2016;11:625-640. doi:10.2147/IJN.S94370

126. Chen W-Y, Cheng Y-H, Hsieh N-H, et al. Physiologically based pharmacokinetic modeling of zinc oxide nanoparticles and zinc nitrate in mice. *Int J Nanomedicine*. 2015;10:6277-6292. doi:10.2147/IJN.S86785

127. Lankveld DPK, Oomen AG, Krystek P, et al. The kinetics of the tissue distribution of silver nanoparticles of different sizes. *Biomaterials*. 2010;31(32):8350-8361. doi:10.1016/j.biomaterials.2010.07.045

128. Lin Z, Monteiro-Riviere NA, Riviere JE. A physiologically based pharmacokinetic model for polyethylene glycol-coated gold nanoparticles of different sizes in adult mice. *Nanotoxicology*. 2016;10(2):162-172. doi:10.3109/17435390.2015.1027314

129. Lin Z, Monteiro-Riviere NA, Kannan R, Riviere JE. A computational framework for interspecies pharmacokinetics, exposure and toxicity assessment of gold nanoparticles. *Nanomed*. 2016;11(2):107-119. doi:10.2217/nnm.15.177

130. Alvarez CE. Naturally occurring cancers in dogs: insights for translational genetics and medicine. *ILAR J*. 2014;55(1):16-45. doi:10.1093/ilar/ilu010

131. Gordon IK, Khanna C. Modeling opportunities in comparative oncology for drug development. *ILAR J*. 2010;51(3):214-220. doi:10.1093/ilar.51.3.214

132. Hansen K, Khanna C. Spontaneous and genetically engineered animal models; use in preclinical cancer drug development. *Eur J Cancer Oxf Engl 1990*. 2004;40(6):858-880. doi:10.1016/j.ejca.2003.11.031

133. Khanna C, London C, Vail D, Mazcko C, Hirschfeld S. Guiding the Optimal Translation of New Cancer Treatments From Canine to Human Cancer Patients. *Clin Cancer Res*. 2009;15(18):5671-5677. doi:10.1158/1078-0432.CCR-09-0719

134. LeBlanc AK, Mazcko CN, Khanna C. Defining the Value of a Comparative Approach to Cancer Drug Development. *Clin Cancer Res*. 2016;22(9):2133-2138. doi:10.1158/1078-0432.CCR-15-2347

135. Nass SJ, Gorby H. The role of clinical studies for pets with naturally occurring tumors in translational cancer research: workshop summary (2015). *Role Clin Stud Pets Nat Occur Tumors Transl Cancer Res Workshop Summ 2015*. Published online 2015. Accessed October 8, 2020. https://www.cabdirect.org/cabdirect/abstract/20163095345

136. Paoloni M, Khanna C. Translation of new cancer treatments from pet dogs to humans. *Nat Rev Cancer*. 2008;8(2):147-156. doi:10.1038/nrc2273

137. Pinho SS, Carvalho S, Cabral J, Reis CA, Gärtner F. Canine tumors: a spontaneous animal model of human carcinogenesis. *Transl Res J Lab Clin Med*. 2012;159(3):165-172. doi:10.1016/j.trsl.2011.11.005

138. Porrello A, Cardelli P, Spugnini EP. Oncology of companion animals as a model for humans. an overview of tumor histotypes. *J Exp Clin Cancer Res CR*. 2006;25(1):97-105.

139. Rowell JL, McCarthy DO, Alvarez CE. Dog models of naturally occurring cancer. *Trends Mol Med*. 2011;17(7):380-388. doi:10.1016/j.molmed.2011.02.004

140. Schiffman JD, Breen M. Comparative oncology: what dogs and other species can teach us about humans with cancer. *Philos Trans R Soc B Biol Sci*. 2015;370(1673):20140231. doi:10.1098/rstb.2014.0231

141. Adams VJ, Evans KM, Sampson J, Wood JLN. Methods and mortality results of a health survey of purebred dogs in the UK. *J Small Anim Pract*. 2010;51(10):512-524. doi:10.1111/j.1748-5827.2010.00974.x

142. Bronson RT. Variation in age at death of dogs of different sexes and breeds. *Am J Vet Res*. 1982;43(11):2057-2059.

143. Gordon I, Paoloni M, Mazcko C, Khanna C. The Comparative Oncology Trials Consortium: Using Spontaneously Occurring Cancers in Dogs to Inform the Cancer Drug Development Pathway. *PLOS Med*. 2009;6(10):e1000161. doi:10.1371/journal.pmed.1000161

144. Ito D, Frantz AM, Modiano JF. Canine lymphoma as a comparative model for human non-Hodgkin lymphoma: recent progress and applications. *Vet Immunol Immunopathol*. 2014;159(3):192-201. doi:10.1016/j.vetimm.2014.02.016

145. Simpson S, Dunning MD, de Brot S, Grau-Roma L, Mongan NP, Rutland CS. Comparative review of human and canine osteosarcoma: morphology, epidemiology, prognosis, treatment and genetics. *Acta Vet Scand*. 2017;59(1):71. doi:10.1186/s13028-017-0341-9

146. Knapp DW, Ramos-Vara JA, Moore GE, Dhawan D, Bonney PL, Young KE. Urinary bladder cancer in dogs, a naturally occurring model for cancer biology and drug development. *ILAR J*. 2014;55(1):100-118. doi:10.1093/ilar/ilu018

147. Hicks J, Platt S, Kent M, Haley A. Canine brain tumours: a model for the human disease? *Vet Comp Oncol*. 2017;15(1):252-272. doi:10.1111/vco.12152

148. Hernandez B, Adissu HA, Wei B-R, Michael HT, Merlino G, Simpson RM. Naturally Occurring Canine Melanoma as a Predictive Comparative Oncology Model for Human Mucosal and Other Triple Wild-Type Melanomas. *Int J Mol Sci*. 2018;19(2). doi:10.3390/ijms19020394

149. American Cancer Society. Cancer Facts & Figures 2018 | American Cancer Society. Published 2018. Accessed October 8, 2020. https://www.cancer.org/research/cancer-facts-statistics/all-cancer-facts-figures/cancer-facts-figures-2018.html

150. Bergman PJ. Canine Oral Melanoma. *Clin Tech Small Anim Pract*. 2007;22(2):55-60. doi:10.1053/j.ctsap.2007.03.004

151. Kunz M. Oncogenes in melanoma: an update. *Eur J Cell Biol*. 2014;93(1-2):1-10. doi:10.1016/j.ejcb.2013.12.002

152. Sulaimon SS, Kitchell BE. The basic biology of malignant melanoma: molecular mechanisms of disease progression and comparative aspects. *J Vet Intern Med*. 2003;17(6):760-772. doi:10.1111/j.1939-1676.2003.tb02513.x

153. Bergman PJ, Kent MS, Farese JP. 19 - Melanoma. In: Withrow SJ, Vail DM, Page RL, eds. *Withrow and MacEwen's Small Animal Clinical Oncology (Fifth Edition)*. W.B. Saunders; 2013:321-334. doi:10.1016/B978-1-4377-2362-5.00019-0

154. Ascierto PA, Kirkwood JM, Grob J-J, et al. The role of BRAF V600 mutation in melanoma. *J Transl Med*. 2012;10:85. doi:10.1186/1479-5876-10-85

155. Kelleher FC, McArthur GA. Targeting NRAS in melanoma. *Cancer J Sudbury Mass*. 2012;18(2):132-136. doi:10.1097/PPO.0b013e31824ba4df

156. Kiuru M, Busam KJ. The NF1 gene in tumor syndromes and melanoma. *Lab Investig J Tech Methods Pathol*. 2017;97(2):146-157. doi:10.1038/labinvest.2016.142

157. Curtin JA, Busam K, Pinkel D, Bastian BC. Somatic Activation of KIT in Distinct Subtypes of Melanoma. *J Clin Oncol*. 2006;24(26):4340-4346. doi:10.1200/JCO.2006.06.2984

158. Fowles JS, Denton CL, Gustafson DL. Comparative analysis of MAPK and PI3K/AKT pathway activation and inhibition in human and canine melanoma. *Vet Comp Oncol*. 2015;13(3):288-304. doi:10.1111/vco.12044

159. Hendricks WPD, Zismann V, Sivaprakasam K, et al. Somatic inactivating PTPRJ mutations and dysregulated pathways identified in canine malignant melanoma by integrated comparative genomic analysis. *PLOS Genet*. 2018;14(9):e1007589. doi:10.1371/journal.pgen.1007589

160. Chang AE, Karnell LH, Menck HR. The National Cancer Data Base report on cutaneous and noncutaneous melanoma: a summary of 84,836 cases from the past decade. The American College of Surgeons Commission on Cancer and the American Cancer Society. *Cancer*. 1998;83(8):1664-1678. doi:10.1002/(sici)1097-0142(19981015)83:8<1664::aid-cncr23>3.0.co;2-g

161. Bocanegra Gondan AI, Ruiz-de-Angulo A, Zabaleta A, et al. Effective cancer immunotherapy in mice by polyIC-imiquimod complexes and engineered magnetic nanoparticles. *Biomaterials*. 2018;170:95-116. doi:10.1016/j.biomaterials.2018.04.003

162. Adams BD, Parsons C, Walker L, Zhang WC, Slack FJ. Targeting noncoding RNAs in disease. *J Clin Invest*. 2017;127(3):761-771. doi:10.1172/JCI84424

163. Gragoudas ES, Adamis AP, Cunningham ET, Feinsod M, Guyer DR, VEGF Inhibition Study in Ocular Neovascularization Clinical Trial Group. Pegaptanib for neovascular age-related macular degeneration. *N Engl J Med*. 2004;351(27):2805-2816. doi:10.1056/NEJMoa042760

164. Stein CA, Castanotto D. FDA-Approved Oligonucleotide Therapies in 2017. *Mol Ther J Am Soc Gene Ther*. 2017;25(5):1069-1075. doi:10.1016/j.ymthe.2017.03.023

165. DeLong RK, Nolting A, Fisher M, et al. Comparative pharmacokinetics, tissue distribution, and tumor accumulation of phosphorothioate, phosphorodithioate, and methylphosphonate oligonucleotides in nude mice. *Antisense Nucleic Acid Drug Dev*. 1997;7(2):71-77. doi:10.1089/oli.1.1997.7.71

166. Salton M, Kasprzak WK, Voss T, Shapiro BA, Poulikakos PI, Misteli T. Inhibition of vemurafenib-resistant melanoma by interference with pre-mRNA splicing. *Nat Commun*. 2015;6(1):7103. doi:10.1038/ncomms8103

167. Poulikakos PI, Persaud Y, Janakiraman M, et al. RAF inhibitor resistance is mediated by dimerization of aberrantly spliced BRAF(V600E). *Nature*. 2011;480(7377):387-390. doi:10.1038/nature10662

168. Mathew EN, Hurst MN, Murthy, Vaibhav, Wang B, DeLong RK. Interaction of Ras Binding Domain (RBD) by Chemotherapeutic Zinc Oxide Nanoparticles: Progress towards RAS Pathway Protein Interference. Published online Submitted.

169. Cheng X, DeLong RK, Wickstrom E, et al. Interactions between single-stranded DNA binding protein and oligonucleotide analogs with different backbone chemistries. *J Mol Recognit JMR*. 1997;10(2):101-107. doi:10.1002/(SICI)1099-1352(199703/04)10:2<101::AID-JMR344>3.0.CO;2-4

170. Kimoto M, Shirouzu M, Mizutani S, et al. Anti-(Raf-1) RNA aptamers that inhibit Ras-induced Raf-1 activation. *Eur J Biochem*. 2002;269(2):697-704. doi:10.1046/j.0014-2956.2001.02703.x

171. DeLong Lab. Unpublished Data.

172. Bhaumik A, Shearin AM, Delong R, Wanekaya A, Ghosh K. Probing the Interaction at the Nano–Bio Interface Using Raman Spectroscopy: ZnO Nanoparticles and Adenosine Triphosphate Biomolecules. *J Phys Chem C*. 2014;118(32):18631-18639. doi:10.1021/jp506200a

173. DeLong RK, Hurst MN. Two dimensional fluorescence difference spectroscopy characterization of nanoparticles and their interactions. Published online May 22, 2018.

174. Hurst MN, DeLong RK. Two-Dimensional Fluorescence Difference Spectroscopy to Characterize Nanoparticles and their Interactions. *Sci Rep*. 2016;6(1):33287. doi:10.1038/srep33287

175. Cobaleda-Siles M, Henriksen-Lacey M, Angulo AR de, et al. An Iron Oxide Nanocarrier for dsRNA to Target Lymph Nodes and Strongly Activate Cells of the Immune System. *Small*. 2014;10(24):5054-5067. doi:10.1002/smll.201401353

176. DeLong RK, Curtis CB. Toward RNA nanoparticle vaccines: synergizing RNA and inorganic nanoparticles to achieve immunopotentiation. *WIREs Nanomedicine Nanobiotechnology*. 2017;9(2):e1415. doi:10.1002/wnan.1415

177. Jia J, Zheng Y, Wang W, et al. Antimicrobial peptide LL-37 promotes YB-1 expression, and the viability, migration and invasion of malignant melanoma cells. *Mol Med Rep*. 2017;15(1):240-248. doi:10.3892/mmr.2016.5978

178. Singh D, Qi R, Jordan JL, San Mateo L, Kao CC. The Human Antimicrobial Peptide LL-37, but Not the Mouse Ortholog, mCRAMP, Can Stimulate Signaling by Poly(I:C) through a FPRL1-dependent Pathway. *J Biol Chem*. 2013;288(12):8258-8268. doi:10.1074/jbc.M112.440883

179. Felício MR, Silva ON, Gonçalves S, Santos NC, Franco OL. Peptides with Dual Antimicrobial and Anticancer Activities. *Front Chem*. 2017;5. doi:10.3389/fchem.2017.00005

180. Kauffman KJ, Dorkin JR, Yang JH, et al. Optimization of Lipid Nanoparticle Formulations for mRNA Delivery in Vivo with Fractional Factorial and Definitive Screening Designs. *Nano Lett*. 2015;15(11):7300-7306. doi:10.1021/acs.nanolett.5b02497

181. Oberli MA, Reichmuth AM, Dorkin JR, et al. Lipid Nanoparticle Assisted mRNA Delivery for Potent Cancer Immunotherapy. *Nano Lett*. 2017;17(3):1326-1335. doi:10.1021/acs.nanolett.6b03329

182. Kumari N, Dwarakanath BS, Das A, Bhatt AN. Role of interleukin-6 in cancer progression and therapeutic resistance. *Tumor Biol*. 2016;37(9):11553-11572. doi:10.1007/s13277-016-5098-7

183. Shao K, Singha S, Clemente-Casares X, Tsai S, Yang Y, Santamaria P. Nanoparticle-Based Immunotherapy for Cancer. *ACS Nano*. 2015;9(1):16-30. doi:10.1021/nn5062029

184. Roy R, Das M, Dwivedi PD. Toxicological mode of action of ZnO nanoparticles: Impact on immune cells. *Mol Immunol*. 2015;63(2):184-192. doi:10.1016/j.molimm.2014.08.001

185. Medberry P, Dennis S, Van Hecke T, DeLong RK. pDNA bioparticles: comparative heterogeneity, surface, binding, and activity analyses. *Biochem Biophys Res Commun*. 2004;319(2):426-432. doi:10.1016/j.bbrc.2004.04.188

186. Knowle R, Werner A, DeLong RK. R4 Peptide-pDNA Nanoparticle Coated HepB Vaccine Microparticles: Sedimentation, Partitioning, and Spray Freeze Dry Bioprocesses. *J Nanosci Nanotechnol*. 2006;6(9-10):2783-2789. doi:10.1166/jnn.2006.427

187. Murray AR, Kisin E, Inman A, et al. Oxidative Stress and Dermal Toxicity of Iron Oxide Nanoparticles In Vitro. *Cell Biochem Biophys*. 2013;67(2):461-476. doi:10.1007/s12013-012-9367-9

188. Cohen J. A power primer. - PsycNET. Published 1992. Accessed October 8, 2020. https://psycnet.apa.org/doiLanding?doi=10.1037%2F0033-2909.112.1.155

189. Cohen J. *Statistical Power Analysis for the Behavioral Sciences*. Academic Press; 2013.

190. Raymand D, van Duin ACT, Baudin M, Hermansson K. A reactive force field (ReaxFF) for zinc oxide. *Surf Sci*. 2008;602(5):1020-1031. doi:10.1016/j.susc.2007.12.023

191. Plimpton S. Fast Parallel Algorithms for Short-Range Molecular Dynamics. *J Comput Phys*. 1995;117(1):1-19. doi:10.1006/jcph.1995.1039

192. Huang J, Rauscher S, Nawrocki G, et al. CHARMM36m: an improved force field for folded and intrinsically disordered proteins. *Nat Methods*. 2017;14(1):71-73. doi:10.1038/nmeth.4067

193. Zhang Y, Chen R, Riviere JE, Comer J. Extraction of aromatic organochlorines from water by ZnO nanoparticles. Published online Submitted.

194. Wang G. Structures of Human Host Defense Cathelicidin LL-37 and Its Smallest Antimicrobial Peptide KR-12 in Lipid Micelles. *J Biol Chem*. 2008;283(47):32637-32643. doi:10.1074/jbc.M805533200

195. Phillips JC, Braun R, Wang W, et al. Scalable molecular dynamics with NAMD. *J Comput Chem*. 2005;26(16):1781-1802. doi:10.1002/jcc.20289

196. Hopkins CW, Le Grand S, Walker RC, Roitberg AE. Long-Time-Step Molecular Dynamics through Hydrogen Mass Repartitioning. *J Chem Theory Comput*. 2015;11(4):1864-1874. doi:10.1021/ct5010406

197. Miyamoto S, Kollman PA. Settle: An analytical version of the SHAKE and RATTLE algorithm for rigid water models. *J Comput Chem*. 1992;13(8):952-962. doi:10.1002/jcc.540130805

198. Feller SE, Zhang Y, Pastor RW, Brooks BR. Constant pressure molecular dynamics simulation: The Langevin piston method. *J Chem Phys*. 1995;103(11):4613-4621. doi:10.1063/1.470648

199. Chattopadhyay S, Dash SK, Ghosh T, et al. Anticancer and immunostimulatory role of encapsulated tumor antigen containing cobalt oxide nanoparticles. *JBIC J Biol Inorg Chem*. 2013;18(8):957-973. doi:10.1007/s00775-013-1044-y

200. Larese Filon F, Crosera M, Timeus E, et al. Human skin penetration of cobalt nanoparticles through intact and damaged skin. *Toxicol In Vitro*. 2013;27(1):121-127. doi:10.1016/j.tiv.2012.09.007

201. Park E-J, Oh SY, Kim Y, et al. Distribution and immunotoxicity by intravenous injection of iron nanoparticles in a murine model. *J Appl Toxicol*. 2016;36(3):414-423. doi:10.1002/jat.3232

202. Hoffman A, Wu X, Wang J, et al. Two-Dimensional Fluorescence Difference Spectroscopy of ZnO and Mg Composites in the Detection of Physiological Protein and RNA Interactions. *Materials*. 2017;10(12):1430. doi:10.3390/ma10121430

203. Yu Y, Wang J, Liu J, Ling D, Xia J. Functional Assembly of Protein Fragments Induced by Spatial Confinement. *PLOS ONE*. 2015;10(4):e0122101. doi:10.1371/journal.pone.0122101

204. Hasan M, Ruksznis C, Wang Y, Leifer CA. Antimicrobial Peptides Inhibit Polyinosinic-Polycytidylic Acid-Induced Immune Responses. *J Immunol*. 2011;187(11):5653-5659. doi:10.4049/jimmunol.1102144

205. Quagliariello V, Masarone M, Armenia E, et al. Chitosan-coated liposomes loaded with butyric acid demonstrate anticancer and anti-inflammatory activity in human hepatoma HepG2 cells. *Oncol Rep*. 2019;41(3):1476-1486. doi:10.3892/or.2018.6932

206. Serri C, Quagliariello V, Iaffaioli RV, et al. Combination therapy for the treatment of pancreatic cancer through hyaluronic acid-decorated nanoparticles loaded with quercetin and gemcitabine: A preliminary in vitro study. *J Cell Physiol*. 2019;234(4):4959-4969. doi:10.1002/jcp.27297

207. Boltasseva A, Atwater HA. Low-Loss Plasmonic Metamaterials. *Science*. 2011;331(6015):290-291. doi:10.1126/science.1198258

208. Valentine J, Zhang S, Zentgraf T, et al. Three-dimensional optical metamaterial with a negative refractive index. *Nature*. 2008;455(7211). Accessed October 9, 2020. https://ris.uni-paderborn.de/publication/1738

209. Chen P-C, Liu X, Hedrick JL, et al. Polyelemental nanoparticle libraries. *Science*. 2016;352(6293):1565-1569. doi:10.1126/science.aaf8402

210. Wiesmann N, Tremel W, Brieger J. Zinc oxide nanoparticles for therapeutic purposes in cancer medicine. *J Mater Chem B*. 2020;8(23):4973-4989. doi:10.1039/D0TB00739K

211. DeLong RK, Dean J, Glaspell G, et al. Amino/Amido Conjugates Form to Nanoscale Cobalt Physiometacomposite (PMC) Materials Functionally Delivering Nucleic Acid Therapeutic to Nucleus Enhancing Anticancer Activity via Ras-Targeted Protein Interference. *ACS Appl Bio Mater*. 2020;3(1):175-179. doi:10.1021/acsabm.9b00798

212. Lin S, Zhao Y, Xia T, et al. High Content Screening in Zebrafish Speeds up Hazard Ranking of Transition Metal Oxide Nanoparticles. *ACS Nano*. 2011;5(9):7284-7295. doi:10.1021/nn202116p

213. Bauman JA, Li S-D, Yang A, Huang L, Kole R. Anti-tumor activity of splice-switching oligonucleotides. *Nucleic Acids Res*. 2010;38(22):8348-8356. doi:10.1093/nar/gkq731

214. Parker-Esquivel B, Flores KJ, Louiselle D, et al. Association of poly I:C RNA and plasmid DNA onto MnO nanorods mediated by PAMAM. *Langmuir ACS J Surf Colloids*. 2012;28(8):3860-3870. doi:10.1021/la203998r

215. Reyes-Reveles J, Sedaghat-Herati R, Gilley DR, et al. mPEG-PAMAM-G4 nucleic acid nanocomplexes: enhanced stability, RNase protection, and activity of splice switching oligomer and poly I:C RNA. *Biomacromolecules*. 2013;14(11):4108-4115. doi:10.1021/bm4012425

216. Hayward NK, Wilmott JS, Waddell N, et al. Whole-genome landscapes of major melanoma subtypes. *Nature*. 2017;545(7653):175-180. doi:10.1038/nature22071

217. Tenland E, Pochert A, Krishnan N, et al. Effective delivery of the anti-mycobacterial peptide NZX in mesoporous silica nanoparticles. *PLoS ONE*. 2019;14(2). doi:10.1371/journal.pone.0212858

218. Alberto Fernández-Medarde, Eugenio Santos. Ras in Cancer and Developmental Diseases Reprints and permission: *Genes Cancer*. 2011;2(3):344-359. doi:10.1177/1947601911411084

219. Vinardell MP, Mitjans M. Antitumor Activities of Metal Oxide Nanoparticles. *Nanomater Basel Switz*. 2015;5(2):1004-1022. doi:10.3390/nano5021004

220. Stern O, Volmer M. The extinction period of fluorescence. *PhysZ*. 1919;20:183-189.

221. Cho EC, Zhang Q, Xia Y. The effect of sedimentation and diffusion on cellular uptake of gold nanoparticles. *Nat Nanotechnol*. 2011;6(6):385-392. doi:10.1038/nnano.2011.58

222. Lo Giudice MC, Herda LM, Polo E, Dawson KA. In situ characterization of nanoparticle biomolecular interactions in complex biological media by flow cytometry. *Nat Commun*. 2016;7. doi:10.1038/ncomms13475

223. García-Álvarez R, Hadjidemetriou M, Sánchez-Iglesias A, Liz-Marzán LM, Kostarelos K. In vivo formation of protein corona on gold nanoparticles. The effect of their size and shape. *Nanoscale*. 2018;10(3):1256-1265. doi:10.1039/C7NR08322J

224. Chiang H-M, Xia Q, Zou X, et al. Nanoscale ZnO induces cytotoxicity and DNA damage in human cell lines and rat primary neuronal cells. *J Nanosci Nanotechnol*. 2012;12(3):2126-2136.

225. Carver K, Ming X, Juliano RL. Multicellular Tumor Spheroids as a Model for Assessing Delivery of Oligonucleotides in Three Dimensions. *Mol Ther - Nucleic Acids*. 2014;3(3). doi:10.1038/mtna.2014.5

226. van Meerloo J, Kaspers GJL, Cloos J. Cell sensitivity assays: the MTT assay. *Methods Mol Biol Clifton NJ*. 2011;731:237-246. doi:10.1007/978-1-61779-080-5_20

227. Braun K, Stürzel CM, Biskupek J, Kaiser U, Kirchhoff F, Lindén M. Comparison of different cytotoxicity assays for in vitro evaluation of mesoporous silica nanoparticles. *Toxicol Vitro Int J Publ Assoc BIBRA*. 2018;52:214-222. doi:10.1016/j.tiv.2018.06.019

228. Roudi R, Syn NL, Roudbary M. Antimicrobial Peptides As Biologic and Immunotherapeutic Agents against Cancer: A Comprehensive Overview. *Front Immunol*. 2017;8. doi:10.3389/fimmu.2017.01320

229. Dürr UHN, Sudheendra US, Ramamoorthy A. LL-37, the only human member of the cathelicidin family of antimicrobial peptides. *Biochim Biophys Acta BBA - Biomembr*. 2006;1758(9):1408-1425. doi:10.1016/j.bbamem.2006.03.030

230. Sørensen OE, Follin P, Johnsen AH, et al. Human cathelicidin, hCAP-18, is processed to the antimicrobial peptide LL-37 by extracellular cleavage with proteinase 3. *Blood*. 2001;97(12):3951-3959. doi:10.1182/blood.v97.12.3951

231. Scott MG, Davidson DJ, Gold MR, Bowdish D, Hancock REW. The Human Antimicrobial Peptide LL-37 Is a Multifunctional Modulator of Innate Immune Responses. *J Immunol*. 2002;169(7):3883-3891. doi:10.4049/jimmunol.169.7.3883

232. Piktel E, Niemirowicz K, Wnorowska U, et al. The Role of Cathelicidin LL-37 in Cancer Development. *Arch Immunol Ther Exp (Warsz)*. 2016;64(1):33-46. doi:10.1007/s00005-015-0359-5

233. Agerberth B, Gunne H, Odeberg J, Kogner P, Boman HG, Gudmundsson GH. FALL-39, a putative human peptide antibiotic, is cysteine-free and expressed in bone marrow and testis. *Proc Natl Acad Sci*. 1995;92(1):195-199. doi:10.1073/pnas.92.1.195

234. Cowland JB, Johnsen AH, Borregaard N. hCAP-18, a cathelin/pro-bactenecin-like protein of human neutrophil specific granules. *FEBS Lett*. 1995;368(1):173-176. doi:10.1016/0014-5793(95)00634-L

235. Frohm M, Agerberth B, Ahangari G, et al. The Expression of the Gene Coding for the Antibacterial Peptide LL-37 Is Induced in Human Keratinocytes during Inflammatory Disorders. *J Biol Chem*. 1997;272(24):15258-15263. doi:10.1074/jbc.272.24.15258

236. Sørensen O, Arnljots K, Cowland JB, Bainton DF, Borregaard N. The human antibacterial cathelicidin, hCAP-18, is synthesized in myelocytes and metamyelocytes and localized to specific granules in neutrophils. *Blood*. 1997;90(7):2796-2803.

237. Kuroda K, Okumura K, Isogai H, Isogai E. The Human Cathelicidin Antimicrobial Peptide LL-37 and Mimics are Potential Anticancer Drugs. *Front Oncol*. 2015;5. doi:10.3389/fonc.2015.00144

238. Shaykhiev R, Beißwenger C, Kändler K, et al. Human endogenous antibiotic LL-37 stimulates airway epithelial cell proliferation and wound closure. *Am J Physiol-Lung Cell Mol Physiol*. 2005;289(5):L842-L848. doi:10.1152/ajplung.00286.2004

239. Kim JE, Kim HJ, Choi JM, et al. The antimicrobial peptide human cationic antimicrobial protein-18/cathelicidin LL-37 as a putative growth factor for malignant melanoma. *Br J Dermatol*. 2010;163(5):959-967. doi:10.1111/j.1365-2133.2010.09957.x

240. Heilborn JD, Nilsson MF, Jimenez CIC, et al. Antimicrobial protein hCAP18/LL-37 is highly expressed in breast cancer and is a putative growth factor for epithelial cells. *Int J Cancer*. 2005;114(5):713-719. doi:10.1002/ijc.20795

241. Hase K, Murakami M, Iimura M, et al. Expression of LL-37 by human gastric epithelial cells as a potential host defense mechanism against Helicobacter pylori. *Gastroenterology*. 2003;125(6):1613-1625. doi:10.1053/j.gastro.2003.08.028

242. Yang D, Chen Q, Schmidt AP, et al. Ll-37, the Neutrophil Granule–And Epithelial Cell–Derived Cathelicidin, Utilizes Formyl Peptide Receptor–Like 1 (Fprl1) as a Receptor to Chemoattract Human Peripheral Blood Neutrophils, Monocytes, and T Cells. *J Exp Med*. 2000;192(7):1069-1074. doi:10.1084/jem.192.7.1069

243. Niemirowicz K, Prokop I, Wilczewska AZ, et al. Magnetic nanoparticles enhance the anticancer activity of cathelicidin LL-37 peptide against colon cancer cells. *Int J Nanomedicine*. 2015;10:3843-3853. doi:10.2147/IJN.S76104

244. Manarang JC, Burns AR, McDermott AM. Apoptotic Pathways of Antimicrobial Peptide-Induced Death of Uveal Melanoma Cells. *Invest Ophthalmol Vis Sci*. 2011;52(14):511-511.

245. Zhang L, Sen GL, Ward NL, et al. Antimicrobial peptide LL37 and MAVS signaling drive interferon β production by epidermal keratinocytes during skin injury. *Immunity*. 2016;45(1):119-130. doi:10.1016/j.immuni.2016.06.021

246. Ren NSX, Shen J, Cheng A, et al. FK-16 Derived from the Anticancer Peptide LL-37 Induces Caspase-Independent Apoptosis and Autophagic Cell Death in Colon Cancer Cells. *PloS One*. 2013;8:e63641. doi:10.1371/journal.pone.0063641

247. Dolkar T, Trinidad CM, Nelson KC, et al. Dermatologic toxicity from novel therapy using antimicrobial peptide LL-37 in melanoma: A detailed examination of the clinicopathologic features. *J Cutan Pathol*. 2018;45(7):539-544. doi:10.1111/cup.13262

248. Livak KJ, Schmittgen TD. Analysis of relative gene expression data using real-time quantitative PCR and the 2(-Delta Delta C(T)) Method. *Methods San Diego Calif*. 2001;25(4):402-408. doi:10.1006/meth.2001.1262

249. Protein Calculator Results. Published 2020. Accessed October 12, 2020. http://protcalc.sourceforge.net/cgi-bin/protcalc

250. Smith PK, Krohn RI, Hermanson GT, et al. Measurement of protein using bicinchoninic acid. *Anal Biochem*. 1985;150(1):76-85. doi:10.1016/0003-2697(85)90442-7

251. Walker JM. The Bicinchoninic Acid (BCA) Assay for Protein Quantitation. In: Walker JM, ed. *The Protein Protocols Handbook*. Springer Protocols Handbooks. Humana Press; 1996:11-14. doi:10.1007/978-1-60327-259-9_3

252. Wang W, Xu Y, Gao R, et al. Detection of SARS-CoV-2 in Different Types of Clinical Specimens. *JAMA*. 2020;323(18):1843-1844. doi:10.1001/jama.2020.3786

Appendix A - Supplemental Information

Biodistribution of ZnO NP-Procedure

Bioimaging of Mouse Tissues:

BALB/C mice were anesthetized using oxygen/isoflurane prior to administration with treatment and bioimaging. Animals were intravenously administered with 100 µl of with PBS or ZnO NP or ZnO NP-Cy5.5 at the dose rate of 2 mg/kg body weight. Imaging was done using a Pearl® Trilogy Small Animal Imaging System (LI-COR Biosciences, USA) immediately before and after PBS administration, 5 days after ZnO NP administration and at regular time points until 6h after ZnO NP-Cy5.5 administration. After the defined time points, animals were euthanized under anesthesia.

ICP – MS:

Tissues were collected from mice treated with, (1) PBS alone (n=1), (2) ZnO NP (n=2), and (3) ZnO NP-Cy5.5 (n=2). The concentration of zinc (Zn) in the mouse tissues was determined using ICP-MS analysis following the standard protocol. In brief, tissues were digested using 2 ml of 70% nitric acid (HNO3) for liver and 1 ml for brain, heart, lungs, spleen and kidneys. The digestion was performed in SC154 HotBlock® (Environmental Express, USA) at 90^0C overnight. Following overnight digestion, all the tissue digests were diluted by addition of 9 ml deionized water. The diluted digests were further diluted by combining 1 ml of the digest with 4 ml of 2% HNO3 and filtered using 0.2 µm filter. Zinc concentration was measured on a PerkinElmer NexION® 350D ICP-MS using Syngistix™ software (Shelton, CT, USA). The experiment was done intriplicates.

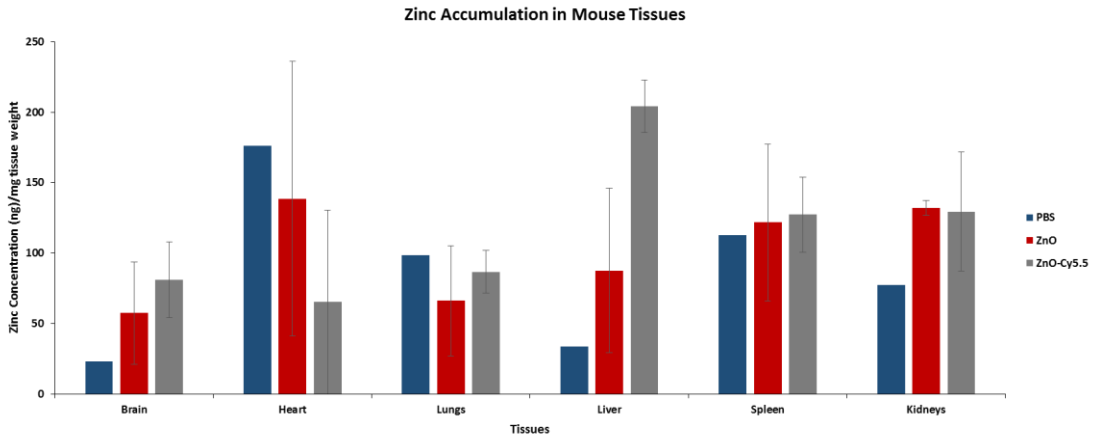

Figure A.1. Zinc accumulation in mouse tissues demonstrated by ICP-MS

Fluorescence:

Tissues were collected from mice treated with, (1) PBS alone (n=1), (2) ZnO NP (n=2), and (3) ZnO-Cy5.5 NP (n=2). Fluorescence was measured in the following tissues:

(1) PBS treated: Liver and Kidney

(2) ZnO NP treated: a. Mouse 1: Liver and kidneys b. Mouse 2: brain, heart, lungs, spleen and kidneys

(3) ZnO NP-Cy5.5 treated: brain, heart, lungs, spleen and kidneys from both mice

From the tissues collected, a portion was cut off, weighed and homogenized using SONICS VCX Vibra 130 Tissue Sonicator (PRO Scientific Inc.) at an amplitude of 50 at a pulse rate of 10s (on) and 5s (off) for 20 minutes. From the homogenate, 200 µl was transferred to a 96-well plate and fluorescence was measured using SpectraMax® i3x multimode microplate reader (Molecular Devices, California, USA). Excitation and emission wavelengths used were 660 nm and 695 nm respectively. PBS was used as the blank. The experiment was done in triplicates.

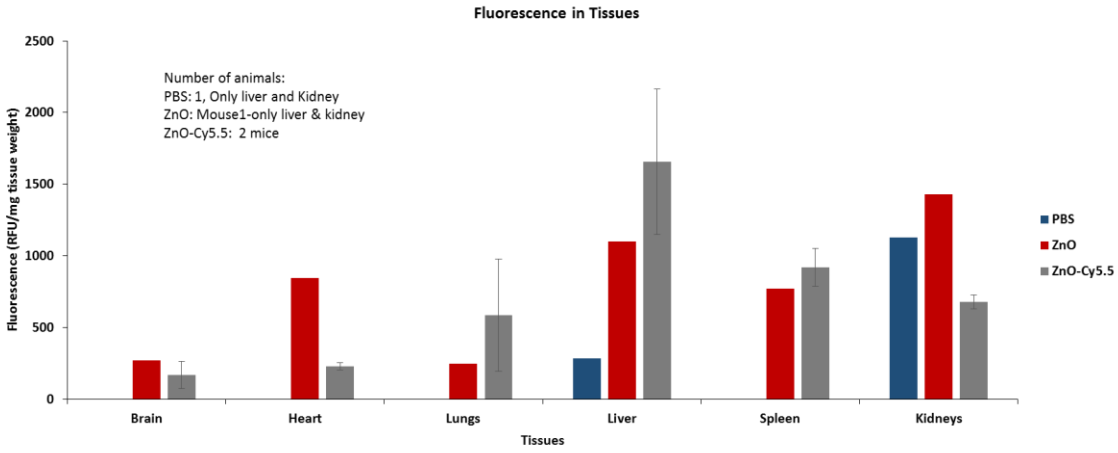

Figure A.2. Biodistribution of ZnO NP demonstrated by fluorescence measurements

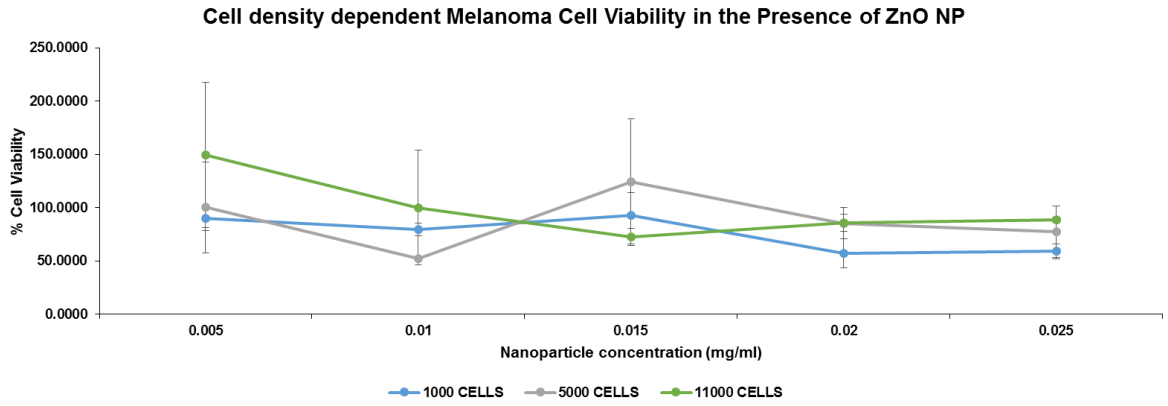

Figure A.3. Cell density dependent melanoma cell viability in the presence of ZnO NP. BLUE-1000 cells per well; GREY-500 cells per well; GREEN-11000 cells per well

Table A.1. RT-qPCR cycling conditions

Stage	Temperature (°C)	Exposure time
Holding	95	5 min
Amplification (40 cycles)	95	15 s
	60	1 min
	72	1 min
Melting and Holding	95	15 s
	60	1 min
	95	15 s

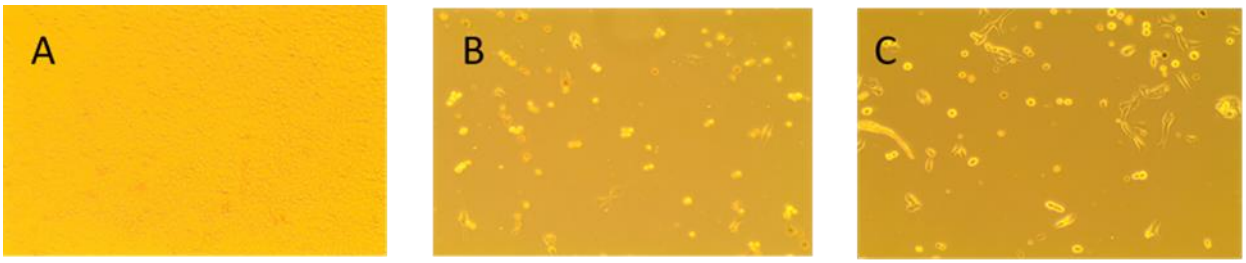

Figure A.4. Cytotoxic Activity of nanoparticles in B16F10 mouse melanoma cells at 24h of exposure. A. Untreated Cells B. Cells treated with ZnO C. Cells treated with 0.1% Ni/ZnO

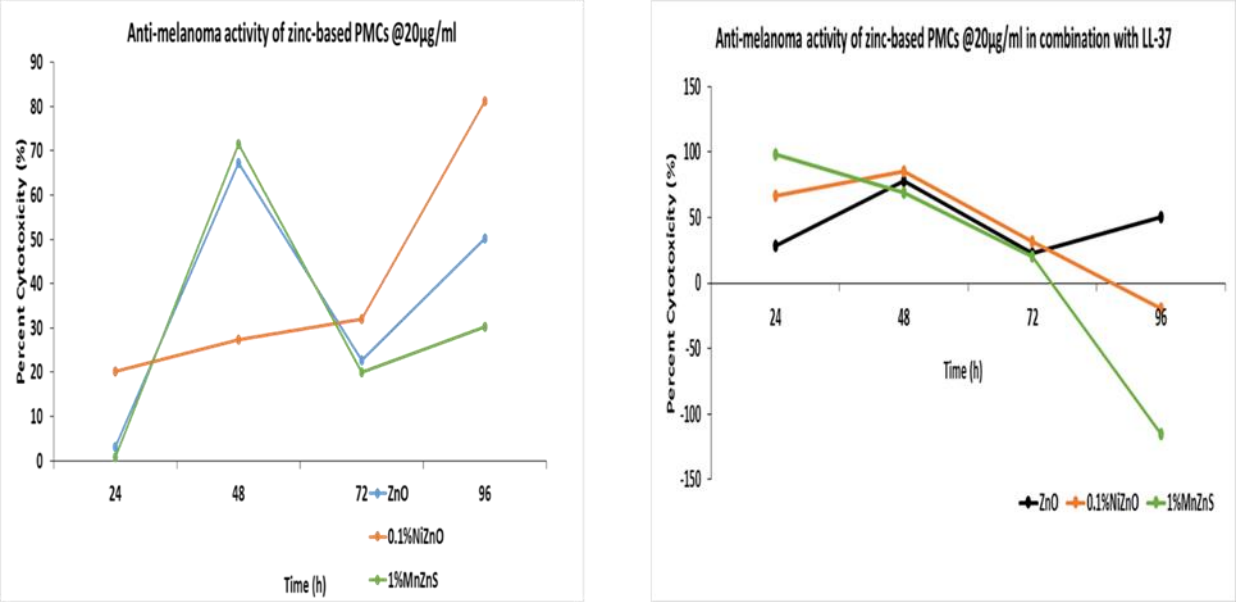

Figure A.5. Anti-melanoma activity of ZnO and its PMCs in B16F10 cells at 20µg/ml in the presence and absence of LL-37

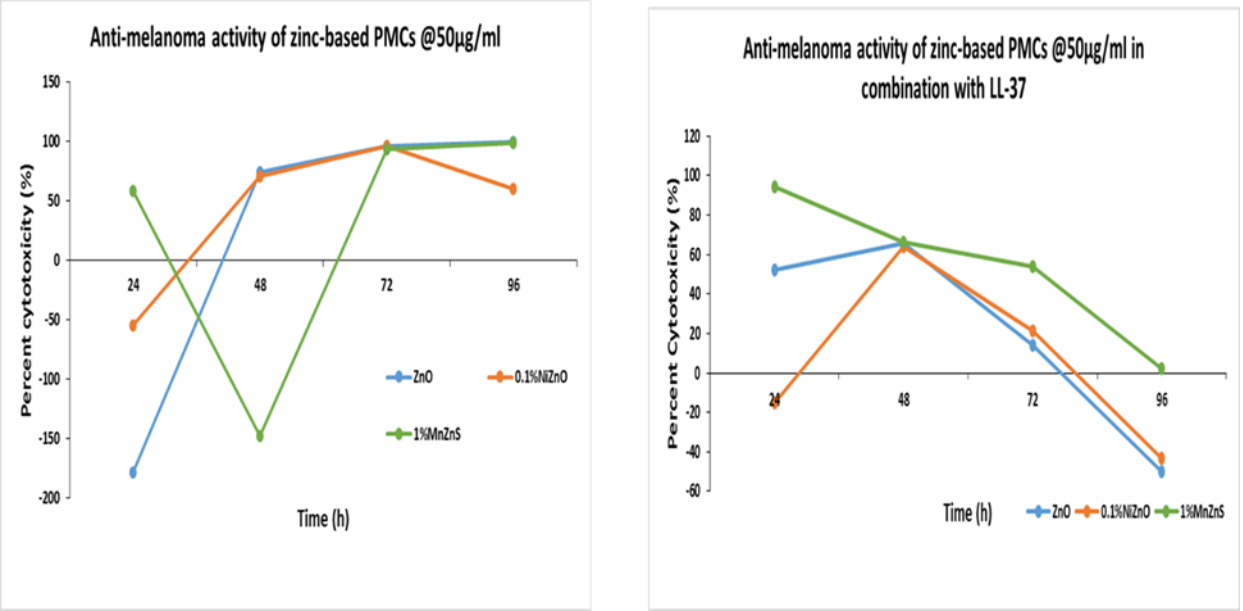

Figure A.6. Anti-melanoma activity of ZnO and its PMCs in B16F10 cells at 20µg/ml in the presence and absence of LL-37

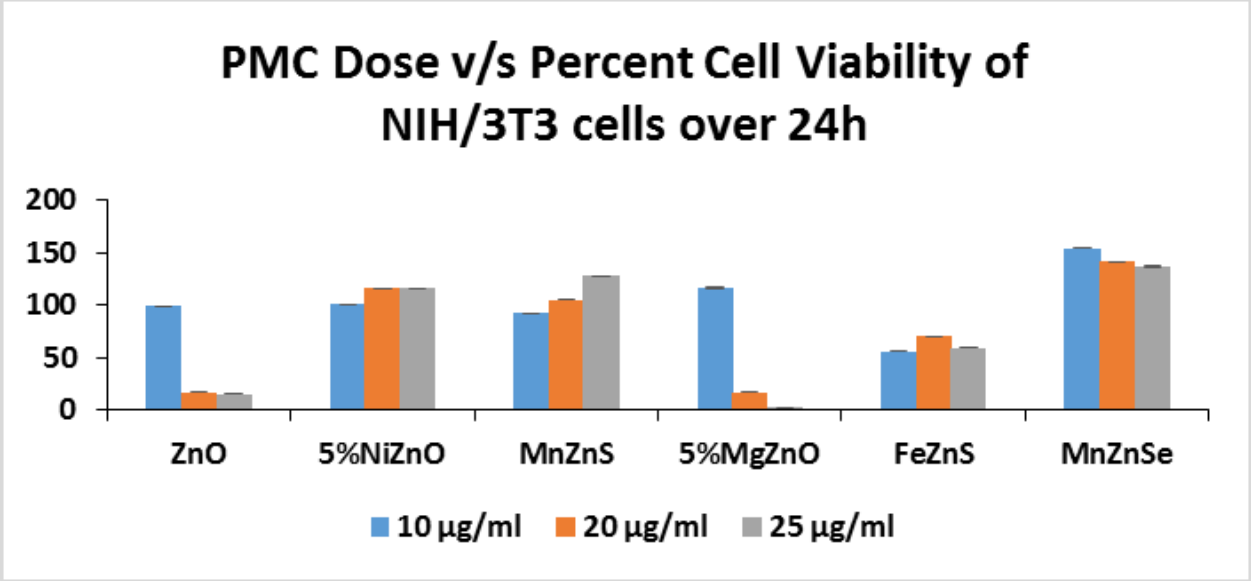

Figure A.7. Dose dependent cell viability of NIH3T3 fibroblast cells in the presence of ZnO NP and its PMCs at 24h

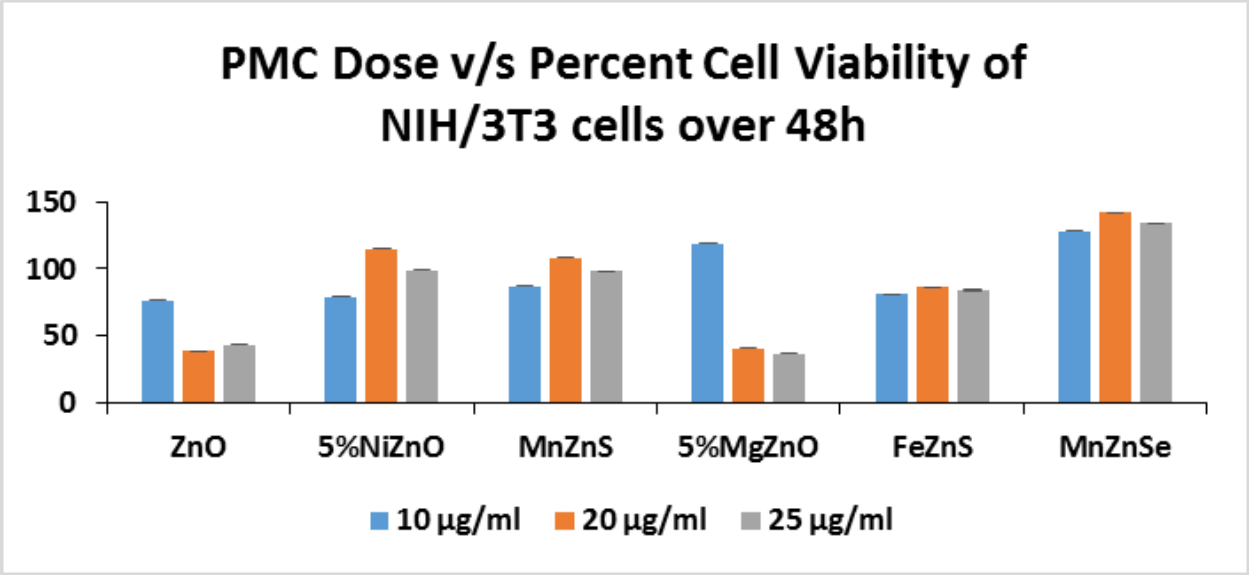

Figure A.8. Dose dependent cell viability of NIH3T3 fibroblast cells in the presence of ZnO NP and its PMCs at 48h

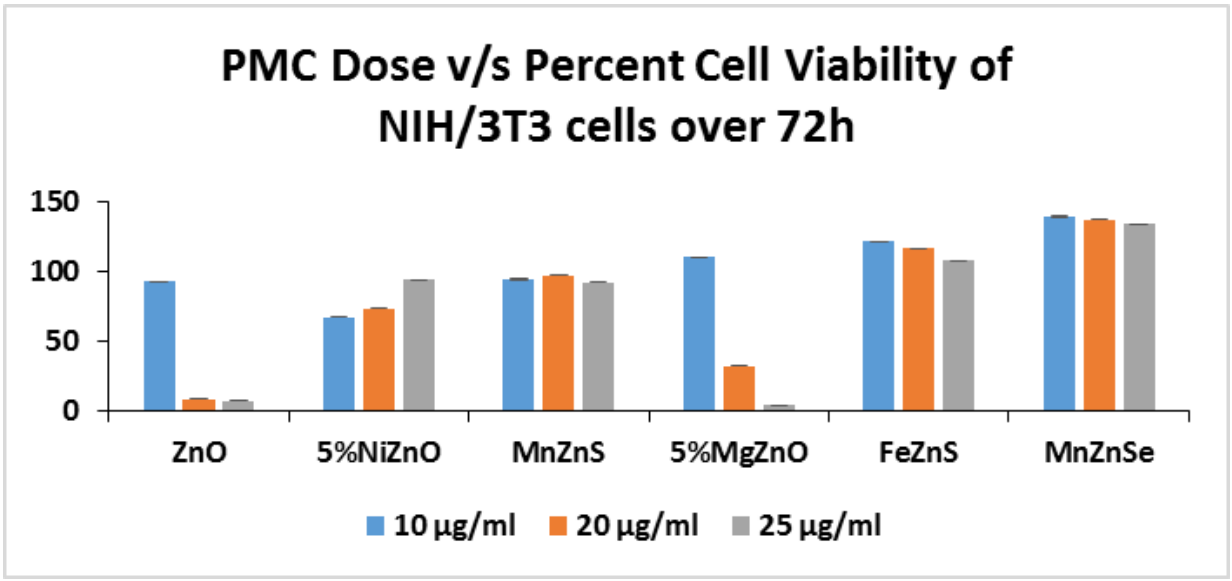

Figure A.9. Dose dependent cell viability of NIH3T3 fibroblast cells in the presence of ZnO NP and its PMCs at 72h

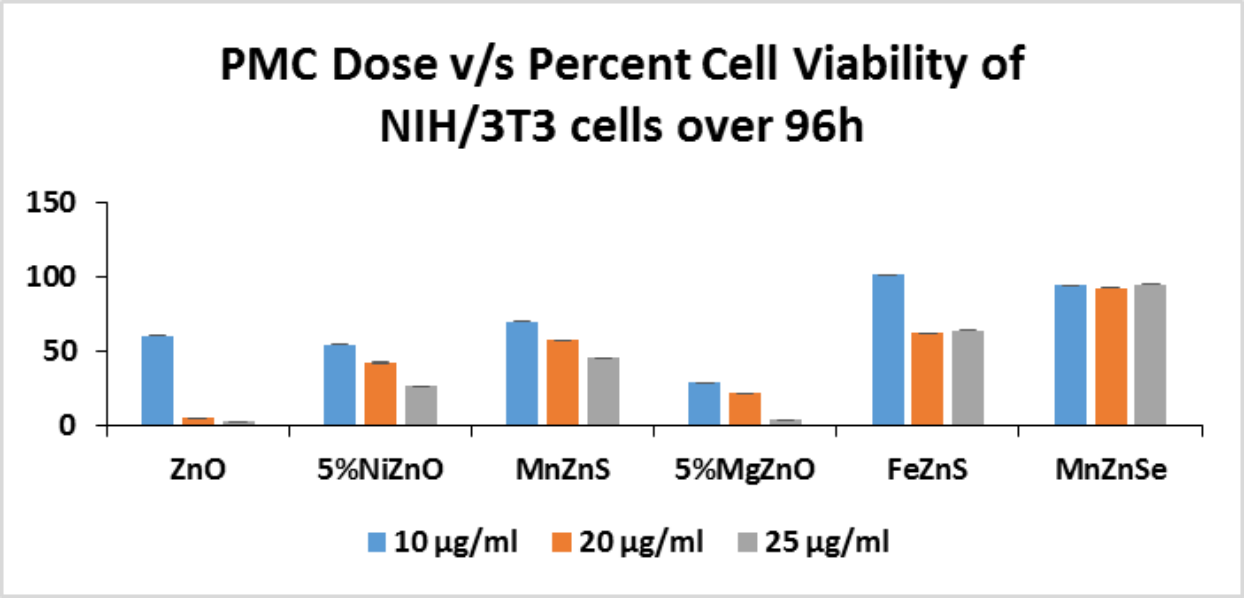

Figure A.10. Dose dependent cell viability of NIH3T3 fibroblast cells in the presence of ZnO NP and its PMCs at 96h

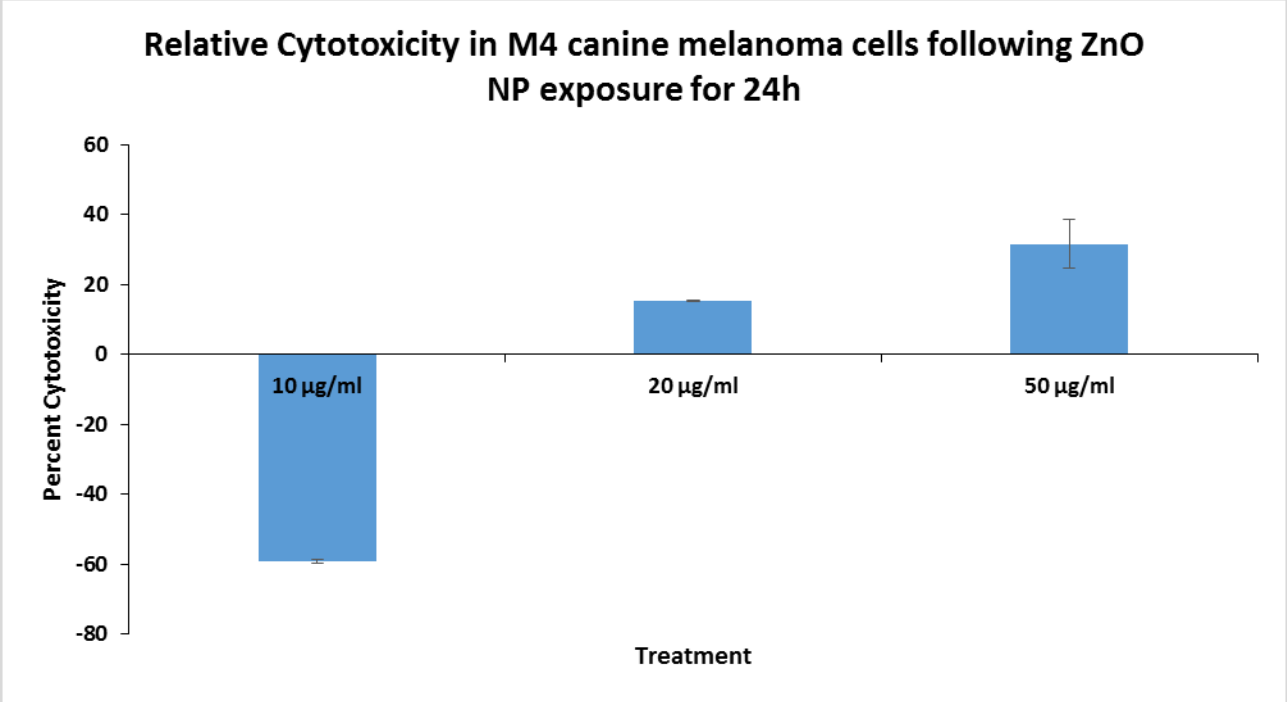

Figure A.11. Relative Cytotoxicity in M4 canine melanoma cells following ZnO NP exposure for 24h demonstrated by trypan blue exclusion assay

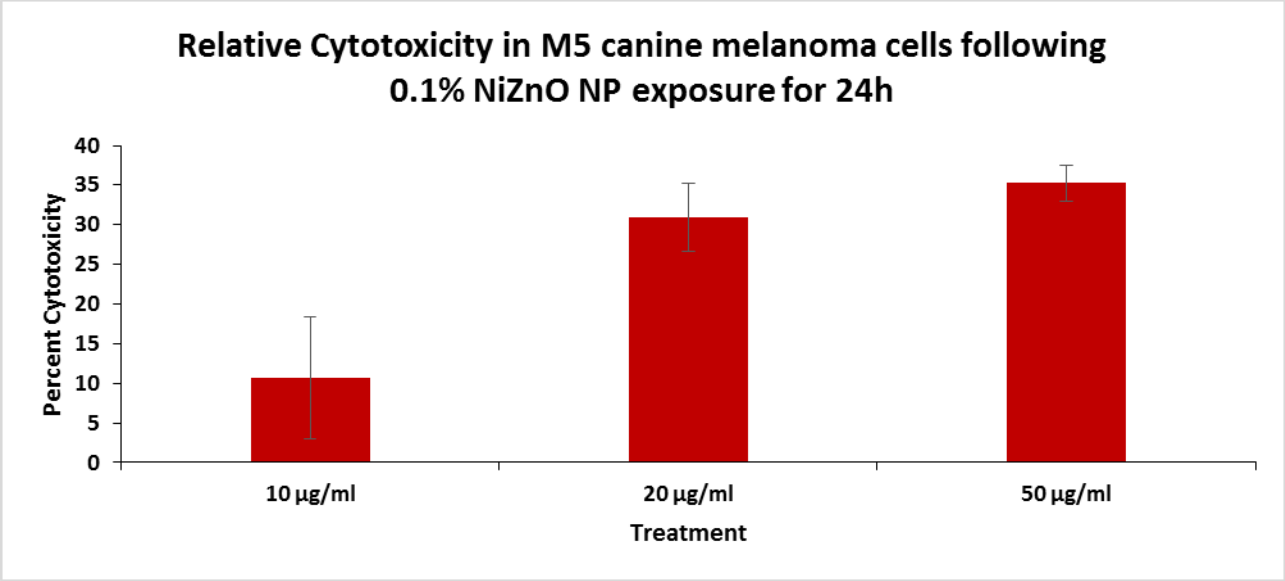

Figure A.12. Relative Cytotoxicity in M5 canine melanoma cells following 0.1% NiZnO NP exposure for 24h demonstrated by trypan blue exclusion assay

Appendix B - List of Abbreviations

Abbreviation	Expansion
ZnO	Zinc Oxide
NP	Nanoparticle
PMC	Physiometacomposite
DLS	Dynamic Light Scattering
2-D FDS	Two-dimensional fluorescence difference spectroscopy
TEM	Transmission electron microscopy
ICP-MS	Inductively coupled plasma mass spectrometry
RBD	Ras Binding Domain
EPR	Enhanced Permeability and Retention
GRAS	Generally Recognized as Safe
ROS	Reactive Oxygen Species
IL	Interleukin
BSA	Bovine Serum Albumin
CD	Circular dichroism
FTIR	Fourier Transform Infrared
HR-TEM	High Resolution Transmission Electron Microscopy
LDH	Lactate Dehydrogenase
BPF	Bovine Plasma Fibrinogen
XRD	X-ray diffraction
BCA	Bicinchoninic Acid Assay
GFP	Green Fluorescent Protein

SDS-PAGE	Sodium Dodecyl Sulphate-Polyacrylamide Gel Electrophoresis
NMR	Nuclear Magnetic Resonance
RAF	Rapidly Activated Fibrosarcoma
NGS	Next Generation Sequencing
MAPK	Mitogen Activated Protein Kinase
ERK	Extracellular Signal Regulated Kinase
AKT	Protein Kinase B
mTOR	Mammalian Target of Rapamycin
NF-κB	Nuclear Factor kappa-light-chain-enhancer of activated B cells
PTEN	Phosphatase and Tensin homolog
NAT	Nucleic Acid Therapeutic
ACP	Anticancer Protein
PEG	Polyethylene Glycol
CSNP	Core Shell Nanoparticle
pIC	Poly Inosinic acid Cytidilic acid
PK	Pharmacokinetics
PBPK	Physiologically Based Pharmacokinetics
RNA	Ribobucleic Acid
TLR	Toll-like Receptor
IFN	Interferon
TNF	Tumor Necrosis Factor
ACR	Anticancer Ribonucleic Acid
BMDC	Bone marrow derived dendritic cells

HEK	Human epidermal keratinocytes
CV	Coefficient of Variation
MgO	Magnesium Oxide
NiO	Nickel Oxide
ELISA	Enzyme Linked Immunosorbent Assay
SSO	Splice-shifting-oligomer
β-Gal	β-Galactosidase
Ex	Excitation
Em	Emission
Luc	Luciferase
TiO_2	Titanium Dioxide
B_4C	Boron Carbide
Cu	Copper
MnZnS	Manganese Zinc Sulfide
NiZnO	Nickel Zinc Oxide
ZnS	Zinc Sulfide
FeZnS	Iron Zinc Sulfide
Co_3O_4	Cobalt Oxide
CoZnO	Cobalt Zinc Oxide
ZP	Zeta potential
ASO	Antisense oligomer
HPLC	High Performance Liquid Chromatography
DMEM	Dulbecco's Minimal Essential Medium

FBS	Fetal Bovine Serum
PBS	Phosphate buffered saline
ICP-MS	Inductively Coupled Plasma Mass Spectrometry
H_2O_2	Hydrogen peroxide
RT-qPCR	Quantitative Real Time Polymerase Chain Reaction

Appendix C - List of Publications

1. Robert DeLong, Jeffrey Comer, **Elza Mathew**, Majid Jaberi-Douraki. 2019. Comparative immunological activity of physiological metal oxide and its anticancer peptide (ACP) and anticancer RNA (ACR) complexes. Nanomaterials. 9(12): 1670. https://doi.org/10.3390/nano9121670
2. R. K. DeLong, Yi-Hsien Cheng, Paige Pearson, Zhoumeng Lin, Calli Coffee, **Elza Neelima Mathew**, Amanda Hoffman, Raelene Wouda and Mary Lynn Higginbotham. 2019. Translating nanomedicine to comparative oncology: the case for combining zinc oxide nanomaterials with nucleic acid therapeutic and protein delivery for treating metastatic cancer. Journal of Pharmacology and Experimental Therapeutics. *https://doi.org/10.1124/jpet.118.256230*
3. **Elza N. Mathew**, Miranda N. Hurst, Baolin Wang, Vaibhav Murthy, Yuntao Zhang, and Robert K. DeLong. Interaction and Delivery of Ras Binding Domain (RBD) by Chemotherapeutic Zinc Oxide Nanoparticles: Progress towards RAS Pathway Protein Interference. *Manuscript resubmitted to PLOS One.*

Appendix D - Copyright Permission

November 11, 2020

Elza Neelima Mathew
Nonotechnology Innovation Center of Kansas State
Department of Anatomy and Physiology
College of Veterinary Medicine
Kansas State University
1800 Denison Avenue, 339 Coles Hall
Manhattan, KS 66506-5802

Email: elzamathew@ksu.edu

Dear Elza Neelima Mathew:

This is to grant you permission to include the following article in your dissertation entitled "Investigating the Biophysical, Biochemical, and Biological Activity of Anti-cancer Zinc Oxide Nanoparticle and its Physiometacomposite (PMC) Nanoparticles" for Kansas State University:

> RK DeLong, Y-H Cheng, P Pearson, Z Lin, C Coffee, EN Mathew, A Hoffman, RM Wouda, and ML Higginbotham (2019) Translating Nanomedicine to Comparative Oncology—the Case for Combining Zinc Oxide Nanomaterials with Nucleic Acid Therapeutic and Protein Delivery for Treating Metastatic Cancer, *J Pharmacol Exp Ther*, 370(3): 671-681; DOI: https://doi.org/10.1124/jpet.118.256230

The following must be included with your citation to the article:

> Reprinted with permission of the American Society for Pharmacology and Experimental Therapeutics. All rights reserved.

If you present the article as it was published in the journal, the original copyright line published with the paper must be shown on the copies included with your dissertation.

Sincerely yours,

Richard Dodenhoff
Journals Director